Exploring the Kuiper Belt

Design of trajectories for long-term Kuiper Belt exploration

L. van der Heyden

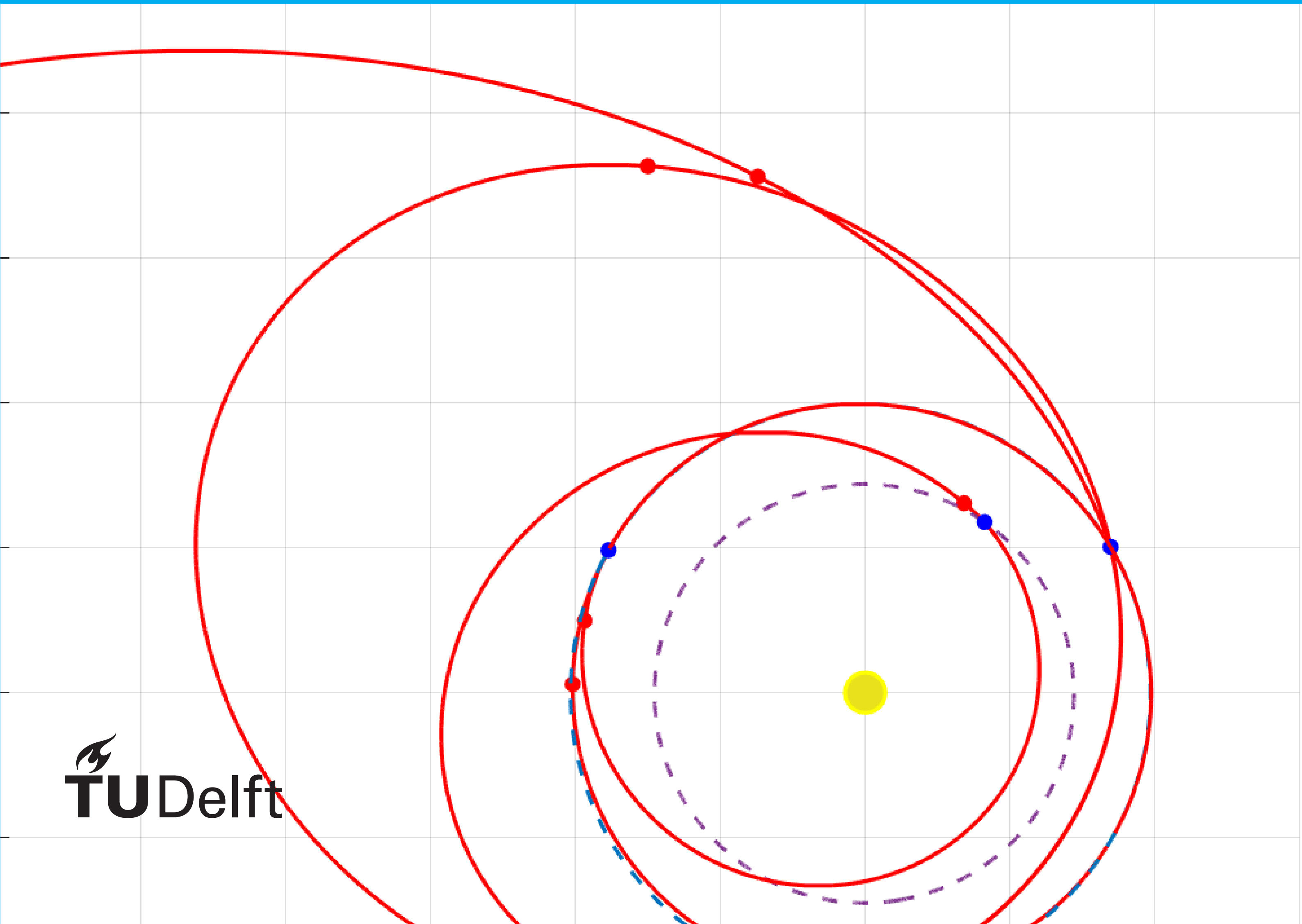

TU Delft

Exploring the Kuiper Belt

Design of
trajectories for long-term Kuiper Belt exploration

by

L. van der Heyden

to obtain the degree of Master of Science
at Delft University of Technology,
to be defended publicly on Wednesday August 26, 2020 at 14:00.

Student number:	4515366	
Project duration:	October 14, 2019 – June 30, 2020	
Thesis committee:	Dr. D. M. Stam,	TU Delft, committee chair
	Dr. ir. M. Snellen,	TU Delft, external committee member
	Ir. R. Noomen,	TU Delft, daily supervisor

Preface

Before you lies the MSc thesis ”Exploring the Kuiper Belt: Design of trajectories for long-term Kuiper Belt exploration”, a document that I consider the apex of my curriculum. I started my bachelor’s degree on Aeronautical Engineering in 2010. During these studies I first developed my interest in the scientific fields of space. After inspiring internships at Airbus and Innovative Solutions In Space, I was certain to further pursue my interest and continue my academic journey with a MSc degree in Space Flight at the Delft University of Technology.

The topic of this study was inspired by the incredible work of the NASA New Horizons mission team, who were able to succeed in performing the first space mission to Pluto and the Kuiper Belt. The intention of this study is to investigate the feasibility of trajectories for a mission with a similar underlying goal: to better understand the unique characteristics of the Kuiper Belt.

This study was performed within the Astrodynamics and Space Missions department of the TU Delft L&R Faculty. The topic of research for this study was formulated together with my supervisor, Ron Noomen, to whom I want to express my enormous gratitude for his inspiring and helpful supervision. Thank you for your guidance and support, which has enabled me to finish this thesis.

Finally, I would like to thank my family, girlfriend, and friends for their encouragement and support over these past years of my studies.

L. van der Heyden
Delft, August 2020

Table of Contents

List of Symbols

Latin

Symbol	Meaning	Unit
a	Semi-major axis	[m]
B	Impact parameter	[m]
b_{rot}	3D rotation angle	[rad]
C_3	Launch energy	[m^2/s^2]
CR	Cross-over rate	[-]
DSMDV	Delta V required to perform all trajectory DSMs	[km/s]
DV	Hyperbolic excess velocity required for launch	[km/s]
e	Orbit eccentricity	[-]
E	Eccentric anomaly	[rad]
F	Scale factor (DE)	[-]
$\overline{F}$	Hyperbolic eccentric anomaly	[rad]
$f_i(x)$	Objective function	[various]
F(x)	Set of objective functions	[-]
g_0	Standard gravity	[m/s^2]
i	Orbit inclination	[rad]
$i_{x,y,z}$	Unit vector	[-]
I_{sp}	Specific impulse	[s]
KB_{pen}	Kuiper Belt scaling penalty component	[m]
M	Mean anomaly	[rad]
$\overline{M}$	Hyperbolic mean anomaly	[rad]
m	mass	[kg]
n	Mean orbital motion	[rad/s]
n_p	Population size	[-]
P	Position	[m]
P_{sid}	Siderial period of a planet	[s]
P_{syn}	Synodic period	[s]
$\vec{r}$	Position vector	[m]
r_a	Orbit apocenter	[m]
Realb	Conservation chance	[-]
R_j	Radius Jupiter	[m]
R_m	Objective space	[-]
r_{min}	Minimum flyby distance	[m]
R_p	Orbit pericenter	[m]
r_p	Flyby distance	[m]
R_{pl}	Radius planet	[m]
t	Time	[MJD2000] or [s]
T	Neighbourhood size	[-]
T_0	Departure time	[MJD2000]
t_{dsm}	Moment of DSM application	[s]
t_i	Time of flight of an interplanetary leg	[s]
TKB	Time in Kuiper Belt	[years]
TOA	Time between launch and arrival at Kuiper Belt	[years]
V	Velocity	[m/s]

Symbol	Meaning	Unit
$\vec{v}$	Velocity vector	[m/s]
V_{esc}	Escape velocity	[m/s]
v_G	Mutant vector	[-]
V_∞	Hyperbolic excess velocity	[m/s]
x	Decision vector for trajectory	[various]
x_G	Target vector	[-]
z_i^*	Objective space reference point	[-]
z_i^{nadir}	Objective space nadir point	[-]

Greek

Symbol	Meaning	Unit
α	Asymptotic deflection angle	[rad]
ΔV	Magnitude of the velocity change of a maneuver	[m/s]
η	Fraction of interplanetary leg time of flight at which DSM occurs	[-]
μ	Gravitational parameter	[m^3/s^2]
Ω	Decision variable space	[-]
ϕ	Out-of-plane angle for the hyperbolic excess velocity	[rad]
θ	True anomaly	[rad]
θ	In-plane angle for the hyperbolic excess velocity	[rad]

Indices

Index	Meaning
dry	Excluding propellant mass
dsm	Of the DSM
f	Final
i	Initial
i	Individual in population or vector
in	Incoming (before gravity assist)
out	Outgoing (after gravity assist)
p	At pericenter
pl	Of the planet
r	Of the reach leg
sc	Of the spacecraft
wet	Including propellant mass
x	In the x-direction
y	In the y-direction
z	In the z-direction
∞	Hyperbolic excess velocity (velocity at infinity)
0	At departure
~	Of a different reference frame

List of Abbreviations

The following table gives an overview of the abbreviations used in this report. Planets are also often abbreviated when used in a planetary flyby sequence. For these abbreviations the first letter of the flyby planets are used. VVEJ for example indicates a Venus-Venus-Earth-Jupiter flyby trajectory. The departure planet is always Earth and is not listed in these abbreviations.

Abbreviation	Meaning
ACT	Advanced Concepts Team
AU	Astronomical Unit
BI	Boundary Intersection
DE	Differential Evolution
DSM	Deep Space Maneuver
ESA	European Space Agency
exp	Expended (boosters)
FH	Falcon Heavy
GA	Gravity Assist
GALOMUSIT	Genetic ALgorithm Optimization of a MUltiple Swingby Interplanetary Trajectory
GTOP	Global Trajectory Optimization Problem
HECRF	non-rotating Heliocentric ECliptic Reference Frame
HORIZONS	Horizons On-Line Ephemeris System
IR	Infrared
JHUAPL	Johns Hopkins University Applied Physics Laboratory
JPL	Jet Propulsion Laboratory
KB	Kuiper Belt
KBO	Kuiper Belt Object
LEO	Low Earth Orbit
LSP	Launch Services Program
LSST	Large Synoptic Survey Telescope
MGA	Multiple Gravity Assist
MGA-1DSM	Multiple Gravity Assist with 1 Deep Space Maneuver per leg
MHACO	Multi-objective Hypervolume-based Ant Colony Optimizer
MJD	Modified Julian Date
MOEA/D	Multi-objective Evolutionary Algorithm by Decomposition
MOI	Mercury Orbit Insertion
MSc	Master of science
NASA	National Aeronautics and Space Administration
NSGA	Non-dominated Sorting Genetic Algorithm
NSPSO	Non-dominated Sorting Particle Swarm Optimization
OPTIDUS	OPTimization of Interplanetary trajectories by Delft University Students
OSSOS	Outer Solar System Origins Survey
PaGMO	Parallel Global Multi-objective Optimizer
Pan-STARRS	Panoramic Survey Telescope & Rapid Response System
PF	Position Formulation
rec	Recovered (boosters)

Abbreviation	Meaning
RTG	Radioisotope Thermoelectric Generator
SC	Spacecraft
SOI	Sphere Of Influence
TNO	Trans-Neptunian Object
TU Delft	Delft University of Technology
ULA	United Launch Alliance
UV	Ultraviolet
VF	Velocity Formulation

Abstract

Previous trajectory proposals with the purpose of exploring the Kuiper Belt have been limited to identifying trajectories to fly by a single pre-selected Kuiper Belt Object (KBO). Furthermore, these proposals were often limited to high-velocity flybys that pass through the Kuiper Belt in a limited number of years, or are based on the assumption of significant and uncertain technological advances. This thesis investigates the existence of currently feasible trajectories which position a spacecraft inside the Kuiper Belt for a significantly longer period of time. The feasibility of these trajectories is based on the assumption of current technological capabilities and a launch date between the years 2025 and 2040.

To model these unique trajectories the conventional MGA-1DSM trajectory model is adapted in order to optimize trajectory problems that aim to reach the Kuiper Belt. The use of powered flybys is excluded in these problems in order to reduce problem and mission complexity. Optimization of the trajectory problems was done by performing an interactive multi-objective optimization approach with four distinct objectives on a set of twenty planetary sequences. The high complexity of these problems in combination with conflicting multiple objectives was found to necessitate an iterative optimization process using the pooled results of several algorithms in order to obtain satisfactory results. The optimization algorithm performance was further enhanced using various encouragement methods.

By using the established optimization method multiple routes were identified that all culminate in a long-duration flight through the Kuiper Belt. The best results were found with planetary flyby sequences VVEJS, EVEEJN, and JN. The required launch energy (C_3) for these trajectories ranges from 16 km^2/s^2, for sequences utilizing multiple inner planet flybys, to 75.5 km^2/s^2, for solutions utilizing a direct Jupiter-Neptune route. The maximum onboard delta V capability required for these solutions is 400 m/s. The flight time to the inner boundary of the Kuiper Belt ranges from 14.6 to 24 years. All these trajectories feature a flight time through the Kuiper Belt of well over or close to 100 years. In addition, it was found that trajectories that conclude their planetary flyby sequence with a Jupiter-Neptune leg are found to be especially well suited for long-duration Kuiper Belt flight.

1

Introduction

The New Horizons spacecraft has surpassed dwarf planet Pluto and is traversing the Kuiper Belt after performing the first ever flyby of a Kuiper Belt Object (KBO), also marking the most distant flyby in the history of space exploration. Discussion of the mission concept that would eventually become the New Horizons mission to Pluto began shortly after Voyager 2 flew by Neptune in 1989. Now, with New Horizons having completed its main goals, the time is right to consider new options of further exploring the Kuiper Belt. Instead of investigating opportunities to perform similar flybys of single KBOs, a more logical and challenging follow-up mission is envisioned in which the spacecraft remains in the Kuiper Belt for an extended period of time. As KBOs are relatively unaffected by the processes that have altered other Solar System objects, such a mission can provide unique data on the earliest moments of the Solar System and its formation. Determining the feasibility of the trajectories of the envisioned mission is the main topic of investigation in this thesis.

Studies on trajectories to the Kuiper Belt are often inspired by the success of the New Horizons mission and aim for high velocity flyby observations of specific objects. Preliminary trajectories to five large KBOs are presented by Mcgranaghan et al. [1]. The identified trajectories launch between 2014 and 2050 and all of them feature a flyby velocity comparable to that of New Horizons. A 2018 study by Zangari et al. [2] presents a similar analysis, finding preliminary spacecraft trajectories for 45 KBOs suitable for launch between the years 2025 and 2040. Mimicking the New Horizons mission, these trajectories also utilize an exceptionally high-velocity launch combined with a Jupiter gravity assist. Other studies, following the initial and rapid increase of KBO observations two decades ago, focus on assessing the required technology to conduct Kuiper Belt object orbiter missions. One such study by Poncy et al. [3] concludes that technology for such a mission is severely wanting for propulsion and power systems. This conclusion is supported by the results of a NASA JPL study by Oleson et al. [4], specifying a minimum of nine advanced Radioisotope Thermoelectric Generators (RTGs) to supply a KBO orbiter spacecraft of adequate power.

Instead of expanding on these works a radically different type of trajectory is investigated in this thesis. Focusing on launch opportunities between the years 2025 and 2040 with an appropriate technological requirement, it is investigated whether a spacecraft can reach the Kuiper Belt and remain there for a substantial amount of time, i.e., as long as possible. The intention is to show what trajectories are possible in the near future, how long these might take, and when they could happen. The feasibility of these trajectories is judged on four distinct criteria that focus on launch, onboard propellant, flight time, and the time spent inside the Kuiper Belt.

The research question of this thesis is:

What feasible trajectories exist that support a novel space mission, launched between the years 2025 and 2040, which places a spacecraft inside the Kuiper Belt for a prolonged amount of time?

Structure

The remainder of this report is structured as follows. Chapter 2 provides an introduction on the structure of the Kuiper Belt, in addition to information on past exploration efforts, mission proposals, and trajectory studies. More information on the alternative exploration scenario proposed by this thesis is provided. Subsequently, in Chapter 3, the characteristics of the proposed mission are further defined in order to establish the scope of the trajectory search space. Following this chapter the used trajectory design model is explained Chapter 4. This includes discussions about the assumptions made, the model architecture, the trajectory criteria, and model verification. The software, method, and further options to optimize the trajectory problems are discussed in Chapter 5. Subsequently a two-objective preliminary testing phase of the trajectory model and the optimization methods is presented in Chapter 6. Using lessons learned from these two-objective tests, the four-objective optimization method is established in Chapter 7. This optimization method is then used to produce the trajectory results which are discussed in Chapter 8. The conclusions of this thesis are given in Chapter 9. Finally recommendations for future research are given in Chapter 10.

2

The Kuiper Belt

This chapter is dedicated to provide general information on the Solar System and, more specifically, on the outermost region of it. This chapter also introduces the current and past efforts to explore the Kuiper Belt and to understand its composition and formation. First the structure and scientific opportunities of the Kuiper Belt are discussed in Section 2.1. Subsequently past efforts to visit the Kuiper Belt as well as recent mission proposals to do so are discussed in Section 2.3. Finally Section 2.4 discusses the alternatives to the typical high-velocity fly-through trajectory types that have been proposed so far.

2.1. Introduction

Figure 2.1 shows an illustration of the major bodies and regions in the Solar System. Closest to the Sun it shows the rocky inner planets Mercury, Venus, Earth, and Mars. The asteroid belt separates the inner planets from the outer planets Jupiter, Saturn, Uranus, and Neptune. Jupiter and Saturn are known as the gas giants. Uranus and Neptune are classified in a separate category as ice giants. Beyond Neptune lies the ring-shaped region known as the Kuiper Belt. This chapter serves as an introduction to the Kuiper Belt and contains information on its characteristics and unique scientific opportunities.

The Kuiper Belt extends from the orbit of Neptune, at 30 Astronomical Units (AU), to approximately 50 AU from the Sun. Beyond the Kuiper Belt are the bodies with highly eccentric orbits which can extend from 30 AU to sometimes beyond 100 AU. These bodies are part of what is called the scattered disc. The KBOs, together with objects of the more sparsely populated scattered disc, are collectively referred to as Trans-Neptunian Objects (TNOs) [5].

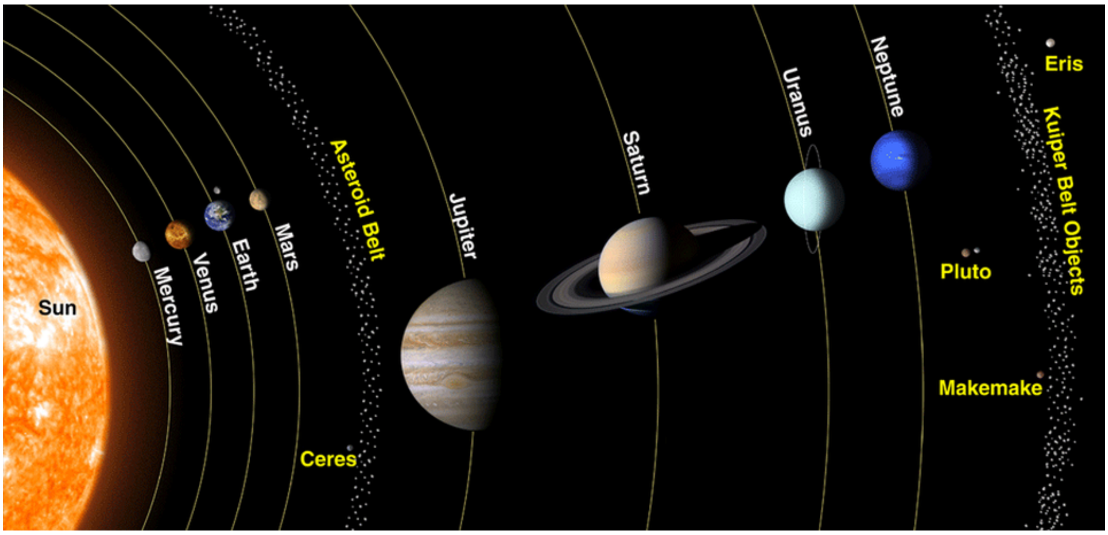

Figure 2.1: Illustration of the main bodies and regions of the Solar System, ranging from the Sun to the Kuiper Belt [6].

The discovery of the Kuiper Belt revolutionized the understanding of the Solar System and significantly influenced theories on the evolution of the protoplanetary nebula. Interest in the outer Solar System grew rapidly within the scientific community as bodies located so far from the Sun are considered fossils of the formation period of the Solar System. A better understanding of the Kuiper Belt and its objects can provide valuable information on the evolution of the Sun's planetary system but also on that of exoplanets around young stars. TNOs can be considered as the building blocks of the Solar System, containing clues to the composition of the matter from which planets were formed 4.6 billion years ago. Uncovering the properties of these objects is considered essential to understanding the formation and the evolution of the Solar System as a whole. Research into the properties and history of TNOs has become an active field of planetary science in recent decades [7].

The effort to further discover the Kuiper Belt is reflected by the increase of KBO observations in the last two decades, as shown in Figure 2.2. The number of known KBOs has increased to thousands, and more than 100,000 KBOs over 100 km in diameter are thought to exist. The discovery rate of TNOs was particularly high during the period between the years 1999 and 2017 due to the Deep Ecliptic Survey program and the Outer Solar System Origins Survey (OSSOS) program. The contribution of these projects was made possible with the availability of very large ground-based telescopes and telescopes in Low Earth Orbit (LEO) such as the Hubble and Spitzer space telescopes. While these telescopes enable observational studies of larger TNOs, obtaining information on the physical properties of a more diverse selection of the population remains a significant challenge [7][5].

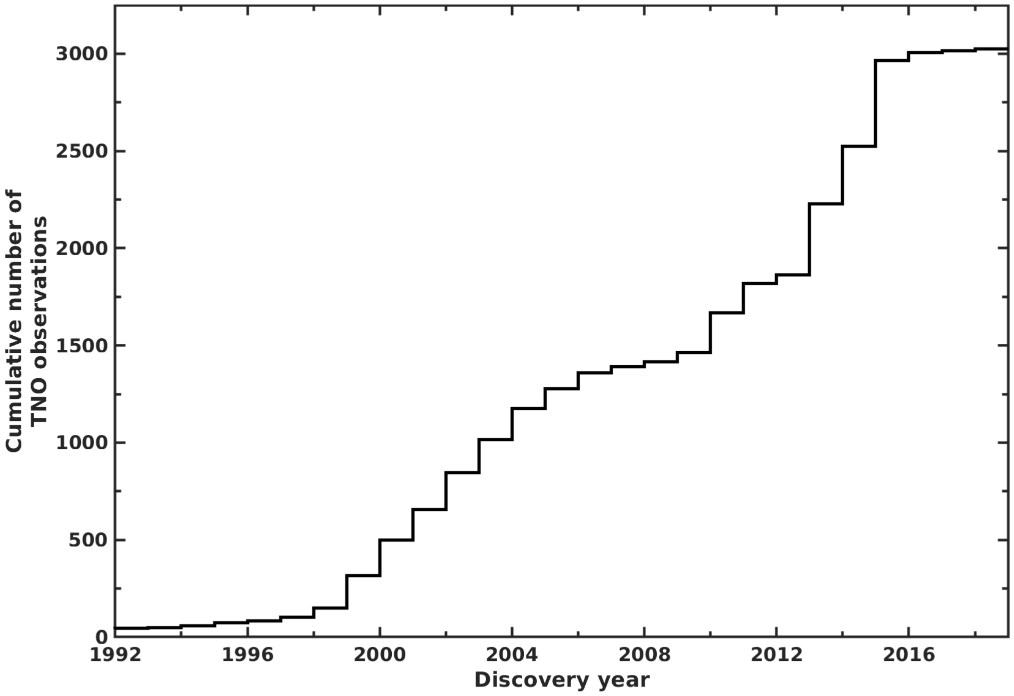

Figure 2.2: The discovery rate of TNOs with perihelion distances larger than 30 AU between the years 1992–2020. Image adapted from [5]. Updated with data taken from *JPL Solar System Dynamics* [8].

The largest objects in the Kuiper Belt that have been discovered so far are Pluto, shown in Figure 2.3, which has a diameter 2,370 km, Makemake (1,400 km), and Haumea (1,200 km). The discovery of Makemake, Haumea, and other large KBOs eventually led to the conclusion that Pluto was not particularly different from other members of the Kuiper Belt. This, combined with the fact that Pluto shares its orbit with many other KBOs, led to its reclassification of a planet to a dwarf planet. A classification Pluto shares with Makemake, Haumea, Ceres, and Eris. Pluto is still the largest KBO discovered so far, although there is evidence that suggests that at least one object larger than Pluto originated from inside the Kuiper Belt: Neptune's moon Triton [7][5].

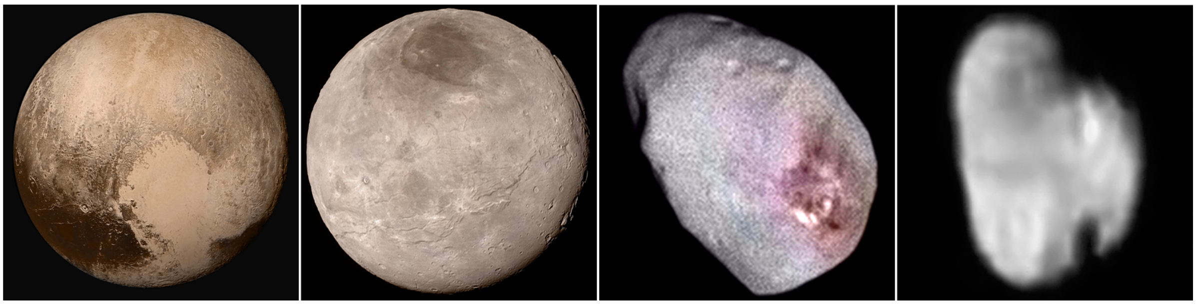

Figure 2.3: Images captured by the NASA New Horizons spacecraft showing Pluto and three of its moons named Charon, Nix and Hydra (ordered left to right) [9].

During its migration period from the inner Solar System to the outer Solar System, Neptune is thought to have captured Triton, shown in Figure 2.4. An important piece of evidence for this theory is the fact that Triton is the only large moon with a retrograde orbit close to its parent body. Unlike the large moons of the other giant planets, which are thought to have formed from the rotating discs of material surrounding the planets as they formed, Triton was likely a fully formed body that was later captured in the gravity well of Neptune [10].

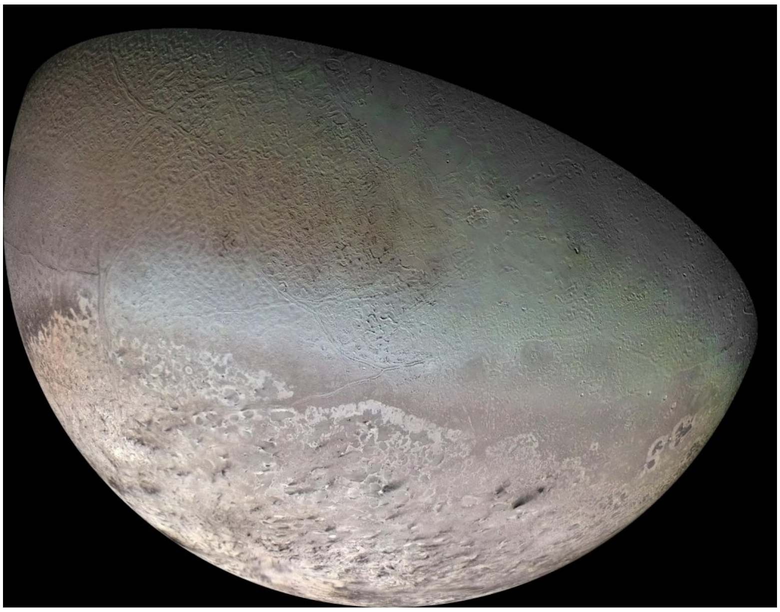

Figure 2.4: Color mosaic of Triton, taken in 1989 by Voyager 2 during its flyby of the Neptune system [11]. Triton is thought to have originated from the Kuiper Belt before being captured by the gravitational pull of planet Neptune.

2.2. Structure and Distribution

The presence of Neptune has a significant effect on the structure of the Kuiper Belt due to orbital resonances. Over time Neptune's prominent gravitational pull destabilizes the orbits of any small object that interacts with it, slinging the object into the inner Solar System or out into the scattered disc or even into interstellar space. This phenomenon causes the Kuiper Belt to have significant gaps in its layout, similar to the asteroid belt's Kirkwood gaps. Such a gap can for example be found in the region bounded by 40 and 42 AU. Any object observed in this sector must have migrated there relatively recently as no stable orbit is possible there [7][12].

The phenomenon of these resonances also causes the opposite effect, leading to certain regions being more densely populated than others. The most densely populated region of the Kuiper Belt is considered to extend from the 2:3 resonance at 42 AU to the 1:2 resonance at 48 AU. This region is known as the classical Kuiper Belt and it contains roughly two thirds of the KBOs observed to date. The classical Kuiper Belt is further divided into two classes: the dynamically cold and the dynamically hot population. The cold population consists of bodies with close to circular orbits and with an inclination to the ecliptic plane of up to 10 degrees. The cold population also contains a core at around 44 AU at which a higher density of classical objects have been observed. The dynamically hot population generally has orbits which are much more inclined, with some objects featuring inclinations of up to 30 degrees. The orbital parameters of these two groups are not the only features dividing them, the physical characteristics of the objects themselves also differ. The cold population generally has a higher albedo and contains a larger fraction of binary objects. A proposed theory for these differences in characteristics is that the hot population was formed near Neptune's original orbit and was later scattered out during the migration of the gas giants in the early period of the Solar System. The cold population is thought to have formed in more or less its current position as any encounters with Neptune would have torn the large number of binary objects apart [7][12].

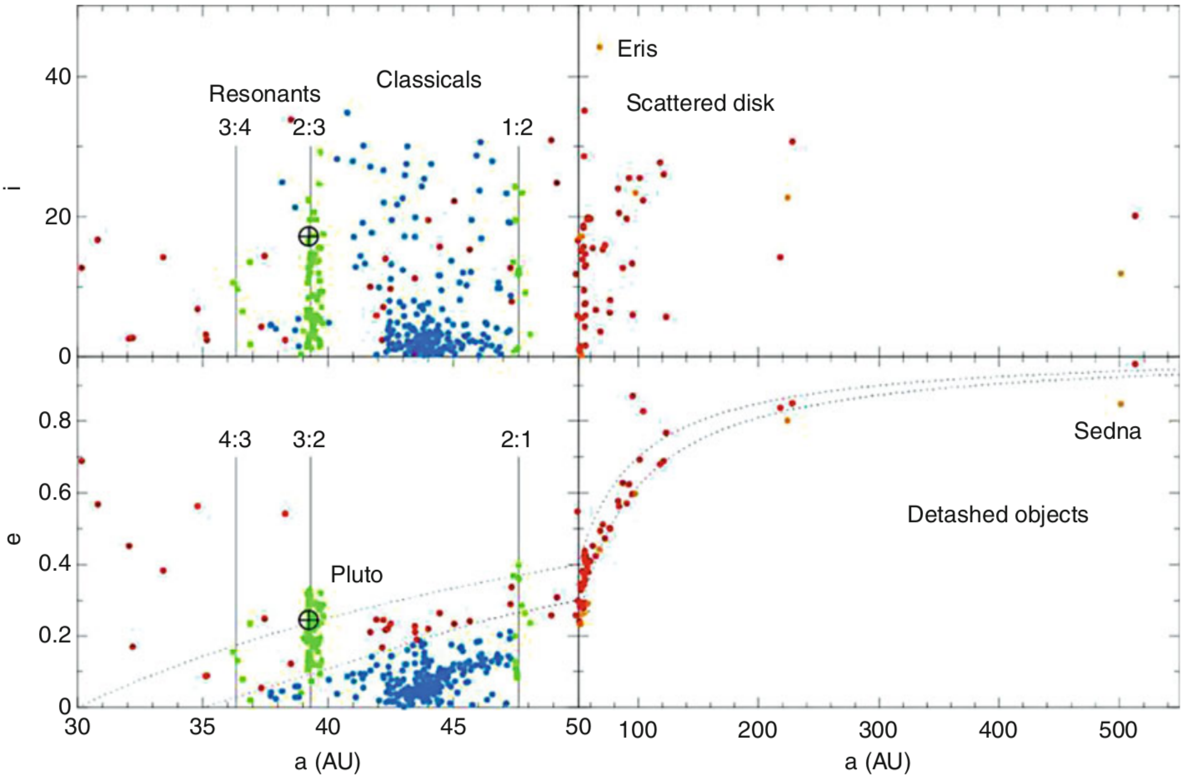

Figure 2.5: This diagram illustrates the distribution of Trans-Neptunian objects (resonant, classical, scattered disk, and detached objects) at different semi-major axes (a), eccentricities (e), and inclinations (i) [7].

The precise origin of the Kuiper Belt and the nature of its complex structure are still unclear. Astronomers are awaiting the completion of several wide-field survey telescopes such as the Panoramic Survey Telescope & Rapid Response System (Pan-STARRS) and the future Large Synoptic Survey Telescope (LSST), which should reveal many currently unknown KBOs. So far observations have shown that there is a relative absence of objects with a semi-major axis smaller than 39 AU. This absence of objects can not be explained by the effect of resonance with Neptune. The current theory proposes that the objects in this region were ejected by the gravitational pull of Neptune as the planet migrated outwards in an early period of the Solar System. Another phenomenon in the structure of the Kuiper Belt that can not be fully explained is the relative absence of objects beyond the 1:2 resonance at approximately 48 AU. This boundary at which there is a sudden decrease in the abundance of objects is known as the Kuiper cliff. Models of the formation of the Solar System and the Kuiper Belt suggest that this region should actually host an increased number of large bodies. It is currently not known whether the Kuiper cliff is just a broad gap or if it should be seen as the end of the classical Kuiper Belt. One interesting but controversial theory to explain the clustering of objects in these regions is that it is caused by the gravitational attraction of a large unobserved planetary body, sometimes called Planet Nine, whose mass would have to be more than five times that of Earth [7][12].

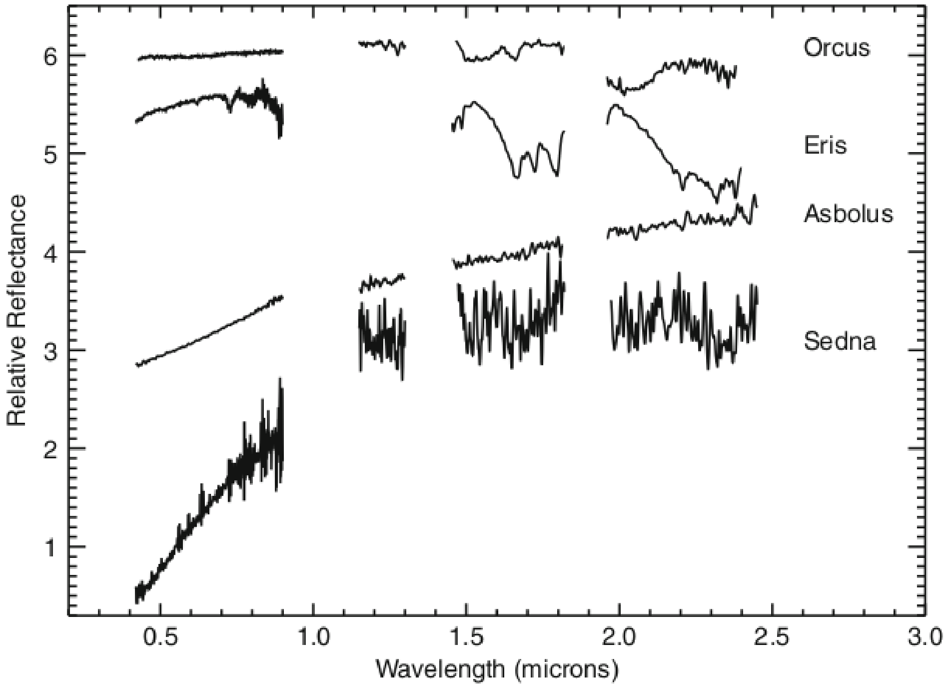

Figure 2.6: An example of the visible and near-infrared spectra of three TNOs (Sedna, Eris, and Orcus) and the Centaur Asbolus. The four objects each show different absorption behavior at the various wavelengths [7].

Due to their small size and extreme distance from Earth, the structure and physical makeup of KBOs is very difficult to determine. The principal method by which astronomers determine the composition of these celestial objects is spectroscopy. An example of this technique for several TNOs can be seen in Figure 2.6. Although to date most KBOs still appear spectrally featureless due to their faintness, there have been a small number of successes in determining their composition. For some smaller objects information on the visible and near-infrared color spectrum and relative reflectance has been retrieved. An example of this is shown in the data of Figure 2.6. However, most of the known TNOs are too faint for spectroscopic observations with the current largest telescopes. Future surveys, such as those by the previously mentioned Pan-STARRS and LSST projects, will enable the discovery of many more objects including their physical characteristics. Meanwhile, the in-situ measurements of the NASA New Horizons mission have revealed many additional properties of the Pluto system and of a KBO named Arrokoth that would have been impossible to obtain with ground-based telescopes [7][12].

2.3. Exploration History

Physical exploration of the Kuiper Belt was initiated with the NASA New Horizons mission. The complete trajectory of the New Horizons spacecraft between launch in January 2006 and August 2020 is shown in Figure 2.7. The New Horizons primary objective was a flyby of Pluto and its largest moon Charon. After completing this flyby in July 2015, the New Horizons mission was extended in order to perform its secondary objective: locate and investigate more distant KBOs [13][14].

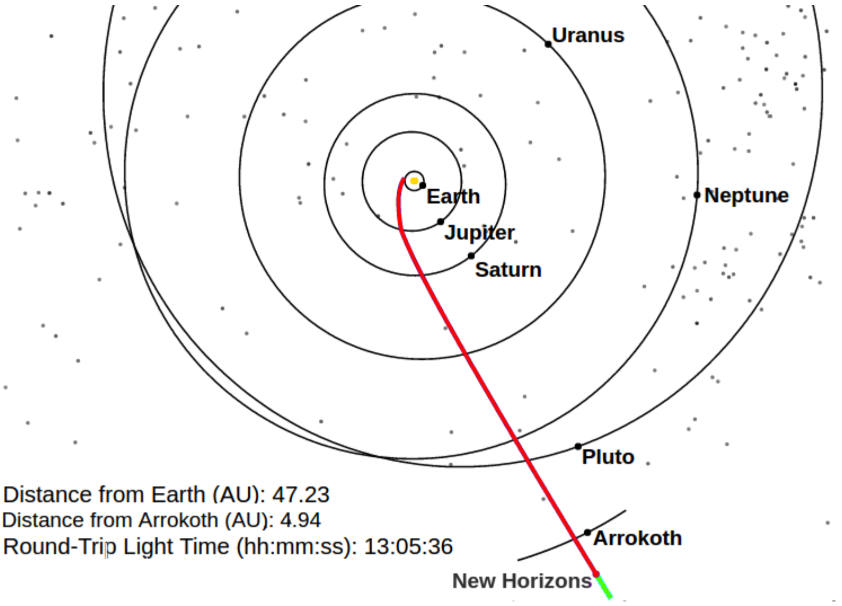

Figure 2.7: Trajectory, position and heading of the New Horizons spacecraft, last updated August 2020 [15].

As the remaining propellant aboard the probe was extremely limited at this point in the mission, the range of candidates for this extended mission were narrow. With use of the Hubble Space Telescope three candidates were selected, all three of them members of the cold classical Kuiper Belt population. The most favorably situated of these objects was candidate *2014 MU69*, nicknamed *Ultima Thule*, and ultimately officially named *486958 Arrokoth*. Course corrections of the New Horizons probe took place in early November of 2015, resulting in the first-ever flyby of a KBO on the first of January 2019. Relayed data of this flyby resulted in the image shown in Figure 2.8. Additional scientific data is expected to continue to be received over the course of the year 2020. The onboard RTG continues to generate sufficient power to keep the spacecraft operational until the mid to late 2030s. The potential for an additional KBO flyby at the outer edges of the Kuiper Belt depends on funding and on finding a suitable KBO close enough to the spacecraft's current trajectory [13][14].

Figure 2.8: Composite image of Kuiper Belt object 2014 MU69, now officially named Arrokoth. Compiled from enhanced color data combined with high-resolution pictures obtained by the New Horizons spacecraft [16].

The New Horizons spacecraft was able to reach Pluto in just nine years due to its extremely high heliocentric velocity. The launch vehicle included an added third stage which increased the launch energy (C_3) to 157.75 km^2/s^2, the highest of all space launches at that time, and about ten times that of a typical mission to planet Mars. After separation from the launch vehicle, New Horizons reached a velocity of about 16.26 km/s. The heliocentric velocity was further increased by a Jupiter flyby in 2007. The backup launch windows in February 2006 and February 2007 would not have been able to use this gravity assist and would thus have an increased flight time to Pluto of five to six years. The heliocentric velocity of New Horizons and Voyager 2 in relation to the Solar System escape velocity is shown in Figure 2.9. The velocity profile of New Horizons shows a clear contrast with that of Voyager 2. New Horizons achieved Solar System escape velocity with the use of its launch vehicle and then used Jupiter as an additional boost in order to encounter Pluto earlier. The velocity of Voyager 2 after launch was much lower but the spacecraft used each subsequent planetary encounter to build up more heliocentric velocity, ultimately exceeding the velocity of New Horizons after encountering Saturn. It is interesting to note here that the heliocentric velocity of the Voyager 2 spacecraft was reduced during its flyby of planet Neptune [17][18].

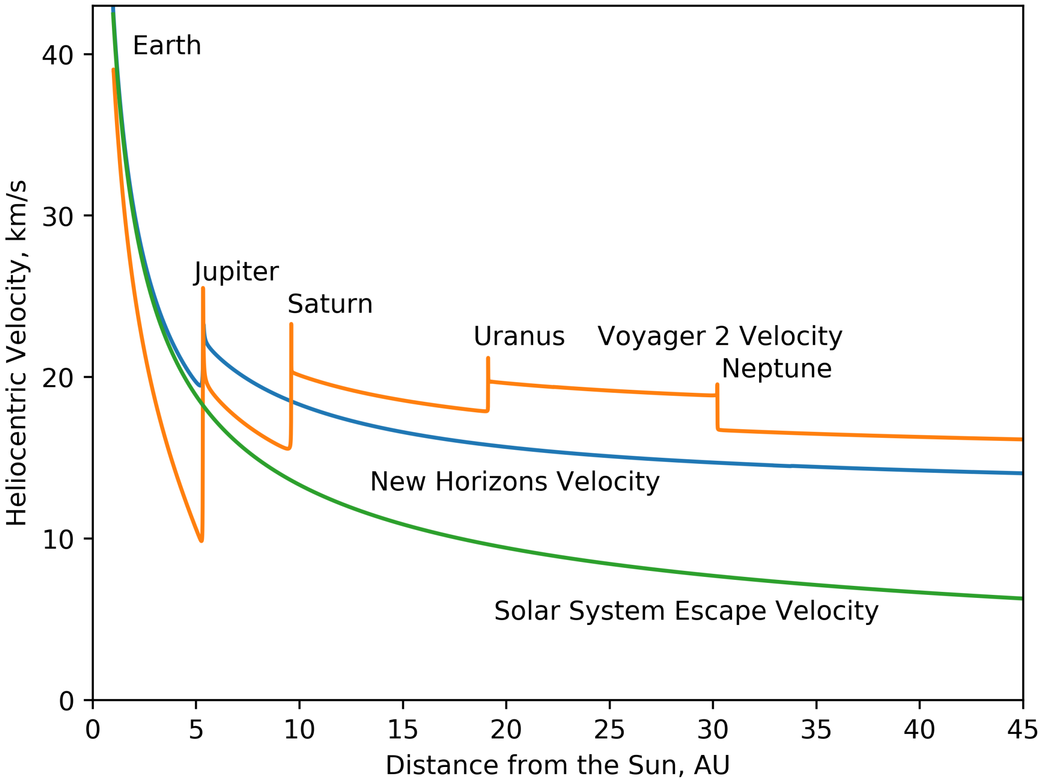

Figure 2.9: Plot of New Horizons and Voyager 2 heliocentric velocity against their distance from the Sun. The two velocity profiles show the difference in how Solar System escape velocity was reached by each probe. (Data source: HORIZONS System, JPL, NASA [8])

As stated previously, the potential for New Horizons to perform a flyby of an additional KBO is largely dependent on finding a suitable target. The spacecraft is coasting through the Kuiper Belt at high velocity and its capability to perform trajectory adjustments is limited by its small remnant of propellant available. Additionally, New Horizons was designed in line with its main mission objective: a comprehensive flyby study of the Pluto system. Its investigation of additional KBOs was and still is a secondary goal. To expand on the Kuiper Belt exploration efforts made by the New Horizons mission multiple new missions have been studied and proposed in the last two decades. These concepts include a direct successor initiated by New Horizons principal investigator Alan Stern and others in their proposal for a New Horizons 2 mission in 2002. This mission was primarily aimed to continue the Kuiper Belt exploration efforts of the original mission and to make use of an opportunity to perform a flyby of planet Uranus. The New Horizons 2 proposal was ultimately denied due to a shortage of plutonium-238 radioactive material required for the construction of onboard RTGs [19][20].

Further interesting proposals which stated an objective to further explore the Kuiper Belt were 2009 and 2019 NASA mission proposals *Argo* and *Trident*. The Argo mission would take advantage of a favorable outer planet alignment by launching between the years 2015 and 2020. This would enable gravity assists from Jupiter, Saturn and a flyby of the Neptune system. The final phase of the mission would then consist of one or more KBO flybys. Multiple trajectories and launch opportunities were analyzed and listed by Hansen et al. [21][22].

One of these proposed trajectories for the Argo mission is shown in Figure 2.10. The trajectory clearly shows the favorable alignment of planets Jupiter, Saturn and Neptune that is utilized by launching in late 2019. It also shows how the gravitational pull of Neptune is used to set up the flyby of a KBO. This gravity assist would enable any course within a 120 degree cone without using onboard propulsive means. In comparison, a suitable KBO destination for New Horizons had to be selected from within a 0.9 degree cone of the established trajectory [21][22].

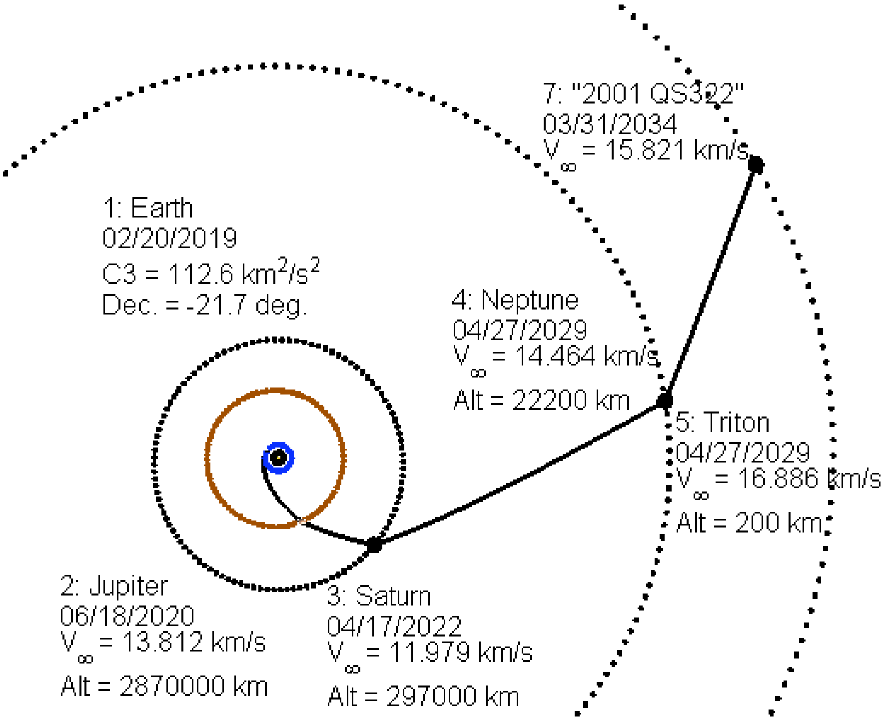

Figure 2.10: A proposed Argo trajectory which includes flybys of Jupiter, Saturn, Neptune, Triton, and a KBO [22].

An exciting mission currently being studied is the mentioned NASA Trident mission. First officially proposed in 2019, it was selected along three other Discovery Class proposals for further study in 2020. The main scientific goal of the Trident mission is to investigate Neptunian moon Triton. The proposed spacecraft and trajectory have some similarities with the New Horizons mission, in particular designing the mission for a very fast flyby of the target and using remote sensing equipment with large apertures and high angular resolution sensors. The trajectory of Trident is aimed to bring the spacecraft through the ionosphere of Triton, within 500 km of the surface. This feat requires exquisite orbital positioning of the spacecraft at a distance of 50 AU from the Sun, as the margin for error is quite small in such an exceptionally low altitude flyby. For reference, the New Horizons flyby of Pluto had a closest approach distance of 12,500 kilometers. If Trident is selected for further development and ultimately launch, the envisioned spacecraft will weigh about 1,000 kg, roughly twice the mass of the New Horizons spacecraft [23].

The trajectory of the proposed Trident mission is shown in Figure 2.11. Launching in the first half of 2027 and using a launch energy of 25.75 km^2/s^2 the spacecraft would be put on a course which sets up a multitude of gravity assists in the inner Solar System. Using a flyby sequence of Earth, Venus, Earth, Earth, the heliocentric velocity is increased in steps until a flyby of Jupiter is performed approximately six years after launch. This Jupiter flyby is performed at an altitude of around 87,000 km, or 1.24 Jupiter radii, which provides an opportunity for a close flyby of Jupiter's moon Io. After the Jupiter gravity assist the Trident spacecraft will be on route for its flyby of Neptune and Triton another six years later in the year 2038. The EVEEJN ballistic trajectory enables a minimal propulsion system while still limiting the time of flight to Triton to twelve years [24].

As mentioned, the primary research objective of Trident is the Neptunian moon Triton. The additional science objectives during its flight will include Jupiter, Io, and Neptune itself. After the high velocity flyby of Trident a mission extension to visit objects in the Kuiper Belt is possible but certainly optional. This is a commonality with the New Horizons mission where a visit of a KBO after the Pluto system flyby was a secondary objective which was only possible after a successful mission extension request. The high-velocity flyby of Triton will result in a similar scenario in which a KBO will have to be selected out of a limited range of candidates which happen to be in reach of the established trajectory by chance. Furthermore the instrument suite of Trident will be designed for its science objectives at Triton, particularly concerning the possible detection of its suspected subsurface ocean [25].

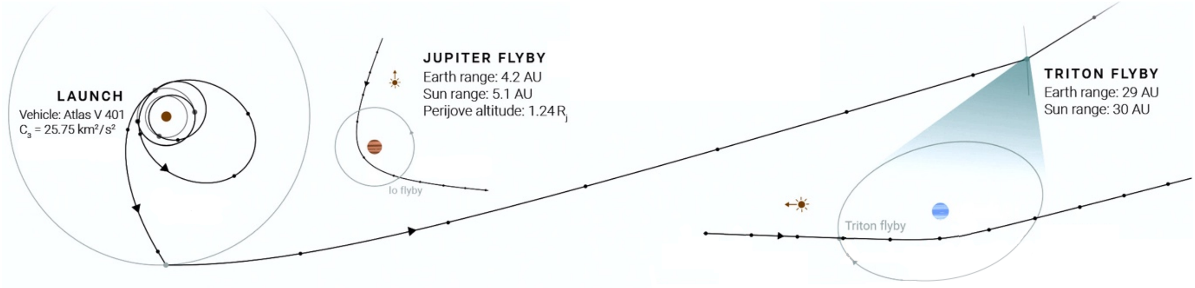

Figure 2.11: The proposed Trident mission trajectory utilizes an EVEEJN flyby route and culminates in a fast flyby of Triton in 2038 and an option of subsequent KBO flybys [23].

Studies on identifying optimal trajectories dedicated purely for Kuiper Belt exploration are often building on the success of the New Horizons mission and focus on high-velocity flyby observations of KBOs. In general these trajectories are optimized for a specific pre-selected KBO, typically targeting the one of the larger variants. Earlier such studies, following the initial but rapid increase of TNO observations two decades ago, focus on preliminary assessments regarding the required technology to enable exploration of these at the time newly discovered planetary bodies.

A study performed by Poncy et al. in 2009 aims to quantify the technological advances needed to perform a TNO-orbiter mission, specifically targeting dwarf planet Haumea. They conclude that current technology for such a mission is severely lacking in the fields of propulsion system performance and power generation systems. Arguing that a high-efficiency electric low-thrust propulsion system would be required, capable of generating a specific impulse of 15,000 seconds. To power such a system significant advances would have to be made in the development and production of powerful onboard nuclear reactors [3]. This conclusion is supported by the results of a NASA JPL study by Oleson et al. in 2011. This study was performed to explore the use of radioisotope electric propulsion for a similar KBO orbiter mission to be launched in the 2030 time-frame. The study concludes that for such a mission four kilo-Watt of power would be needed to power both the ion propulsion system and the spacecraft. With such technology the spacecraft would be able to rendezvous with and subsequently orbit a KBO after sixteen years of flight time. To provide such amounts of power the spacecraft would need a minimum of nine advanced RTG power systems [4]. However, the production rate for the plutonium required for these RTGs has been a bottleneck for years, a statement supported by the conclusion of the New Horizons II report by the New Horizons II Review Panel in [20].

A more thorough discussion on the consideration of high-thrust and low-thrust propulsion systems for missions to the outer Solar System can be found in Chapter 5 of the literature study that preceded this thesis, see [26]. The mentioned studies and further exploration of this topic in the literature study resulted in the decision to focus on more conventional high-thrust propulsion trajectories in this thesis project. A low-thrust scenario is noted as an interesting and promising follow-up topic of investigation. A good starting point for such research would be the work of Baskaran et al. in [27] where low-thrust trajectories for high-velocity flyby missions to selected KBOs were identified.

Preliminary design of high-thrust flyby trajectories to five large TNOs Sedna, Makemake, Haumea, Eris, and primarily Quaoar are discussed by Mcgranaghan et al. in a 2011 study. Limiting Earth departure dates between 2014 and 2050 and a maximum time of flight of 25 years, the best trajectories are found when using only a Jupiter gravity assist, with total mission delta V as low as 7.15 km/s. The transit time ranges from 13.5 to 24.5 years depending on the target object. The arrival velocities for these trajectories are comparable to that of New Horizons. The study emphasizes that the geometry of the Jupiter gravity assist has a crucial effect on the orbit solution, in particular the periapse radius distance which varies from 3.5 to 25 Jupiter radii for the identified solutions [1].

The 2018 study by Zangari et al. performs a similar analysis, finding preliminary spacecraft trajectories for 45 KBOs and Pluto suitable for launch between the years 2025 and 2040. The trajectories are modeled after the New Horizons mission style: a high C_3 launch with a Jupiter gravity assist. Additionally Earth-Jupiter and Earth-Saturn scenarios with optional Uranus or Neptune assists are evaluated. For high-velocity flybys of most target KBOs the study concludes that a single Jupiter gravity assist is the most efficient method to reach the Kuiper Belt [2].

A follow-up study to that of Mcgranaghan et al. was performed by Gleaves et al. in 2012. Instead of aiming for high-velocity flyby trajectories, this study aims to find solutions to insert a spacecraft in orbit of one of the larger TNOs. The trajectory search space is based on the results of Mcgranaghan et al. and is therefor limited to only evaluating high C_3 launch to Jupiter gravity assist trajectories. The study notes that the meager gravitational pull of KBOs means that the high arrival velocity will have to be almost completely negated by the vehicle itself in order to accomplish a closed orbit around the target body. One of the proposed solutions for this challenge is to equip the spacecraft with a multi-stage propulsion system based on the STAR48 engines also used as a final stage for current heavy-lift launch vehicles [28].

2.4. Alternative Exploration Scenarios

Instead of expanding the work done mentioned in Section 2.3 by exploring similar options, this project aims to find trajectories that enable long-term observation of objects from inside the Kuiper Belt. To enable this, three main methods were proposed, of which one was selected as a most interesting and most promising scenario to investigate. The evaluation of these three methods is discussed in this section.

The New Horizons mission was indisputably highly successful and provided otherwise unobtainable data on Pluto, as well as the first-ever detailed images of a KBO. Nevertheless, the high-velocity flyby limits the observation time of KBOs to very short time-frames and restricts the number of objects observed to one, possibly two, over the course of the entire mission. An obvious solution to ensure a longer period of valuable data collection would be to insert a spacecraft into orbit of, for example, a KBO with particularly interesting qualities. However, as discussed in Section 2.3 the feasibility of a KBO orbiter mission in the near future seems unlikely at best. Feasibility studies depend on either significant advances in onboard nuclear power systems and electric low-thrust propulsion systems, or on integrating an unprecedented amount of conventional delta V capability to perform the orbit insertion burn around the target object. This project aims to avoid these problems and to be a first step into identifying and evaluating trajectories that can be flown with current or very-near future technology while also allowing longer observation of multiple KBOs.

The goal of this project requires a trajectory which enables a significant amount of time to be spent within the target region, while also allowing a diverse selection of KBOs to be observed. In order to make this possible it is likely that a non-hyperbolic trajectory is required. A rapid high-velocity passage through the Kuiper Belt mimicking the Voyager and New Horizons probes is not sufficient for this purpose. Instead a near-circular orbit between 30 to 50 AU, or a highly eccentric orbit that ranges from the outer edge of the Kuiper Belt at aphelion to a distance of only several AU (or even less) from the Sun at perihelion would likely be much more attractive. A third option is to design a mission which creates a multiple-spacecraft constellation in which each probe passes through the Kuiper Belt at a different epoch, thereby increasing the time and the diversity of objects observed within the region. For clarity, these three scenarios are illustrated in Figure 2.12 and each will be discussed shortly in the remainder of this section.

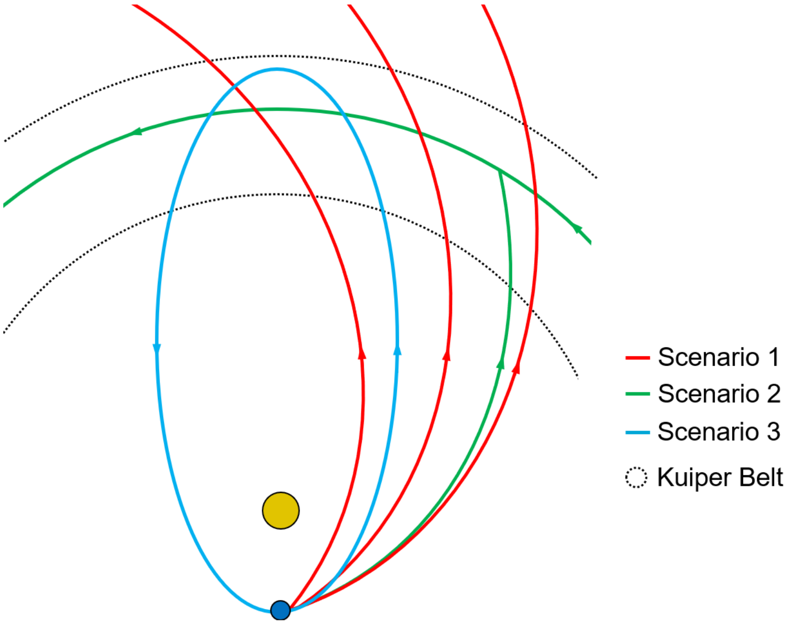

Figure 2.12: To facilitate long term and diverse Kuiper Belt object observations three types of missions were considered. 1: Multiple Spacecraft Constellation. 2: A circular orbit inside the KB. 3: An eccentric orbit with aphelion inside the KB.

Constellation scenario

The first option would be to launch multiple probes which all fly through the Kuiper Belt, at different epochs or in different regions, in order to create a semi-permanent stream of continuous data. For example, if a single satellite can provide interesting scientific data for five years, every subsequent satellite could enter the region approximately five years after the former. The first drawback of this is of course that developing, building, and launching multiple separate probes increases the cost of the mission. The availability of planetary swing-by opportunities is dependent on time and it would take careful planning to get each probe in the right trajectory at the right time. To reduce cost and complexity, multiple probes of the same design can be launched with a single launch vehicle. Each probe then using a slightly different trajectory to enter the Kuiper Belt at the appropriate time or in the right region. It should also be noted that the use of multiple probes increases the chance of one of these spacecraft failing, but also increases the chance of at least one spacecraft reaching the Kuiper Belt and functioning nominally. A major drawback of this idea is that the construction of multiple probes will demand the production of at least an equal number of RTGs. As mentioned in Section 2.3, RTG production rate is an ongoing challenge and the New Horizons II proposal was denied because of it. The RTG aboard the flown New Horizons probe itself was even reduced in size due to the scarcity of the available isotopes [29]. The decision to pursue building and launching multiple spacecraft each with an onboard RTG all for the same mission is difficult to defend with the scarcity and value of these resources in mind.

Circular orbit scenario

With a circular orbit the probe would be permanently orbiting the Sun at a distance of 30 to 50 AU. Certainly a spacecraft in such an orbit would allow sufficient time to encounter and observe a plethora of KBOs. However, the combination of the large distance from the Sun and of circularizing the orbit once arriving at the 30 AU boundary would take a significant amount of delta V. Preferably the final orbit of the spacecraft is reached without employing a large propellant burn in a late stage of the trajectory. If such a maneuver were to be feasible and it would likely be more desirable to use it to facilitate a KBO orbiter mission such as those proposed by Gleaves et al. [28]. This project aims to find a trajectory solution for a mission that does not require advancements in technology which are uncertain to exist in the near future. To get an indication of current conventional onboard spacecraft delta V budget capabilities: New Horizons had a total maneuver budget of about 0.3 km/s [30]. The Cassini mission to Saturn, one of the largest spacecraft launched in history, had a total delta V capability of 2.36 km/s and used about 1.0 km/s of this budget to prepare its second Venus gravity assist maneuver and its orbital injection maneuver of Saturn [31][32]. Based on these values deploying a satellite capable of employing more than a few km/s of delta V by using propulsion methods after or shortly before reaching 30 AU is deemed unrealistic. Circularization of the orbit can partially be done by performing gravity assists around the outer bodies Neptune or even Pluto, but it is deemed unlikely at this point that these maneuvers can be significant enough to eliminate the necessity of large propellant burns.

Eccentric orbit scenario

The idea of an eccentric orbit scenario would be to place a probe in a highly eccentric orbit with an aphelion at the outer edge of the Kuiper Belt. Data is gathered while the probe is flying through the target region and this can be sent to Earth at increasingly high bit-rates as the spacecraft is returning closer to Earth after the orbit apocenter. Using Kepler's third law to evaluate this approach an orbital period of approximately 130 years is calculated. This obviously exceeds the realistic time-frame for this (or any) near future space mission. In such an orbit however, due to the extreme distances and an eccentricity which is close to one, the probe would spend almost 90 years between 30 and 50 AU from the Sun. The energy required to adjust a hyperbolic to an highly eccentric orbit is naturally also much smaller than to change it to an orbit with an eccentricity that approaches zero. However, it is undesirable to fly a trajectory in which a crucial course adjustment has to take place at a very late stage of the mission. To perform such a late maneuver would necessitate hauling the required amount of propellant along to this point, as well as risking the success of the mission on this maneuver. The eccentric orbit scenario would thus preferably make use of a trajectory that obtains the final orbit shape before the Kuiper Belt itself is reached.

To further evaluate the possibility of reaching the Kuiper Belt in a closed but highly eccentric orbit the three plots in Figure 2.13 are used. The top plot displays the transfer time of a spacecraft with perihelion (R_p) at approximate Earth orbit radius and a varying orbit aphelion. The orbital distance of major bodies and the Kuiper Belt boundaries are also shown. The y-axis reflects the transfer time in years to fly from perihelion to aphelion in such an orbit. The middle plot shows the same x-axis and notations but instead provides the time spent by the spacecraft in the Kuiper Belt on the y-axis. Finally, the bottom plot shows the launch energy required to achieve the aphelion value reflected on the x-axis. Even though the spacecraft trajectories contained in these plots are very basic and un-optimized, they nevertheless provide an indication of whether reaching a target is achievable within a certain time-frame or not. Therefor several interesting statements can be made with support of the data in these two plots.

In the top figure it can be seen that with this kind of trajectory it will take 18 to 30 years to reach the Kuiper Belt. These 30 years can be interpreted as an upper boundary for how long a flight to the Kuiper Belt should reasonably take. The second plot shows that as the aphelion rises beyond 30 AU, the time spent in the Kuiper Belt rapidly increases as well. This would indicate that a trajectory that reaches, for example, just 35 AU would be sufficient for long-term Kuiper Belt exploration. However, as discussed in Section 2.2, the majority of KBOs are orbiting at distances of between 39 and 48 AU from the Sun. For this reason a more distant aphelion would thus be preferable.

The bottom plot shows that the required launch energy for these trajectories are relatively high, with aphelion distances beyond 40 AU requiring a C_3 of over 140 km^2/s^2. These values are comparable to the 157.75 km^2/s^2 launch performed for the New Horizons mission, and thus reflect a similar limited payload mass capacity. The goal of this study will be to find trajectories that achieve similar or better values for transfer time and time spent in the Kuiper Belt, but with a lower launch energy requirement.

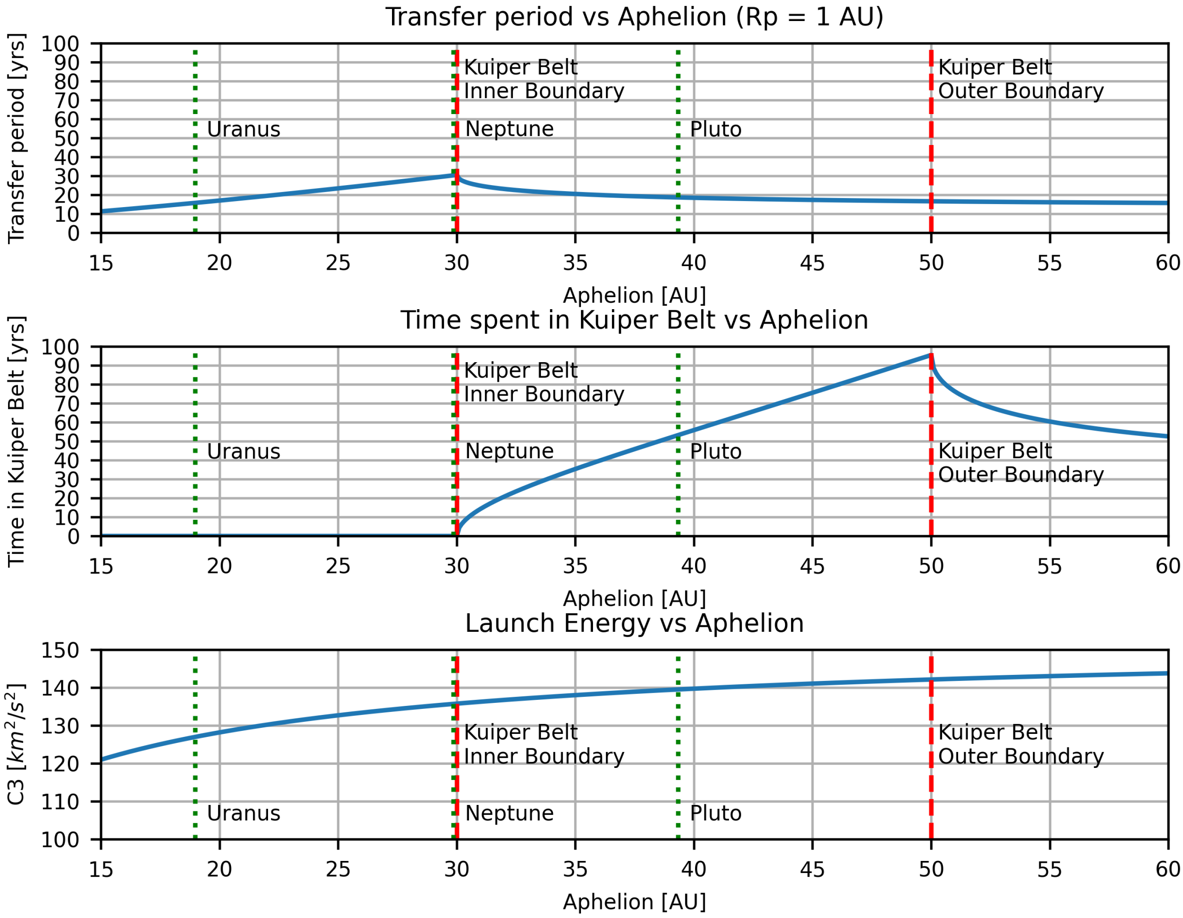

Figure 2.13: Plots of aphelion distance versus transfer time (top), time spent in Kuiper Belt (middle), and the required launch energy (bottom).

The type of orbit reflected in these plots are certainly not optimized space mission trajectories: the transfer time typically exceeds 20 years while still requiring a launch energy at the upper limit of what is possible with current launch vehicles. Finding more efficient trajectories which allow spacecraft to enter the Kuiper Belt sooner, spent more time in the target region, or allow the deployment of more payload mass are the goal of this study. This can be achieved by performing gravity assists and intermediate propulsion burns, changing the characteristics of the orbit over the course of the mission. In the velocity profiles shown earlier in Figure 2.9 it was noted how the heliocentric velocity of the Voyager 2 probe was actually reduced during its Neptune flyby. This inspires the idea to utilize inner Solar System planet gravity assists to increase the velocity in order to reach the Kuiper Belt earlier, and then using planets Uranus or Neptune in order to remain in the Kuiper Belt longer.

3

Mission Characteristics

In this chapter several fundamental characteristics of the mission are defined. Section 3.1 describes the launch scenario of the mission, including a discussion on the launch energy parameter. Sections 3.2 and 3.3 define the flight time and propulsion methods respectively. Section 3.4 describes the use of gravity assists and deep space maneuvers, further constraints on the trajectory search space are subsequently discussed in Section 3.5. Section 3.6 provides some background information on the characteristics of a spacecraft that would be suitable for the envisioned mission. Finally, in Section 3.7, examples are given of noteworthy mission challenges that are regarded as out of scope of this project.

It should be noted that parts of the content of this chapter find their basis on findings documented in the literature study performed by the author. For a more in-depth discussion on most of these topics the reader is referred to this document [26].

3.1. Launch Scenario

A launch period has to be defined in order to limit the trajectory search space and, perhaps equally important, to define a certain technological development level on which launcher and spacecraft capabilities can be based. For this particular project the launch epoch is set between January 1st of 2025 and January 1st of 2040. An earlier launch epoch could be included but with development and production of the spacecraft in mind the year 2025 is set as a earliest launch year. This research project is intended as a feasibility analysis for the relative near future, corresponding with a launch before the year 2040.

The launch energy parameter C_3 is used to quantify the velocity a launch vehicle can provide to its payload. For hyperbolic trajectories C_3 is equal to the square of the asymptotic velocity at infinite distance denoted by V_∞. The C_3 value is heavily dependent on the mass of the payload; an increased payload mass will result in a reduced C_3 value and thus a reduced V_∞ value. A graph indicating C_3 versus the payload mass of various heavy-class launch vehicles is given in Figure 3.1. The C_3 performance of a launch vehicle can be improved by adding a third stage such as the Star48B used by the New Horizons launcher. The improvement this provided to the C_3 curve of the Atlas V 551 launch vehicle, a configuration which was used for New Horizons, is visible in Figure 3.2. Documentation of the New Horizons launch in the New Horizons Mission Design Report [33] provides insight in how the interplanetary trajectory is set up and performed. The New Horizons spacecraft with an attached Star48B solid rocket motor was placed into an elliptical parking orbit of perigee altitude 165 km and apogee altitude 215 km. After a short coast the booster was ignited and expended, providing New Horizons with the required velocity to intercept Jupiter little over a year later. The delta V required for New Horizons to reach Jupiter was completely provided by the launch vehicle. For the launch of a Kuiper Belt mission it is assumed that the same scenario can be implemented. The launch vehicle provides enough velocity for the spacecraft to be on route for its first planetary flyby. Maneuvers after this interplanetary orbit insertion will be powered by the onboard propulsion system of the spacecraft.

During the heritage review in Chapter 4 of the literature study it was observed that missions which use Venus, Earth, or Mars as a first gravity assist opportunity will launch with a C_3 value of at maximum 36 km^2/s^2. Missions which use Jupiter as their first flyby planet need far more excess hyperbolic velocity, resulting in a C_3 ranging from 100 to 158 km^2/s^2. Optimization of trajectories in this project will reflect this heritage and limit the C_3 to either 36 or 100 km^2/s^2, depending on the first flyby planet. A low C_3 launch is preferable as it allows for an increased payload capacity, or a reduction of cost by allowing the use of a less powerful launch vehicle.

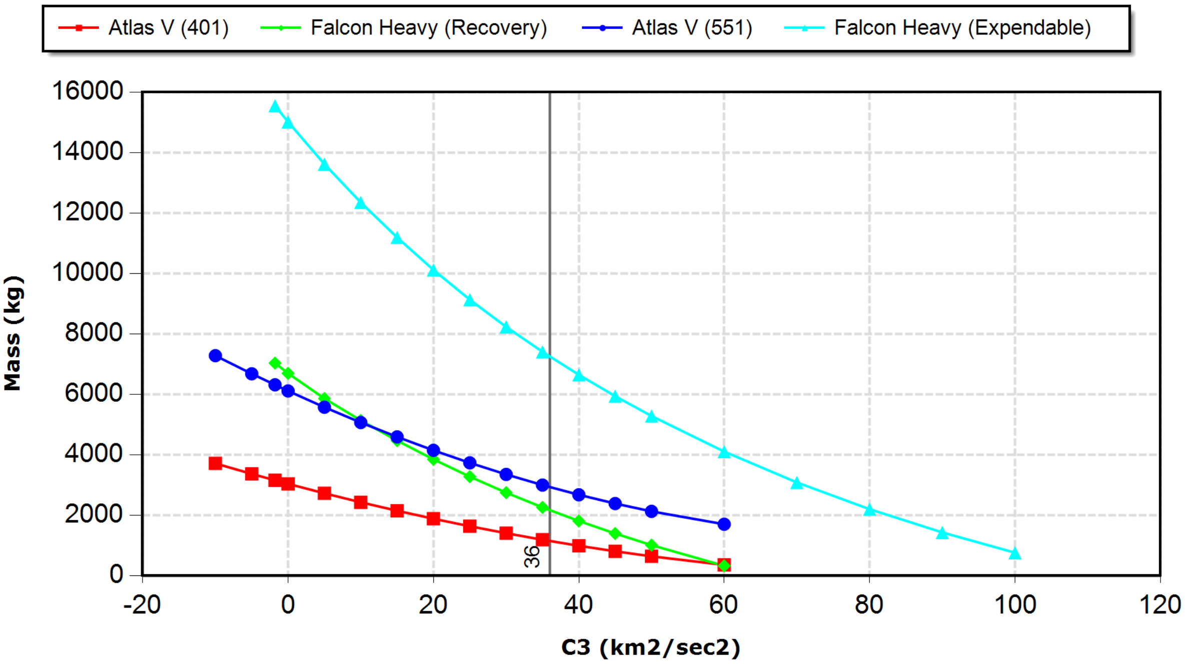

Figure 3.1: C_3 versus payload mass graphs of several currently used launch vehicles [34].

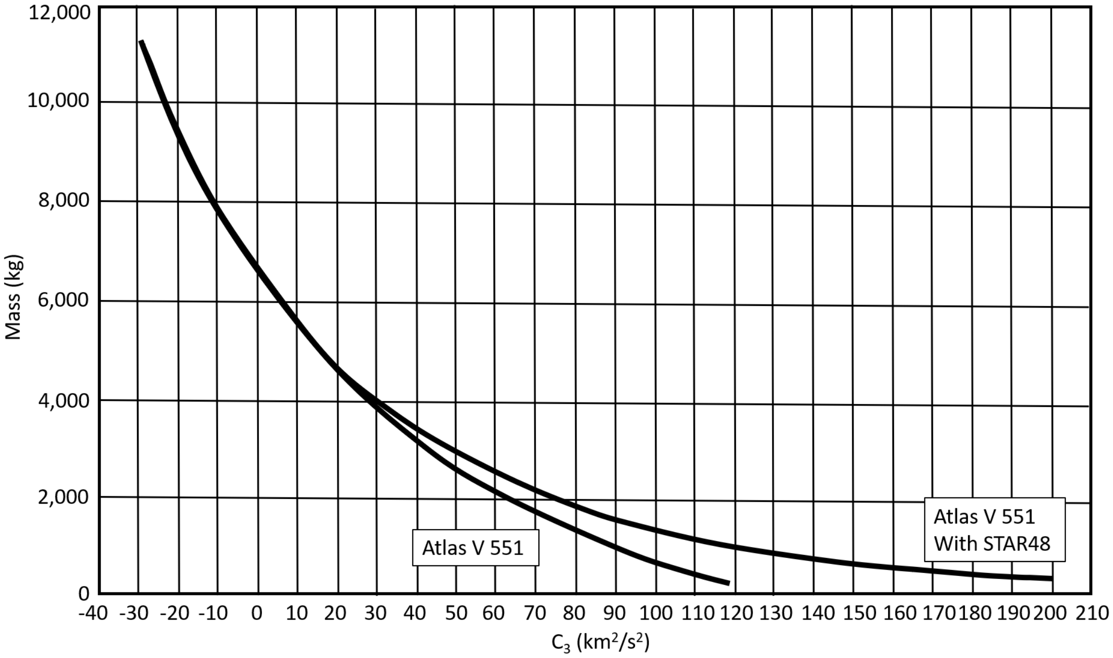

Figure 3.2: C_3 versus payload mass graph of the Atlas V (551) launch vehicle with and without a STAR48 booster stage. Data from [35].

3.2. Flight Time

The flight time is defined as the time between the date of launch and the date upon which a radial distance of 30.5 AU from the Sun is reached. Note that it does not reflect the total mission duration but merely but merely the flight time between launch and entry of the Kuiper Belt region. The use of 30.5 AU to signify the inner boundary of the Kuiper Belt instead of exactly 30 AU will be explained in Section 4.5.2. For a mission to the Kuiper Belt this flight time is a critical feasibility criterion. A maximum flight time of 25 years to enter the Kuiper Belt region is established based on the mission studies and proposals discussed in Section 2.3. The KBO trajectory studies by Mcgranaghan et al.[1], Zangari et al.[2], and Gleaves et al.[28], all define 25 years as the maximum time of flight. Of course, a key aspect of this study will be to investigate if shorter time-of-flight missions are possible as well.

3.3. Propulsion Type

A thorough investigation into propulsion methods was performed as part of the literature study preceding this thesis. The considered propulsion methods were conventional chemically-powered high-thrust, electrically-powered low-thrust, and solar radiation pressure propelled solar sails. The selected propulsion method is conventional high-thrust. The low-thrust electrical propulsion method could be very interesting for further study but the high electrical power requirement makes it a difficult fit for a mission that mostly takes place at large distances from the Sun where solar arrays are effectively useless. The solar sail method possesses a similar problem as its efficiency is almost solely dependent on the distance between the spacecraft and the Sun. At time of writing solar sails are furthermore only tested in practice on relatively small spacecraft.

An electrically powered low-thrust propulsion method should nonetheless be seriously considered were a follow up study be performed. The 2007 thesis by TU Delft alumnus Jeroen Melman included a limited study of a low-thrust trajectory to Neptune. Melman's work shows promising results. Melman does draw the same conclusion as was drawn in the literature study, noting that as the radial distance from the Sun increases the available power and thrust rapidly decreases. The required and available thrust acceleration for Melman's low-thrust solution can be seen in Figure 3.3. At a radial distance of 3.37 AU the required thrust acceleration is triple that of the available thrust. The trajectory found by Melman does not include gravity assists; including these would be an important step to expand upon his work.

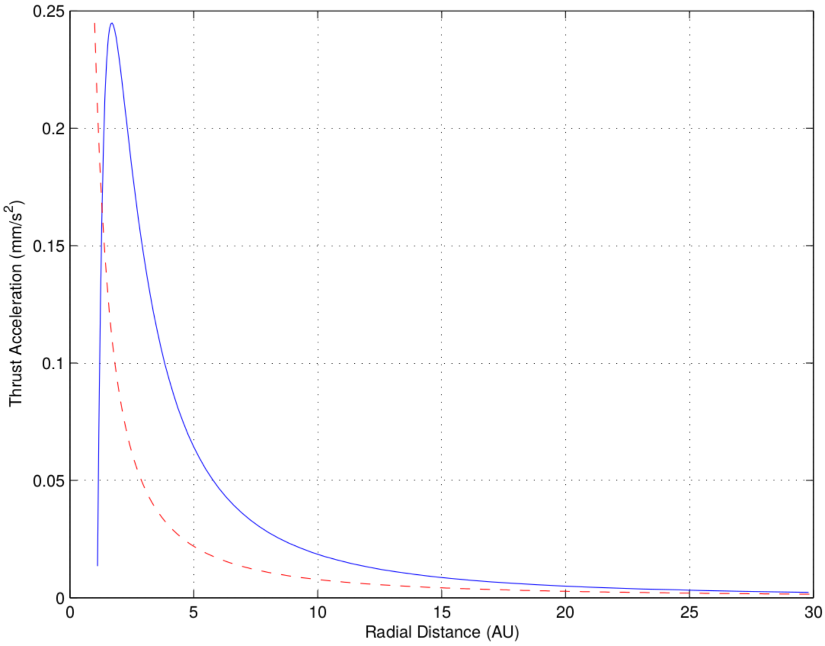

Figure 3.3: The negative mismatch between the available thrust (red) and the required thrust (blue) in the low-thrust solution to Neptune by Melman [36]. This mismatch is indicative of the challenge of using low-thrust electric propulsion for missions to the outer planets.

3.4. Gravity assists and Deep Space Maneuvers

The mission trajectory search space will include the use of planetary gravity assists and Deep Space Maneuvers (DSMs). To simplify the optimization process and manage the quantity of solution variables, the application of DSMs will be limited to one instance per interplanetary transfer leg. Most common gravity assist planets for deep space missions were identified to be Venus, Earth and Jupiter in the literature study. The complete list of planetary flyby sequences that are evaluated for a mission to the Kuiper Belt in this study is documented in Chapter 8.1.

3.5. Trajectory Constraints

In this section the constraints on the trajectory search space are further defined. A launch data search space between 2025 and 2040 was already established in Section 3.1. The maximum time of flight to the Kuiper Belt was set at 25 years in Section 3.2. In this section the constraints on the trajectory after launch are determined.

Most importantly the minimum flyby distance around planets has to be determined. These values will have significant effects on the solution quality and the problem search space. The flyby distance of a planet is often defined as the distance between the planet center and the position of the spacecraft at closest approach as shown in Figure 3.4. For some planets the minimum distance is relatively easy and straightforward to determine. For Venus, Earth, and Mars the minimum flyby distance is set at 1.15 times the planetary radius of the respective body. This ensures that the periapse distance is well above the atmosphere and that any atmospheric drag effects are negligible. For the outer planets Jupiter, Saturn, Uranus, and Neptune the choice of a minimum flyby distance is less straightforward and arguably also dependent on spacecraft design. These planets introduce hazards such as excessive radiation or hazardous ring systems. For these planets minimum distances from heritage missions and previous studies are used for guidance. Zangari et al. [2] state that they employ a minimum radii distance of 1.1 for all outer planets except Jupiter, which they argue requires a 3.0 radii minimum approach distance due to its exceptionally high radiation output. Meanwhile the Triton proposal in Hansen et al.[22] has a Jupiter flyby distance of 2.24 Jupiter radii and the NASA Pioneer 11 mission approached Jupiter up to a distance of 1.6 Jupiter radii. Based on these and other references it is ultimately decided to set a constant minimum distance of 1.7 radii for the outer planet flybys. While this is quite a close approach for a Jupiter flyby it has been performed in the past and can be compensated with radiation shielding on the spacecraft if necessary. Furthermore the true Jupiter flyby distance for the optimized solutions will be investigated upon at the end of the project to see if such a close flyby is necessary.

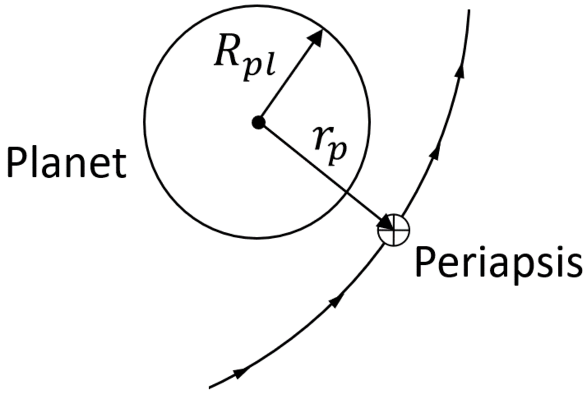

Figure 3.4: The flyby distance r_p during a gravity assist is typically measured between the planet center and the orbit periapsis, and often indicated in units of the respective planet mean radius R_{pl}.

In terms of thermal constraints a somewhat arbitrary Sun approach limit of 0.5 AU is set; this limit ensures that the spacecraft will not require exceptional onboard thermal management systems. Based on previous space missions and studies it is deemed unlikely that reducing the Sun approach limit further would lead to improved results.

For convenience a summary of the minimum flyby distances of the planets and the Sun is given in Table 3.1.

Planet	Merc.	Venus	Earth	Mars	Jupiter	Saturn	Uranus	Neptune	Sun
r_{min} [Radii]	1.15	1.15	1.15	1.15	1.7	1.7	1.7	1.7	0.5 AU

Table 3.1: Minimum flyby distance of the Sun and the Solar System planets in order to avoid significant atmospheric drag and excessive radiation/heat.

3.6. Spacecraft Characteristics

While the focus of this thesis is on trajectory design, some characteristics of the spacecraft can be deduced from past missions in order to create an indication of the design of the spacecraft this mission would require. The minimum spacecraft mass and the propulsion efficiency are based on data from the New Horizons spacecraft. Table 3.2 indicates a scientific payload mass of 32.7 kg which is comparable to the approximate 30 kg of payload mass of New Horizons. The slight difference in mass is due to the addition of a dedicated magnetometer instrument. Based on the 401 kg dry mass of New Horizons, a conservative minimum dry mass of 450 kg is assumed for our Kuiper Belt spacecraft.

Instrument	Power [W]	Mass [kg]
Imaging device	5.1	8.6
IR/UV spectrometers	9.3	14.8
Particle detector	6.5	1.8
Plasma detector	4.6	4.4
Magnetometer	3.1	3.0
Radiometer	2.1	0.1
Total	30.7	32.7

Table 3.2: Overview of common spacecraft instruments, their power requirement, and their mass. Mass and power requirement is based on data from New Horizons [37]. Magnetometer data are from Cassini [38].

Since the propulsion method can have a significant effect on the deployable spacecraft mass, an engine I_{sp} value of 250 s can be assumed based on Table 3.3.

Mission	Thrust [N]	I_{sp} [s]	Propellant [kg]	ΔV [m/s]
Voyager 2	4×0.9	227	104	190
Cassini Huygens	445	307	2,978	2,400
New Horizons	4×4.4	215	77	290

Table 3.3: Performance data of a selection of interplanetary space missions.[39] [30][40]

The extreme distance from the Sun introduces another challenge: diminished and effectively non-existent power generation from solar panels. Both Voyager probes and the New Horizon spacecraft made use of an RTG to generate power. The RTG on New Horizons provided 245.7 W at launch which has decayed to 190 W by January 2019. Power output is predicted to decay too far to power the spacecraft's transmitters in the 2030s. This indicates that for a very long-duration Kuiper Belt trajectory a more advanced or larger RTG is likely required [41].

3.7. Out of Scope Mission Challenges

The challenges considering long-distance communication, power management, and the technology required to allow long-distance observation of relatively small KBOs are considered out of scope for this project. However, an important aspect that should be mentioned is the challenge of performing measurements on the multitude of distant objects from within the Kuiper Belt. The question of how closely the probe must approach a KBO for it to be able to gather valuable scientific data with its onboard instruments would need to be answered. New Horizons closest approach distance to KBO Ultima-Thule was 3,500 km, the image in Figure 2.8 was created using data gathered from a distance of approximately 6,630 km [16]. The chance that a spacecraft achieves such close proximity encounters with a trajectory that is not optimized for one specific encounter is incredibly small. Ultimately, however, the maximum distance at which useful data can be obtained is dependent on the scientific instruments aboard the spacecraft. New Horizons' main mission objective was to return data on dwarf planet Pluto, not on the significantly smaller Kuiper Belt objects it could possibly encounter after this objective was completed. For now this study will focus on identifying spacecraft trajectories that enable long flight times in the Kuiper Belt and assume that the required instruments to make such a mission scientifically valuable are technologically feasible. It is likely that these instruments would be larger and heavier than the instruments aboard New Horizons. With this in mind a valuable research goal is to find launch scenarios which enable a large payload mass. One could envision a probe which features a large telescope instrument comparable in mass to the one aboard the Kepler Space Telescope, an Earth trailing heliocentric spacecraft with a dry mass of approximately 1,050 kg [42].

4

Trajectory Design Method

This chapter encapsulates the considerations and methods to create the trajectory design model. This process starts with discussing the assumptions that were made in Section 4.1. Then in Section 4.2 an introduction is given on Tudat, the TU Delft Astrodynamic Toolbox. Tudat was used to create the mission design model and three of its most used functions are described in Section 4.3. These functions are extensively used in the trajectory design library of Tudat, which was adjusted, and are discussed in Section 4.4. To adapt the existing functionalities of Tudat to optimize trajectories for the proposed long-duration Kuiper Belt flight, several new functionalities were written, these are explained in Section 4.5. Finally the verification of the model and functions is discussed in Section 4.6.

4.1. Model Assumptions

Efficient optimization of interplanetary trajectories is a complex problem. The system of gravitational attraction between the Sun and the planets creates a complex dynamic system of bodies. The environment is constantly changing as a function of time as the planets rotate around the Sun. With this rotation the start and end conditions of the problem, as well as the location and geometry of the optimal gravity assists, continuously change over time as well. To efficiently and effectively evaluate the problem search space, several assumptions are therefor made. These assumptions are typically used in the first phase of optimizing interplanetary trajectories. This first phase of trajectory optimization is done in what is commonly called the first-order analysis. The first-order analysis is sufficiently accurate to provide initial solutions which can then be further evaluated during subsequent, more detailed, studies.

In the first-order analysis perturbations are typically neglected. The absolute magnitude of perturbing forces is much smaller than that of the main forces. In an interplanetary trajectory the main force is almost always the gravitational pull of the Sun. Only during the brief planetary flybys is the gravitational pull of the body around which the flyby is performed the dominant force. Because these planetary flybys have a very short duration, the patched-conics assumption can be used. In the patched-conics assumption a succession of two-body formulations is used in which the Sun and the planets alternate as the central body. The model thus alternates between heliocentric and planetocentric reference frames. The gravity assists and moments of high-thrust propulsion are modeled as instantaneous maneuvers and velocity changes.

In subsequent steps the perturbing forces do need to be included in the environment model. During interplanetary trajectories, especially trajectories with long flight times such as those proposed in this project, perturbations such as third-body effects and solar radiation pressure can be quite significant. Further perturbing forces are introduced during flybys and can be caused by irregularities in gravity fields or by atmospheric drag during close flybys of for example Earth or Mars. Finally, perturbing forces can be caused by electromagnetic effects due to the strong electromagnetic field that some planets possess or by relativistic effects. These last two perturbing forces are typically extremely small and negligible [36][43].

Despite the absence of perturbations in the patched-conics assumption model, effective optimization of high-thrust interplanetary trajectories is still a difficult process. The problem is therefor further simplified by specifying the swing-by planets within the optimization problem definition. Instead of including the quantity and sequence of gravity assists as part of the optimization problem, these variables are thus predetermined and set. Given that the Solar System contains eight planets and that the number of planets useful for a gravity assist is even more limited, this results in a manageable quantity of planetary flyby sequences to evaluate. Once the planetary sequence is fixed the problem becomes comparatively much simpler to solve but nevertheless remains complex. Further simplification is achieved by limiting the number of orbital revolutions per transfer between subsequent planetary flybys to one or a fraction thereof, and by only using a counter-clockwise transfer direction.

In more basic trajectory optimization models, high-thrust maneuvers are only performed at the moment a planetary flyby happens. This simplifies the problem significantly as this simplification fixes both the moment and the position that the high-thrust burns occur, which eliminates variables from the problem. Unfortunately, limiting the trajectory to only perform maneuvers at planetary flybys typically results in solutions that are sub-optimal. The trajectory result can often be improved with the addition of DSMs [44].

The NASA Messenger trajectory to Mercury, shown in Figure 4.1, used multiple DSMs in order to reach the target efficiently. The addition of these DSMs increases the complexity of the problem significantly as the position and time of a DSM burn is not fixed at the moment and position of a planetary flyby. Instead the DSM is performed somewhere in the transfer leg between two planets, introducing new variables to the problem which naturally need to be optimized. The additional variables make the search space of the problem more complex and highly oscillatory. Many local optima are present in the problem and the optimum solution is typically extremely sensitive to small variations in the decision variables. An example of the many sub-optima in the search space of two variables specifying a single DSM can be found in a figure produced by Molenaar [45] shown in Figure 4.2.

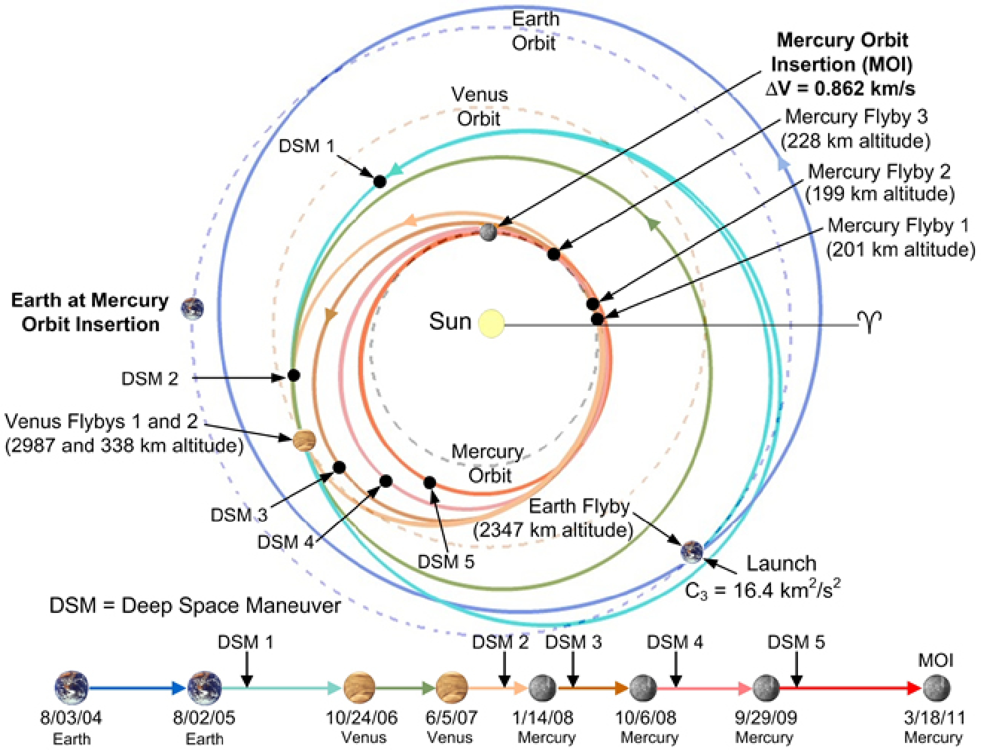

Figure 4.1: Overview of the launch, planetary flybys and DSMs used by the Messenger spacecraft to prepare for Mercury orbit insertion. The total amount of delta V applied by DSM 1 to DSM 5 was 1,039.8 m/s. [46].

Musegaas concludes in his 2012 thesis that the inclusion of DSMs in 24 trajectories to Saturn resulted in a doubling of the deployable final spacecraft mass on average. Musegaas also describes how the inclusion of powered swing-bys concurrently with DSM burns results in an additional 7.8% average improvement on the final spacecraft mass [44]. The 24 trajectory problems Musegaas used to draw this conclusion all had 18 decision variables. The trajectories which will be optimized in this project will often contain more variables, with some problems containing over 30 variables. To increase the likelihood of adequate optimization of the solutions for these trajectory problems the powered flyby is not included in the trajectory model of this project. This means that all gravity assists will be unpowered. This simplification reduces the number of variables in all trajectory problems by one per planetary swing-by. The unpowered multiple gravity assists with one DSM per leg trajectory model is referred to as the unpowered MGA-1DSM model in this thesis.

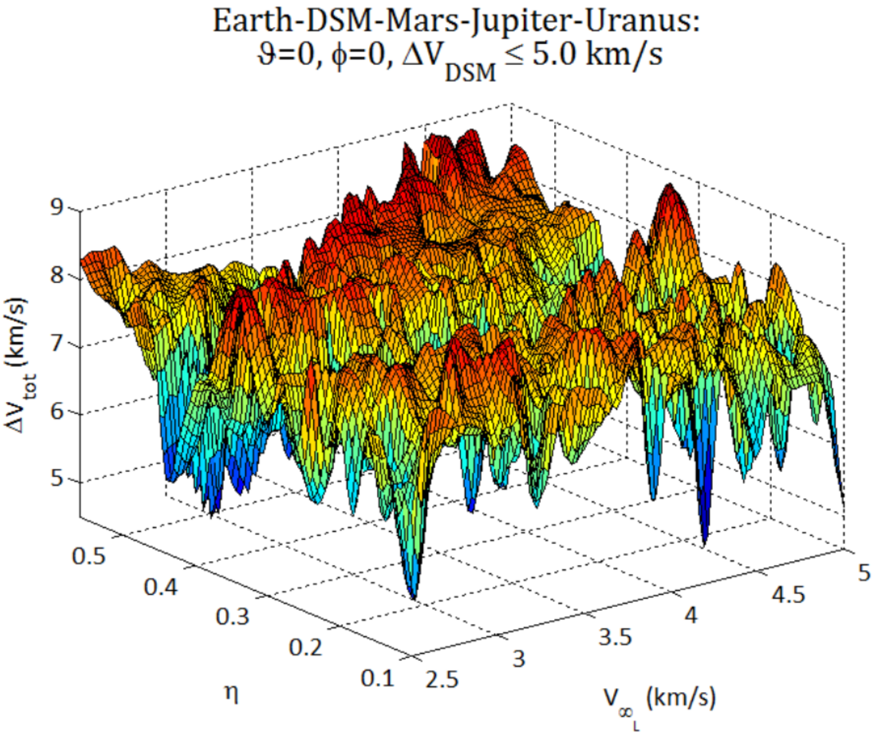

Figure 4.2: Plot showing the total delta V as a function of two variables specifying a single DSM in a trajectory to Uranus. To create this plot a grid sampled search space was evaluated in which two of the DSM variables were varied and the remaining two were fixed. Note that a typical trajectory contains multiple DSMs, all with a similar structure of minima and quantity of sub-optima [45].

4.2. Tudat

The astrodynamic functions described in Section 4.3 and the trajectory model described in Section 4.4 are part of the Tudat library. Tudat is the astrodynamic toolbox created and continuously under further development by the TU Delft. In the past different astrodynamic toolboxes such as OPTIDUS and GALOMUSIT were used by the students and faculty members of the aerospace department. Ultimately these different toolboxes were merged into the Tudat toolbox in order to create a more structured and complete software package and to prevent students from frequently reinventing the wheel during their projects. Tudat is written in the C++ programming language in order to facilitate a fast computation speed. Tudat is set up as an open-source modular software library that contains a wide variety of functions and features. These functions are written to be robust and well-tested before they are included in the stable release of the software package. Tudat has been used extensively in research projects and documentation of the toolbox can be found on the website *tudat.tudelft.nl*

4.3. Astrodynamic Functions

The functions described in this section are used extensively and are in many ways the building blocks of the trajectory model which will be explained in Section 4.4. The first topic which will be discussed is the Kepler propagator in Section 4.3.1. Subsequently, Section 4.3.2 explains the Lambert targeter. The last of the three functions to be discussed is the gravity assist propagator in Section 4.3.3.

4.3.1. Kepler Propagator

This section describes the Kepler propagation function. The Kepler propagator is a function that takes a state in traditional Keplerian elements and an initial epoch and propagates that state to a final state at a given final epoch. This can be formulated as: given S_i and time t_i, find S_f at time t_f. Propagation of the orbit is done under the assumption of an unperturbed Keplerian orbit which makes five of the six variables describing a Kepler orbit static. The only variable dependent on time is the true anomaly θ. Kepler propagation makes use of this fact to solve the orbit propagation problem as it reduces the problem to find a method that relates time to the true anomaly. The formulas used for this calculation differ slightly for elliptic and hyperbolic orbits, both of these scenarios are discussed in this section. The calculation for parabolic orbits is not supported by Tudat, but given that an orbit with an eccentricity of exactly one rarely happens in practice, this does not have ramifications for the implementation of the trajectory model. All methods and formulas in this section are taken from Chapters 6 and 8 of Wakker [43].

The first step is to transform the initial true anomaly, θ_i to the initial eccentric anomaly, E_i or initial hyperbolic eccentric anomaly F_i for the hyperbolic orbit case, by using Equations 4.1 or 4.2, where e is the orbit eccentricity.

$$E_i = 2\arctan\left(\sqrt{\frac{1-e}{1+e}} \cdot tan\frac{\theta_i}{2}\right) \tag{4.1}$$

$$F_i = 2\,\mathrm{arctanh}\left(\sqrt{\frac{1-e}{1+e}} \cdot tan\frac{\theta_i}{2}\right) \tag{4.2}$$

The eccentric anomaly is then transformed to the initial elliptic mean anomaly, M_i, or the initial hyperbolic mean anomaly, $\overline{M}_i$ is found using Equations 4.3 and 4.4.

$$M_i = E_i - e\sin(E_i) \tag{4.3}$$

$$\overline{M}_i = e\sinh(F_i) - F_i \tag{4.4}$$

From the initial mean anomalies, the final mean anomalies can be calculated using the central body gravitational parameter μ and the orbit semi-major axis a in Equations 4.5 and 4.6.

$$M_f = M_i + \sqrt{\frac{\mu}{a^3}}(t_f - t_i) \tag{4.5}$$

$$\overline{M}_f = \overline{M}_i + \sqrt{\frac{\mu}{-a^3}}(t_f - t_i) \tag{4.6}$$

Transformation of these final mean anomalies to their final eccentric anomalies can not be done analytically but instead has to be done using a root-finder function. In Tudat the root-finding algorithm that is used for this is Newton-Raphson, described by Equations 4.7 and 4.9. Musegaas notes in his thesis that the initial guess for these root finders is important as the scheme can become unstable with select initial values. The most stable initial guess for the elliptic mean anomaly was found to be M±e as described in Equation 4.8; for the hyperbolic variant Tudat uses the initial guess procedure described by Wakker resulting in the condition statements shown in Equation 4.10.

$$E_{k+1} = E_k - \frac{f(E_k, M)}{\frac{d}{dE}(f(E, M))|_{E=E_k}} = E_k - \frac{E_k - e\sin(E_k) - M}{1 - e\cos(E_k)} \tag{4.7}$$

$$E_0 = \begin{cases} M + e, & \text{if } M_{\text{mod }(2\pi)} \leq \pi \\ M - e, & \text{if } M_{\text{mod }(2\pi)} > \pi \end{cases} \tag{4.8}$$

$$F_{k+1} = F_k - \frac{f(F_k, \overline{M})}{\frac{d}{dF}(f(F, \overline{M}))|_{F=F_k}} = F_k - \frac{F_k - e\sinh(F_k) - \overline{M}}{1 - e\cosh(F_k)} \tag{4.9}$$

$$F_0 = \begin{cases} \sqrt{\frac{8(e-1)}{e}} \cdot \sinh\left(\frac{1}{3}\operatorname{arcsinh}\left(\frac{3\overline{M}_f}{\sqrt{\frac{8(e-1)}{e}}(e-1)}\right)\right), & \text{if } |\overline{M}_f| < 6e \\ \ln\left(\frac{2\overline{M}_f}{e}\right), & \text{if } |\overline{M}_f| > 6e \\ -\ln\left(\frac{-2\overline{M}_f}{e}\right), & \text{if } |\overline{M}_f| < -6e \end{cases} \tag{4.10}$$

After the final mean anomaly has been found by the root-finder, the true anomaly θ_f at the final epoch t_f can be calculated using either Equation 4.11 for the elliptic orbit case, or Equation 4.12 for the hyperbolic orbit case. By substituting this final true anomaly into the position of the initial true anomaly in the initial state vector S_i, the final body state S_f is found. With standard techniques not described here, the full three-dimensional position and velocity of the spacecraft at epoch t_f can be readily obtained.

$$\theta_f = 2\arctan\left(\sqrt{\frac{1+e}{1-e}} \cdot \tan(\frac{E_f}{2})\right) \tag{4.11}$$

$$\theta_f = 2\arctan\left(\sqrt{\frac{1+e}{1-e}} \cdot \tanh(\frac{F_f}{2})\right) \tag{4.12}$$

4.3.2. Lambert Targeter

A Lambert targeter is an algorithm which can solve Lambert's problem. The input into this problem is the initial position vector $\vec{r}_1$, the final position vector $\vec{r}_2$, and the time-of-flight for the problem that needs to be solved t_f. The typical geometry for this problem is given in Figure 4.3. In the interplanetary trajectories of this project the central body is always the Sun when Lambert's problem is solved. P_1 represents the position of the departure planet at time t_1. P_2 represents the position of the arrival planet at time t_2. The flight time t_f is the difference between times t_1 and t_2. Lambert's problem can be solved over an angle θ or over an angle $2\pi - \theta$ in the opposite direction. Furthermore cases exist where the angle θ is not bound between 0 and 2π but instead allows $k2\pi + \theta$ solutions where multiple revolutions around the central body are performed before the arrival position is reached. As discussed in Section 4.1 the multiple revolution and clockwise solutions will not be considered in this thesis [43].

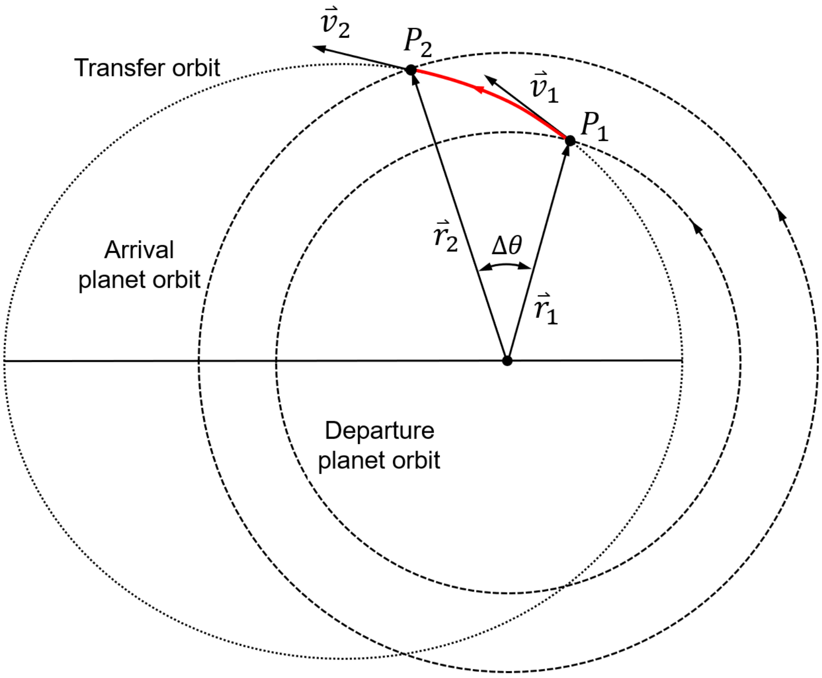

Figure 4.3: Schematic representation of Lambert's problem [47].

To solve Lambert's problem the flight time equation shown in Equation 4.13 needs to be solved.

$$t_f = \sqrt{\frac{a^3}{\mu}}\left[E_2 - E_1 - e(\sin(E_2) - \sin(E_1))\right] \tag{4.13}$$

Typically the variables in Equation 4.13 are rewritten and isolated for specific geometric cases. Wakker describes an analytical method in which four different cases are described which can then be solved using equally as many representations of the equation shown in Equation 4.13 [43]. In Tudat two main methods to solve Lambert's problem are implemented. One implementation is based on the theorem proposed by Lancaster and Blanchard [48], with improvements implemented as proposed by Gooding [49]. The second algorithm is a different method which was developed by Izzo. The algorithm by Izzo builds upon the Lancaster and Blanchard approach but makes use of a new variable, usable in all problem cases, to express the time of flight equation. With this new variable the time of flight curves are approximated using piece-wise continuous lines which can be used to solve the approximated problem using an iterative method and an initial guessed solution. When compared to the method by Gooding, the method developed by Izzo produces equally accurate results but with significantly smaller computational complexity [50]. Based on this faster computation speed the algorithm by Izzo will be used in this thesis.

4.3.3. Gravity Assist Propagator

This section describes the gravity assist calculator and propagator used in this thesis. As discussed in Section 4.1, all planetary flybys in this thesis will be un-powered. The discussion of the gravity assist calculation will thus be limited to the un-powered variant.

To start, the basic principle of the gravity assist is presented. During the approach of a planet the gravitational influence of that planet on the spacecraft will gradually increase. Ultimately the gravitational force of the planet will become the dominant force acting on the approaching spacecraft at which point the spacecraft has entered the planet's Sphere Of Influence (SOI). When the patched-conics assumption is used this portion of the spacecraft trajectory is modeled in a non-rotating planetocentric reference frame. During the flight through the SOI the interaction between the planet and spacecraft causes a change in the velocity vector of the spacecraft and planet. This interaction can be represented mathematically using Equation 4.14, with mass m, heliocentric velocity V, and where subscript sc represents the spacecraft and subscript pl represents the planet. The subscripts i and f represent the initial and final state respectively.

$$m_{sc} \cdot \vec{V}_{sc_i} + m_{pl} \cdot \vec{V}_{pl_i} = m_{sc} \cdot \vec{V}_{sc_f} + m_{pl} \cdot \vec{V}_{pl_f} \tag{4.14}$$

Equation 4.14 can be rewritten to Equation 4.15 which shows the velocity change that the spacecraft experiences as a result of the planetary flyby.

$$\Delta\vec{V}_{sc} = \vec{V}_{sc_f} - \vec{V}_{sc_i} = \left(\vec{V}_{pl_i} - \vec{V}_{pl_f}\right)\frac{m_{pl}}{m_{sc}} \tag{4.15}$$

Of course a spacecraft's mass is negligible in comparison to the mass of a planet, meaning that the planet's velocity remains practically unaffected over the course of the gravity assist.

With respect to the planet, the spacecraft enters the SOI at an initial hyperbolic velocity V_{∞_i} and exits at final hyperbolic excess velocity V_{∞_f}. Due to energy conservation the magnitude of the hyperbolic excess velocity before and after the flyby will be equal, but their directions will be different. Translating this velocity vector direction change to the heliocentric reference frame shown in Figure 4.4 illustrates the gravity assist effect. V'_{pl_i} is the velocity of the planet in the plane of the spacecraft's hyperbolic trajectory within the heliocentric reference frame. The image shown displays the effect of when a spacecraft passes behind the target planet and thereby increases its heliocentric velocity, from V_{sc_i} to V_{sc_f}. A spacecraft passing in front of the planet will result in the opposite effect, causing a effective heliocentric velocity decrease.

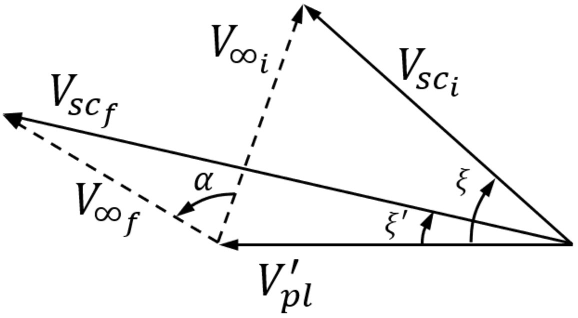

Figure 4.4: Velocity vector diagram of a gravity assist in the heliocentric frame.
Image adapted from [36]

In Figure 4.4 it can be seen that the magnitude and direction of the spacecraft's velocity vector before and after the flyby has clearly changed in the heliocentric reference frame. The amount and direction of this change depends on several parameters which are shown in Figure 4.5. This figure shows the geometry of the gravity assist within the planetocentric frame, again with the initial and final hyperbolic excess velocity shown. An important parameter that determines the flyby trajectory is the impact parameter B, which reflects the distance between the hyperbolic trajectory asymptote and the center of the flyby planet. V_p and r_p are the spacecraft velocity and radial distance at pericenter of the hyperbolic trajectory. Angle α is the asymptotic deflection angle, which describes the severity of direction change in the velocity vector. The relationship between the asymptotic deflection angle α, the approach distance r_p, and the hyperbolic excess velocity V_∞, is an important insight for effective gravity assist design, and will thus be further examined.

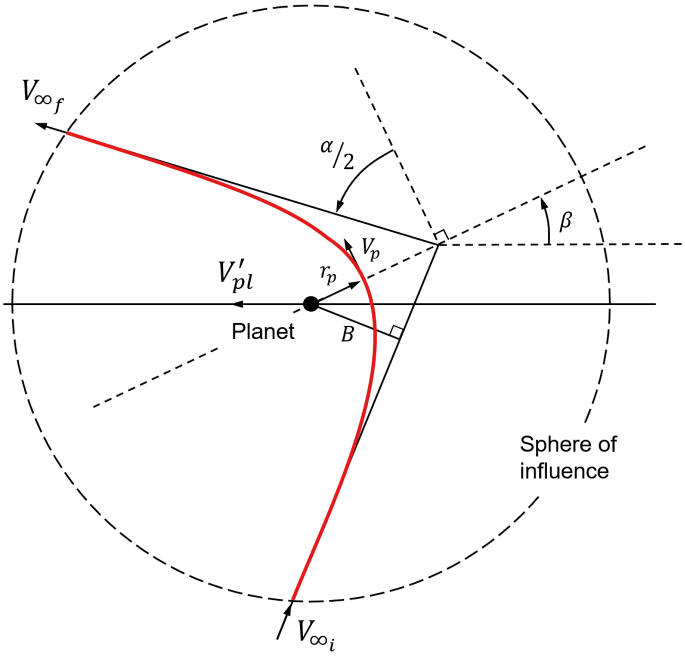

Figure 4.5: Representation of the in-plane geometry of a hyperbolic encounter trajectory. Image adapted from [43].

From Figure 4.5 and the principle that angular momentum of motion is constant for the entire trajectory about the planet, Equation 4.16 can be set up using the impact parameter B.

$$BV_\infty = r_p V_p \tag{4.16}$$

With the relation of the escape velocity at pericenter V_{esc_p} given in Equation 4.17 and the swing-by planet gravitational parameter μ_{pl}, Equation 4.16 can be rewritten to find the pericenter velocity V_p as shown in Equation 4.18 [43].

$$V_{esc_p} = \sqrt{\frac{2\mu_{pl}}{r_p}} \tag{4.17}$$

$$V_p^2 = V_{esc_p}^2 + V_\infty^2 = \frac{2\mu_{pl}}{r_p} + V_\infty^2 \tag{4.18}$$

which can be substituted into Equation 4.16 to obtain the equation for the pericenter radius r_p:

$$r_p = \frac{\mu_{pl}}{V_\infty^2}\left[\sqrt{1 + \frac{B^2 V_\infty^4}{\mu_{pl}^2}} - 1\right] \tag{4.19}$$

Using the relations for hyperbolic trajectories a relationship between the asymptotic deflection angle α and the orbit eccentricity e can be found, as shown in Equation 4.20 [43].

$$\cos\left(\frac{\pi}{2}+\frac{\alpha}{2}\right)=-\sin\left(\frac{\alpha}{2}\right)=-\frac{1}{e} \tag{4.20}$$

which can be further developed using the same hyperbolic trajectory relations to create Equation 4.21, which shows that the asymptotic deflection angle α is solely dependent on the trajectory periapse distance r_p, excess velocity V_∞, and the gravitational parameter of the planet μ_{pl}.

$$\sin\left(\frac{\alpha}{2}\right)=\frac{1}{1+\frac{r_p V_\infty^2}{\mu_{pl}}} \tag{4.21}$$

Given a pericenter distance, the relationship in Equation 4.21 is used in the trajectory model to calculate the bending angle. To calculate the bending angle in the third direction a new variable called the rotation angle b_{rot} is created. The definition of this new variable can be seen in Figure 4.6. $\tilde{V}_{in}$ is the incoming planetocentric velocity vector which is calculated by subtracting the heliocentric planet velocity from the incoming heliocentric spacecraft velocity as shown in Equation 4.22.

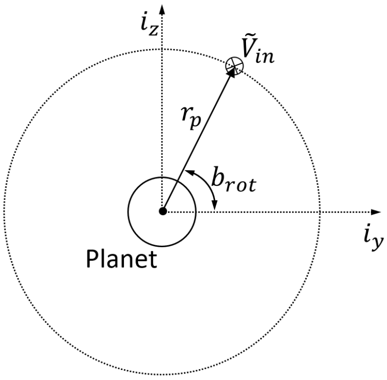

Figure 4.6: Definition of the 3D rotation angle b_{rot} [44].

$$\tilde{V}_{in}=\vec{V}_{in}-\vec{V}_{pl} \tag{4.22}$$

With the planetocentric incoming velocity calculated, the bending angle is calculated using Equation 4.23, a variation of the deflection angle equation shown in Equation 4.21.

$$\alpha=2\arcsin\left(\frac{1}{1+\frac{r_p|\tilde{V}_{in}^2|}{\mu_{pl}}}\right) \tag{4.23}$$

Using the coordinate frame defined with the unit vectors following the definitions shown in Equation 4.24, the outgoing planetocentric velocity vector $\tilde{V}$ is calculated using Equations 4.25. Then finally, using Equation 4.26, the heliocentric velocity vector $\vec{V}_{out}$ is found [51].

$$\vec{i}_x=\frac{\tilde{V}_{in}}{|\tilde{V}_{in}|} \tag{4.24a}$$

$$\vec{i}_y=\frac{\vec{i}_x\times V_{pl}}{|\vec{i}_x\times V_{pl}|} \tag{4.24b}$$

$$\vec{i}_z=\vec{i}_x\times\vec{i}_y \tag{4.24c}$$

$$\tilde{V}_{out}=|\tilde{V}_{in}|\cdot\left(\vec{i}_x\cos(\alpha)+\vec{i}_y\cos(b_{rot})\sin(\alpha)+\vec{i}_z\sin(b_{rot})\sin(\alpha)\right) \tag{4.25}$$

$$\vec{V}_{out}=\vec{V}_{pl}+\tilde{V}_{out} \tag{4.26}$$

4.4. Trajectory Model

The three astrodynamic functions discussed in Section 4.3 make up the majority of the trajectory model in Tudat. This trajectory model is used as a framework through which the entire trajectory problem is set up and subsequently optimized. The model consists of several sections called legs, which are joined together in order to create the full trajectory. The structure of the model is explained in more detail in Section 4.4.1. The individual legs that make out the model are discussed in more detail in Section 4.4.2. This section also lists the variables required to define an unpowered MGA-1DSM trajectory and the implementation of the newly developed reach leg. Section 4.5 then describes the method by which the trajectory fitness values DV, DSMDV, TTA, and TKB are calculated. Finally the verification method of the model and the trajectory fitness value calculations is discussed in Section 4.6.

4.4.1. Model Architecture

The trajectory model used in this thesis is an extension of the basic Multiple Gravity Assist (MGA) trajectory model. By adding a DSM, which requires additional parameters to define its location and moment of application, the potential of the trajectory model is expanded. The trajectory model used in this thesis implements DSMs according to the Velocity Formulation (VF). Tudat also supports an alternative DSM formulation called the Position Formulation (PF), which was shown by Musegaas in his thesis to be more difficult to optimize, and will therefor not be used in this thesis [44].

By combining the DSM-VF model with the MGA trajectory model, the Multiple Gravity Assist with 1 Deep Space Maneuver per leg using Velocity Formulation (MGA-1DSM-VF) model is created. Most trajectory models utilize one DSM per leg, as the first DSM typically results in the largest performance improvement. A schematic representation of the MGA-1DSM-VF model is shown in Figure 4.7. First the departure vector is specified at the departure planet. Using this specified vector the trajectory is propagated for a specified amount of time using the Kepler propagator discussed in Section 4.3.1. At that point the DSM is performed. The Lambert targeter discussed in Section 4.3.2 is subsequently utilized for the second part of the leg up to the point of entry into the SOI of the target swing-by planet. There the gravity assist propagator discussed in Section 4.3.3 is used to calculate the new departure velocity, and the process is repeated until the final planet is reached.

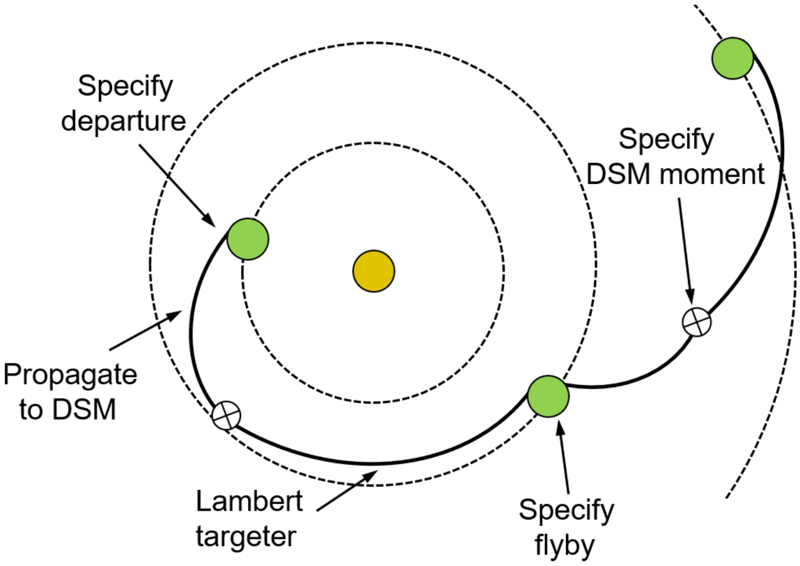

Figure 4.7: Schematic representation of the unpowered MGA-1DSM-VF model used in this thesis.

By excluding the powered gravity assist, as discussed in Section 4.1, the number of variables needed to define the DSM is reduced from four to three. Two of these variables are used to define the properties of the gravity assists, the remaining variable defines the moment at which the DSM is applied. The fourth possible variable, which would define the amount of Delta V added during the powered gravity assist, is thus excluded in this thesis.

As mentioned, the Tudat trajectory model is built up out of multiple legs, with a single leg indicating the transfer from one planet to another planet. The first leg is always the departure leg, starting in a particular orbit around Earth and ending when the SOI of the first target planet is reached. Departure from Earth and the insertion into a hyperbolic Earth escape trajectory is powered purely by the launch vehicle. The required energy for this launch and direct insertion is reflected by the C_3 parameter. The next leg can either be the capture leg, in case a direct transfer without gravity assists is modeled, or one or more subsequent planetary swing-by legs. Typically the final leg in the Tudat trajectory model is the mentioned capture leg. In the current version of Tudat the capture leg ends in a specified parking orbit around the final target planet. However, for this mission the trajectory does not end at the target planet but should instead continue on in a trajectory through the Kuiper Belt. To support this feature a new leg type, called the reach leg, was created which combines certain aspects of the capture and swing-by leg type. An overview of the four mentioned leg types is shown in Figure 4.8.

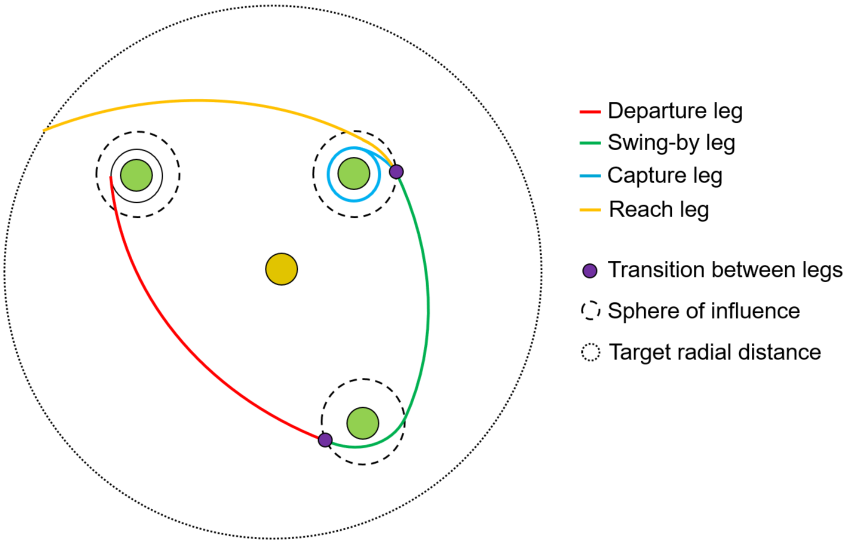

Figure 4.8: Schematic representation of the three default Tudat leg types, and the reach leg type developed for this thesis.

Regardless of type, each leg has the feature to calculate the required delta V, return the location and magnitude of the high-thrust maneuver, and to return the position of the spacecraft at specified regular time intervals. Each leg type also uses the same ephemeris data implementation, which is based on an approximate planet position calculation scheme as described in a document by Standish [52]. This ephemeris model is a simplified approximation as computational performance is preferred over high precision in the first-order trajectory design.

4.4.2. Model Legs and Variables

As discussed in Section 4.1, the unpowered MGA-1DSM-VF model used in this thesis makes the following assumptions to simplify the trajectory model:

- The patched-conics assumption is used.
- Orbit perturbations are neglected.
- High-thrust burns are only possible at departure and as DSMs between planetary flybys.
- One DSM is applied in each leg.
- All heliocentric transfers between planets are counter-clockwise.
- The Lambert targeter is limited to single-revolution solutions.

To form a specific trajectory, the model requires certain variables which are placed in what is called the variable vector or decision vector, denoted with $x(i)$. The number of elements in this vector is dependent on the number of planetary fly-bys that are performed in a trajectory. Each additional swing-by leg in the trajectory requires four additional variables to be specified. For the newly developed reach leg an additional fifth variable is required. The elements of the complete variable vector are described in this section.

The first variables in the vector define the departure time and the time of flight between transfer legs:

- t_0: the mission departure time.
- t_i: the time of flight of an interplanetary leg, for all i transfer legs of the trajectory.

The flyby time of the planets is calculated using these variables by using Equation 4.27, which is used to obtain the planetary position with use of ephemeris data.

$$t_{flyby_i} = t_0 + \sum_{j=1}^{i} t_j \tag{4.27}$$

For the departure leg the following four additional variables are required:

1. η_1: the fraction of time of flight variable t_1 at which the first DSM is performed ($\eta \in [0, 1]$).
2. V_∞: the magnitude of the hyperbolic excess velocity at departure.
3. θ: the in-plane angle for the hyperbolic excess velocity.
4. ϕ: the out-of-plane angle for the hyperbolic excess velocity.

For each swing-by leg the following three additional variables are required:

1. η_i: the fraction of time of flight variable t_i at which DSM i is performed ($\eta \in [0, 1]$).
2. b_{rot}: the rotation angle of the gravity assist.
3. r_p: the pericenter radius of the gravity assist.

Similar to Equation 4.26, the initial heliocentric departure velocity is calculated by adding the planetocentric velocity vector to the heliocentric velocity of the departure planet, as shown in Equation 4.28. The coordinate system used for this is established using the unit vectors shown in Equation 4.29 [51].

$$\vec{V}_{out} = \vec{V}_{pl} + \begin{bmatrix} \vec{i}_x \cos(\theta)\cos(\phi) \\ \vec{i}_y \sin(\theta)\cos(\phi) \\ \vec{i}_z \sin(\phi) \end{bmatrix} V_\infty \tag{4.28}$$

$$\vec{i}_x = \frac{\vec{V}_{pl}}{|\vec{V}_{pl}|} \tag{4.29a}$$

$$\vec{i}_z = \frac{\vec{r}_{pl} \times \vec{V}_{pl}}{|\vec{r}_{pl} \times \vec{V}_{pl}|} \tag{4.29b}$$

$$\vec{i}_y = \vec{i}_z \times \vec{i}_x \tag{4.29c}$$

After the heliocentric velocity is determined, the Kepler propagator described in Section 4.3.1 is used to propagate the orbit parameters to the point of DSM application. The moment of DSM application is calculated using Equation 4.30.

$$t_{dsm_i} = t_0 + \sum_{j=1}^{i} t_j + \eta_i t_i \tag{4.30}$$

At this point the Lambert targeter is utilized in order to calculate the required heliocentric velocity after DSM application, and the required heliocentric velocity on arrival at the SOI of the target planet. The DSM delta V is calculated by subtracting the heliocentric velocity before DSM application from the required heliocentric velocity calculated by the Lambert targeter. Following arrival at the SOI, the gravity assist propagator described in Section 4.3.3 is used to calculate the heliocentric departure velocity after the flyby. Using r_p and b_{rot} from the variable vector to solve Equations 4.23 and 4.25. Once the outgoing heliocentric velocity has been calculated, the process of Kepler propagation to DSM epoch, Lambert target calculation, and gravity assist propagation is repeated for all remaining swing-by legs, until the spacecraft arrives at the capture or reach leg.

As mentioned before, typically the final leg in the Tudat trajectory model is the capture leg. The capture leg is used to calculate the delta V required for orbital capture into a specified parking orbit around the target planet. The resulting delta V is then added to the total mission delta V used for the DSMs and departure burn, at which point the full trajectory has been calculated.

For a mission that aims to pursue a long-duration flight through the Kuiper Belt, orbital capture around a planet is clearly not a desired end of the trajectory. Instead the trajectory should set course for the Kuiper Belt after the final swing-by leg has been completed. To support calculations of such trajectories, a new final leg type is developed within the existing Tudat trajectory model. In this thesis this new leg type is called the reach leg, as it is utilized in order to reach the Kuiper Belt, or hypothetically any other significant region in the Solar System.

The initial segments of the reach leg are in large part identical to the swing-by legs discussed earlier in this section. However, as there is no specified target position vector but merely a certain specified radial distance from the Sun, there is no possibility of utilizing the Lambert targeter method after the gravity assist and Kepler orbit propagation have been performed. This also means that the time of flight between the last planetary swing-by and entry of the Kuiper Belt is not defined in the variable vector $x(i)$ but is instead a result of the previous variable vector parameters and the trajectory that results from these. Specifying the epoch of DSM application as a fraction of the flight time of this reach leg is therefor also not possible. The absence of the Lambert targeter also affects the method of the DSM magnitude calculation, as the Lambert problem solution indirectly calculates this value.

To still enable a DSM to be performed after the final gravity assist in the trajectory, the epoch of DSM application is instead specified as a fraction of an arbitrary time period of five Julian years. This DSM is applied tangentially to the established velocity vector and applied as shown in Equation 4.31, where V_{dsm_i} is the spacecraft velocity vector before DSM application and V_{dsm_f} is the velocity vector after DSM application.

$$\vec{V}_{dsm_f} = \vec{V}_{dsm_i} \left(\frac{\Delta \vec{V}_{dsm_r}}{|\vec{V}_{dsm_i}|} + 1 \right) \tag{4.31}$$

With this design, the reach leg requires specification of the following four additional variables:

1. η_r: the fraction of five Julian years at which the reach leg DSM is performed ($\eta \in [0, 1]$).
2. b_{rot}: the rotation angle of the gravity assist.
3. r_p: the pericenter radius of the gravity assist.
4. ΔV_{dsm_r}: the magnitude of the DSM applied in the reach leg.

As a consequence the problem dimension d, or the total number of variables in the variable vector $x(i)$, for a trajectory with n swing-by legs can be determined as follows:

$$d = 3n + 8 \tag{4.32}$$

4.5. Trajectory Fitness Values

In order to evaluate the quality of the trajectories they will be judged on several parameters. This section explains which parameters they are, why they are important, and how they are calculated. The delta V parameters DV and DSMDV are described in Section 4.5.1. Then Section 4.5.2 describes the Time To Arrival (TTA) parameter. Finally the value representing the time spent by the spacecraft in the Kuiper Belt, designated with TKB, is explained in Section 4.5.3.

4.5.1. DV and DSMDV

The total delta V required for a trajectory, consisting of both DV and DSMDV, is calculated by performing a summation of the following maneuvers:

- $|V_\infty|$: The magnitude of the hyperbolic excess velocity at departure.
- $|\Delta V_{dsm_i}|$: The magnitude of the DSMs applied in the departure and swing-by legs.
- $|\Delta V_{dsm_r}|$: The magnitude of the DSM applied in the reach leg.

By separating the required hyperbolic excess velocity from the delta V required for DSMs, the departure leg V_∞ parameter in the variable vector becomes a convenient and immediate indication of the required launch energy C_3. The C_3 parameter was also mentioned in Section 3.1, where it was explained that it is assumed that the launch vehicle will provide the required energy to achieve the initial interplanetary transfer orbit velocity. The required launch energy and hyperbolic excess velocity are in direct relationship with the amount of spacecraft mass that can be deployed in an interplanetary trajectory. It is therefor used as a trajectory fitness parameters with designation DV. For convenience and clarity the relation between DV, the hyperbolic excess velocity, and the launch energy C_3 is shown here in Equation 4.33.

$$DV = \sqrt{C_3} = V_\infty \tag{4.33}$$

In order to make a judgment on the required on-board propellant of the spacecraft, the summation of the delta V for the DSM maneuvers is separated from the total delta V, and indicated with the designation DSMDV. DSMDV is calculated as shown in Equation 4.34. The parameter ΔV_{dsm_r} is separated here to emphasize that it is a value assigned directly by the variable vector, and not a value defined by the velocity inequality between the first and second part of an interplanetary trajectory leg, a concept explained in Section 4.4.2.

$$DSMDV = \sum_{j=1}^{i} |\Delta V_{dsm_i}| + |\Delta V_{dsm_r}| \tag{4.34}$$

4.5.2. Time To Arrival

The Time To Arrival parameter indicates the time between departure from Earth and entry of the Kuiper Belt region by the spacecraft. This time to arrival is denoted in trajectory results with the designation TTA. The TTA parameter is the summation of the Time-of-Flight (TOF) of each interplanetary leg and of the time between the final planetary swing-by and reaching the inner boundary of the Kuiper Belt. In order to create a clearer distinction between reaching the orbit of Neptune and reaching the Kuiper Belt, the inner boundary of the Kuiper Belt for this calculation is set at 30.5 AU from the Sun. As the aphelion of Neptune's orbit is approximately 30.33 AU this prevents conflicts between a possible Neptune flyby calculation in the trajectory model and with determining the time to arrive at the Kuiper Belt.

The time of flight up to the final planetary flyby is calculated using Equation 4.35, in which a summation is performed of the transfer times of each interplanetary transfer leg. The remaining flight time to the Kuiper Belt is calculated in the reach leg and is dependent on the orbital parameters of the trajectory after the final planetary flyby. To calculate the time between the final flyby and entry of the Kuiper Belt a calculation scheme was set up which will be explained subsequently.

$$TOF_{pl_f} = \sum_{j=1}^{i} t_j \tag{4.35}$$

The calculation scheme solves the following problem: given a body's arbitrary orbital state vector in Keplerian elements S, determine if the body will reach the target distance r_{tar}, and if it does what is the time it takes to travel from the current orbit position to that target distance. In this thesis the problem is always based in the heliocentric frame, meaning that the central body of the orbit is always the Sun. The orbital state vector is always retrieved from the reach leg at the moment right after the final trajectory DSM is applied. However, the calculation scheme can be applied to any problem for which the gravitational parameter μ of the central body is known.

For similar reasons as for the Kepler propagator discussed in Section 4.3.1, the used formulas differ slightly for elliptic and hyperbolic orbits and the calculation for parabolic orbits is not supported. All formulas in this method are taken from Chapters 6 and 8 of Wakker [43].

The formulas in this section are shown using the initial elliptical orbit mean anomaly M_i parameter, for the hyperbolic orbit the formulas are identical but with the initial hyperbolic mean anomaly $\overline{M_i}$ instead. The method to calculate the mean anomaly for both orbit cases is explained in Section 4.3.1 and will thus not be repeated here.

The initial procedure is to determine whether the orbit described by the state vector S will reach the target distance in the first place. For hyperbolic orbits the radial target distance will always be reached at some point as the body coasts to theoretical infinity. For elliptical orbits the apoapsis distance is calculated and used. If the apoapsis of the orbit lies beyond the target distance the body will pass the target distance twice per orbital period. In this case the instance of interest is the passage in which the body is moving away from the central body and reaching r_{tar} for the first time.

The first steps are to calculate the mean motion of the orbit by using Equation 4.36 and to calculate the true anomaly of the target position as shown in Equation 4.37.

$$n = \sqrt{\frac{\mu}{a^3}} \tag{4.36}$$

$$\theta_{target} = \arccos\left(\frac{a(1-e^2) - r_{target}}{e r_{target}}\right) \tag{4.37}$$

The initial true anomaly θ_i and the target true anomaly θ_{target} are then each transformed to their mean anomaly counterparts M_i and M_{target}. The equations used for this transformation are described in Section 4.3.1 and are thus omitted here. Once the mean anomaly parameters are calculated the time of flight between the initial position and the target position can be calculated with the equation shown in Equation 4.38.

$$t_{target} = \frac{M_{target} - M_i}{n} \tag{4.38}$$

Finally, the total flight time between Earth departure and passage of the target distance is calculated as shown here in Equation 4.39. In this equation a summation is performed of the transfer times of the interplanetary transfer legs to the swing-by planets, the fraction of five Julian years for the reach leg DSM application, and the remaining flight time to reach the target distance.

$$TTA = \sum_{j=1}^{i} t_j + \eta_r \cdot 5 \cdot 365.25 + t_{target} \tag{4.39}$$

4.5.3. Time in Kuiper Belt

The time that a spacecraft spends in the Kuiper Belt is represented by the TKB parameter. The method in which the TKB value is calculated is shown in this section. The time spent in the Kuiper Belt is defined as the flight time between 30.5 and 50 AU radial distance from the Sun. The TKB scheme calculates this time from the first passage of the spacecraft through the region, which means that for an elliptical orbit with aphelion beyond 50 AU only the first passage through the Kuiper Belt will be included in the TKB value. The return passage is excluded from the TKB parameter. For an elliptical orbit with aphelion inside the Kuiper Belt the complete flight through the region is used. Excluding the return passage in the first scenario is done as a satellite stays in the neighborhood of its apogee for a relatively long period of time. For example, a satellite orbiting Earth with an apogee altitude of 200,000 km, spends half of its orbital period between a true anomaly of 170.5 and 189.5 degrees. By excluding the return passage from the TKB calculation, trajectories which spend a significant time beyond the Kuiper Belt before returning are discouraged. The TKB calculation uses the same set of equations as the TTA calculation discussed in Section 4.5.2.

For the hyperbolic orbit case, the TKB is determined by performing Equation 4.38 twice with two different values for the target hyperbolic mean anomaly. First the flight time to the inner Kuiper Belt boundary is calculated, which is then subtracted from the flight time to the outer boundary. This is mathematically represented in Equation 4.40. The hyperbolic mean anomalies for the inner and outer Kuiper Belt boundary are reflected by $\overline{M}_{inner}$ and $\overline{M}_{outer}$ respectively.

$$TKB_{hyperbolic} = \frac{\overline{M}_{outer} - \overline{M}_i}{n} - \frac{\overline{M}_{inner} - \overline{M}_i}{n} = \frac{\overline{M}_{outer} - \overline{M}_{inner}}{n} \tag{4.40}$$

For the elliptic orbit case it must first be determined if the Kuiper Belt is reached at all. This is done in the same way as it was for the TTA parameter: by calculating the aphelion value. If the aphelion of the specified orbit is found to lie beyond the outer boundary of 50 AU, the TKB is calculated as in Equation 4.40 but with non-hyperbolic mean anomaly values. If the aphelion lies inside the Kuiper Belt the time of flight to aphelion is calculated instead. The time of flight to the inner boundary is then subtracted, at which point the resulting value is doubled in order to account for the return passage. Note that the mean anomaly at aphelion is equal to π by definition, thereby simplifying the calculation. The procedure to calculate TKB for an orbit with aphelion in the Kuiper Belt is reflected by Equation 4.41.

$$TKB_{elliptic} = 2\left(\frac{\pi - M_{inner}}{n}\right) \tag{4.41}$$

It should be noted that some edge cases exist in the calculation of TKB depending on the trajectory. For example: trajectories that perform a flyby of planet Neptune are likely to perform their DSM inside the Kuiper Belt, thereby altering the orbit while passing through the Kuiper Belt. The calculation procedure described in this section does not account for this scenario. Special algorithms are therefor included in the calculation scheme to accommodate for these exceptional cases. For the mentioned scenario this includes using the orbit state vector before DSM application to determine the period between the Neptune flyby and the DSM that is spent in the Kuiper Belt. This period is then added to the time that the spacecraft spends in the Kuiper Belt after DSM application with the post-DSM orbit elements.

4.6. Verification

This section discusses the steps taken to verify the trajectory model discussed in Section 4.4 and the calculation of the trajectory fitness values described in Section 4.5. Verification of the model is described first in Section 4.6.1. Verification of the fitness value calculations is discussed in Section 4.6.2.

4.6.1. Trajectory Model Verification

The Tudat trajectory model is very similar to the trajectory model used for the ESA Global Trajectory Optimization Problems (GTOP) database project. The C++ code for this model is freely available from the ESA GTOP website: *esa.int/gsp/ACT/projects/gtop* [53]. Translation of this model into the modular design of the existing Tudat libraries was a significant aspect of the thesis written by Musegaas [44]. Musegaas put significant efforts in the development, testing, and verification of the Tudat MGA-1DSM trajectory model and the reader is therefor referred to this thesis for much more details on these topics. For more information on the GTOP project and its contributions to the field of high-thrust trajectory optimization the reader is referred to the technical report by Vinko and Izzo and a conference paper by Vinko et al. [51][54].

In this thesis, verification of the model itself will be limited to ensure that the tests that were specifically built to verify the model are complete, performed, and that they return the expected results. For the Tudat MGA-1DSM-VF trajectory model a total of seven unit tests are distributed at time of writing. Some of these unit tests calculate various trajectories or parts of trajectories and compare the results with the results produced by the ESA GTOP model. Other tests check the inner workings of the model in regards to updating ephemeris or variable vector parameters. The tested full trajectory problems are known under the names Messenger-easy and Cassini-2. For both of these problems several variable vectors and their corresponding solution are listed on the GTOP website. The Tudat model is verified by inserting the values of these variable vectors into the Tudat trajectory model and comparing the calculated delta V with the results published by ESA. Special care is taken to include all aspects of the trajectory model by including both full trajectory calculations as well as specific components of the model, such as the unpowered gravity assist propagator, the Lambert targeter, and the Kepler propagator. The test results of the full trajectories and the unpowered gravity assist propagator are shown in Table 4.1. For these tests a seemingly high error tolerance is allowed by the Tudat unit tests. This is because the default ephemeris model used by Tudat differs from the one used by the GTOP model, a deviation also documented by Musegaas in his thesis. In his test documentation Musegaas notes that the implemented Lambert targeter is highly sensitive to small variations in the z-position of a planet and that this is the main reason that variations are present between the Tudat model and the GTOP model results. Musegaas performed additional verification tests with implementation of the GTOP ephemeris model which returned satisfactory results [44].

Test	GTOP result [m/s]	Tudat result [m/s]	Relative error [-]	Allowed error [-]
Messenger-easy	8644.631811	8630.832561	$1.6 \cdot 10^{-3}$	$2.0 \cdot 10^{-3}$
Casssini-2	8385.157845	8656.658720	$3.2 \cdot 10^{-2}$	$4.0 \cdot 10^{-2}$
Unpowered GA	1415.440206	1415.440408	$1.4 \cdot 10^{-7}$	$1.0 \cdot 10^{-6}$

Table 4.1: Results for two GTOP MGA-1DSM full trajectory model tests and for the unpowered gravity assists unit test distributed with Tudat. The ephemeris model described by Standish [52] instead of the GTOP model was used in these tests. Solution listed by GTOP are used as reference data [51].

The test of the Lambert targeter and Kepler propagator return large arrays of test data and will therefor not be listed in this document. The Kepler propagator is tested by propagating various orbits for a certain time with a certain time-step. The results are then compared to data from external verified sources. The Lambert targeter is tested by comparing the computed semi-major axis, departure and arrival velocity vector components, and transfer rotation direction for various input parameters to the results documented in external publications. With all relevant tests analyzed, completed, and passed, the trajectory model is deemed sufficiently verified.

4.6.2. Fitness Value Verification

The DV and DSMDV parameter calculations were verified by the trajectory model verification in Section 4.6.1. This section will thus focus on the TTA and TKB fitness parameter calculation. The method to verify these two parameters is effectively identical. As Tudat contains a verified Kepler propagator it is possible to propagate an arbitrary orbit by its TTA and TKB time. The propagated orbit parameters can then be analyzed to verify the results. An orbit propagated by the calculated TTA value should thus result in an orbit parameter vector describing a position with a radial distance of 30.5 AU from the Sun. In case the input orbit never reaches, or already passed, the inner Kuiper Belt boundary an indication of this fact is returned instead. To make sure that these exceptions are valid, the aphelion and initial radial distance of every input orbit is calculated separately and compared. An additional check is performed to confirm that the travel direction of the propagated orbit at 30.5 AU is away from the Sun, and not towards it. This test was performed with five runs of 100,000 differently seeded pseudo-randomly generated input orbit parameter vectors. The standard C++ pseudo-random number generator *std::rand* was used to supply the random numbers. The mean absolute and mean relative error of each test run is shown in Table 4.2. It is concluded from the values in this table that the difference between the result produced by the Kepler propagator and the calculated result is negligible.

Run	Seed	Absolute error [m]	Relative error [-]
1	111	$1.6\cdot10^{-4}$	$3.5\cdot10^{-17}$
2	222	$1.6\cdot10^{-4}$	$3.5\cdot10^{-17}$
3	333	$2.5\cdot10^{-4}$	$5.5\cdot10^{-17}$
4	444	$2.3\cdot10^{-4}$	$5.0\cdot10^{-17}$
5	555	$1.9\cdot10^{-4}$	$4.2\cdot10^{-17}$

Table 4.2: Verification test results for the calculation of the TTA parameter. Each run consisted of 100,000 randomly generated orbit parameter vectors.

For propagation for the TKB parameter the same test was performed as for the TTA parameter, but with a slight adjustment. Propagation of an orbit for the duration calculated for TKB can result in a radial distance of either 30.5 or 50 AU. 30.5 AU for elliptical orbits with the aphelion inside the Kuiper Belt, and 50 AU for hyperbolic orbits and elliptical orbits with aphelion beyond 50 AU. The test was thus adjusted slightly to verify these scenarios correctly. Furthermore it should be noted that initial random orbit parameter vectors are propagated for a duration of the sum of TTA and TKB. The resulting errors in this case are thus the error of both the TTA and the TKB calculation scheme together. The mean absolute and mean relative error of each test run is shown in Table 4.2. Again it is concluded that the differences in expected result and calculated result are negligible based on these tests.

Run	Seed	Absolute error [m]	Relative error [-]
1	111	$1.6\cdot10^{-4}$	$2.1\cdot10^{-17}$
2	222	$1.6\cdot10^{-4}$	$2.1\cdot10^{-17}$
3	333	$3.1\cdot10^{-4}$	$4.2\cdot10^{-17}$
4	444	$2.8\cdot10^{-4}$	$3.7\cdot10^{-17}$
5	555	$1.6\cdot10^{-4}$	$2.2\cdot10^{-17}$

Table 4.3: Verification test results for the calculation of both the TTA and the TKB parameter. Each run consisted of 100,000 randomly generated orbit parameter vectors.

5

Trajectory Optimization Options

In Chapter 4 it was described how the trajectory model works and what parameters are required to specify the calculation of a trajectory. This chapter focuses on the software and options which should be considered to maximize the likelihood of finding the optimal solutions to the Kuiper Belt trajectory problem. An introduction to the PaGMO scientific library and the benchmark problem is given in Section 5.1. The tuning parameters for the used optimization algorithm are then discussed in Section 5.2. To further guide the algorithm and increase the likelihood of finding global minimum solutions in the problem search space, penalties and boundary conditions are applied to solutions. These are discussed in Section 5.3. Finally Section 5.4 discusses the method in which the optimization options are tested with the benchmark problem in order to find the optimum optimization algorithm and problem definition settings for the Kuiper Belt trajectory problem.

5.1. Software and Benchmarking

This section discusses the software package PaGMO that is used to optimize the trajectory problems, as well as the suitable algorithms within this software. An introduction to the PaGMO optimization toolbox is given in Section 5.1.1. Then consideration of the optimization algorithms within PaGMO that are suitable for use with the Kuiper Belt trajectory problem are discussed in Section 5.1.2. Then a short description of the two benchmark problems on which the problem implementation and the algorithm performance will be tested is given in Section 5.1.3.

5.1.1. PaGMO Optimization Toolbox

Parallel Global Multi-objective Optimizer (PaGMO) is a scientific library initially developed by members of the Advanced Concepts Team (ACT) of ESA. It offers multiple global and local optimization algorithms initially gathered in a toolbox to solve optimization problems regarding interplanetary trajectory design projects within ESA. The use cases for PaGMO have expanded over the years as the optimization libraries finds their use in other fields of research as well. PaGMO features a framework and a wide array of algorithms that can be used for single-objective, multiple-objectives, continuous, integer, box-constrained, non-linear constrained, stochastic, and deterministic optimization problems. The toolbox allows the user to define a problem and then easily implement an appropriate algorithm to attempt to find an optimized solution for that problem [55].

Figure 5.1: Schematic representation of a typical PaGMO problem definition structure.

The general method in which PaGMO is set up is shown in Figure 5.1. First, the user defines the dimension and bounds of the decision variable vector. Then the problem computation scheme and the problem objective functions are specified. At this point the user can initialize a population of decision vectors. PaGMO generates this population automatically if the user specifies a population size. The user also specifies the number of generations that the optimization scheme should iterate the algorithm on the population. Special tuning parameters can be supplied to the algorithm as well. These tuning parameters further specify the behavior of the algorithm during the optimization process. Then the algorithm is linked to the initial population at which point the iterating optimization loop can be initiated. In an attempt to increase efficiency and level of success of the optimization process, further steps can be taken to solve multiple populations simultaneously on what are called islands. These islands can even be initiated with different algorithms or differently tuned algorithms. The best performing individuals can subsequently be migrated between islands in an archipelago structure. This type of structure is often implemented with the use of multiple processing cores or with a network of computers in which each node solves an individual island. In this thesis the archipelago structure is not used [56].

The PaGMO library includes a wide variety of algorithms. Broadly speaking these algorithms each aim to solve specific types of problems. A good initial basic classification is the ability of the algorithm to perform a global optimization or a local optimization. Global optimization is distinguished from local optimization by its focus to finding the minimum solution over the entire search space, as opposed to finding the local minimum solution. The difference between these is illustrated in Figure 5.2. Finding the global minimum is typically far more difficult than finding a local minimum solution. Some studies utilize a global optimizer first to map the problem search space. Subsequently a local optimization algorithm is used to investigate promising areas of the problem or to fine tune the global solutions.

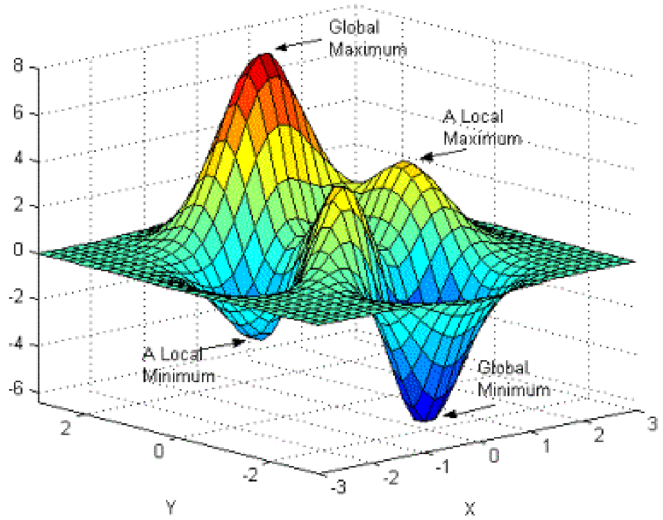

Figure 5.2: An example of an objective function with global and local optima indicated. A global optimization algorithm will always aim the find the global optimum. A local optimization algorithm will more likely iterate within a local optimum of a problem.

The documentation of PaGMO flags each algorithm with the types of problem an algorithm can solve; these flags include single-objective and multi-objective, constrained and unconstrained, integer-programming, and stochastic. An unconstrained problem contains no limitations on the values of the variables other than that they find the optimal solution. For some problems there are constraints to the variables which make otherwise valid solutions illegal. An integer problem is an optimization problem in which some or all of the variables are restricted to be strictly whole integers. Stochastic problems are partially uncertain. Some of the data incorporated in the objective or constraints are undetermined but are usually characterized by a probability distribution. For the interplanetary trajectory problem in this thesis a global multi-objective continuous problem optimization algorithm is required. The suitable algorithms for this type of problem that are available in PaGMO will be discussed in Section 5.1.2 [57].

5.1.2. Multi-objective Optimization

An algorithm's single- or multi-objective specification determines whether the algorithm is capable of finding solutions for a problem in which multiple objectives conflict and typically no single optimal solution is present. This is the case for the problem of this study in which for example the ΔV budget typically conflicts with the spacecraft flight time. With a multi-objective problem, an optimization process will ultimately return solutions in the form of a Pareto front in which no single solution is necessarily better than the other. Once the solution space has sufficiently converged no further improvement can be achieved in any objective without degrading the fitness of other objectives. In a two-objective problem such solutions are then often placed in a Pareto front in order to determine the behavior of the problem and to identify the most suitable solutions. An example of well and badly optimized result for a two-dimensional and a three-dimensional problem is shown in Figure 5.3.

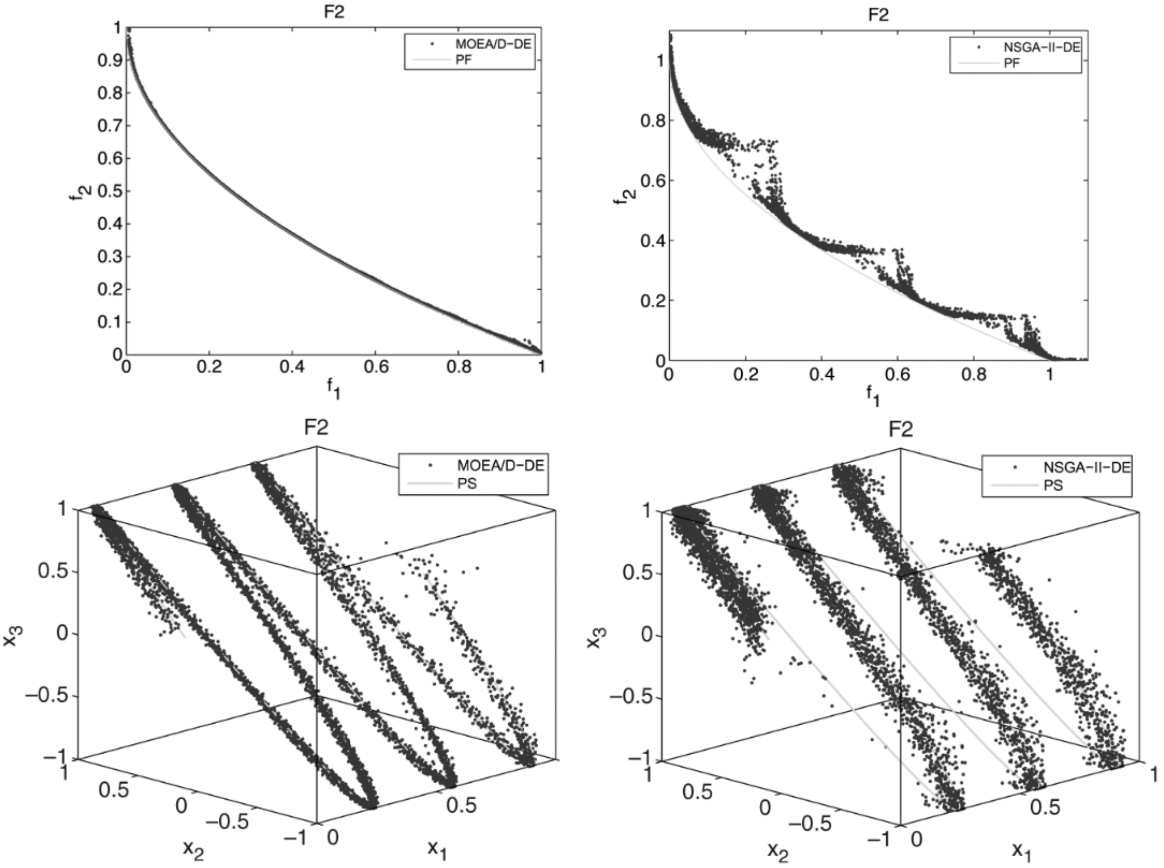

Figure 5.3: Top row: an example of a well optimized result (left) and a badly optimized result (right) of a two-objective problem with corresponding true Pareto fronts indicated. Bottom row: an example of a well optimized result (left) and a badly optimized result (right) of a three-objective problem with corresponding true Pareto sets indicated [58].

Mathematically a multi-objective optimization problem can be stated as follows:

$$\begin{aligned} &minimize \;\; F(x) = (f_1(x), \ldots\ldots, f_m(x))^T \\ &subject\ to\ x \in \Omega \end{aligned}$$

where Ω is the decision variable space, $F : \Omega \rightarrow R^m$ consists of m objective functions and R^m is the objective space. The possible objective set is then defined as the set $\{F(x) | x \in \Omega\}$. As stated before, it is very well possible that no value in Ω exists that maximizes all objectives simultaneously. Instead the objective values are to be balanced with the best trade-offs being defined in terms of Pareto optimality. The set of Ω values that define a Pareto optimality is called a Pareto set, or Pareto optimal vector. The set of all Pareto optimal vectors is the Pareto front.

Often multi-objective problems have many, or even infinite number of Pareto optimal vectors. It is therefor very time consuming, or impossible, to obtain the complete Pareto front of a problem. Many multi-objective optimization algorithms are thus used to find a manageable number of Pareto optimal solutions that are aimed to be evenly distributed along the Pareto front. This distribution of optimal solutions is then utilized as a good approximation of the true Pareto front. The approximation of the Pareto front is finally used by the decision maker to select a final preferred solution [59]. The role of the decision maker and the method in which the true Pareto front is approximated in this thesis will be further discussed in Section 5.4.3. In this section the focus will be on PaGMO and the multi-objective algorithms themselves.

At time of writing PaGMO (version 2.11.3) is distributed with two optimization algorithms capable of solving purely multi-objective problems: *Non-dominated Sorting Genetic Algorithm* (NSGA-II), and *Multi-objective Evolutionary Algorithm by Decomposition* (MOEA/D-DE). Each of these will be discussed briefly below.

Non-dominated Sorting Genetic Algorithm (NSGA-II)
NSGA-II is an evolutionary genetic algorithm widely used for many real-world applications. Today it is regarded as an outdated approach but it still offers great value as a solid benchmark algorithm. NSGA-II generates an initial population of solutions and then an offspring population by using selection, mutation, and recombination methods on the original population. These two populations are combined at which point solutions are sorted into different groups based on their performance. Similarity between the groups is evaluated on the Pareto front and similarity measures are used to ensure that a diverse range of solutions is maintained. This similarity is calculated by computing the density of solutions in a neighborhood of the Pareto front. The worst performing half of the ranked population is eliminated and the process is repeated [60].

Multi-objective Evolutionary Algorithm by Decomposition (MOEA/D-DE)
MOEA/D is a very successful algorithm based on the idea of problem decomposition, meaning that it decomposes a multi-objective problem into individual optimization sub-problems and optimizes them separately but simultaneously. Each sub-problem is optimized by using information from neighboring problem solutions. Similar to NSGA-II it uses mutation to modify offspring solutions as well as diversity preservation mechanisms to ensure a diverse solutions range. The version implemented in PaGMO is based on the popular Differential Evolution (DE) system. While many variations of DE exist, the basic principle revolves around generating a mutant solution vector by taking the weighted difference between two randomly chosen individuals from the population. This mutant vector is then added to a third individual. If the resulting fitness is better than the original third individual it is replaces this third individual [58][59].

In the work by Zhang and Li in [58] and [59] the MOEA/D algorithm performs significantly better than the NSGA-II algorithm on a wide variety of multi-objective integer knapsack problems as well as on continuous multi-objective optimization problems. An example of the comparison between the NSGA-II and MOEA/D results on two of these problems was shown in Figure 5.3. Furthermore it is noted that the computational complexity of the MOEA/D is lower when compared to that of the NSGA-II algorithm. Finally, the Binomial Intersection (BI) problem decomposition method featured in MOEA/D is noted to be highly effective in producing uniform distributions of the Pareto front approximation in problems with more than two objectives. Based on these reasons, as well as the result of preliminary tests done by the author on the Cassini-2 problem discussed in Section 5.1.3, it is decided to utilize the MOEA/D algorithm in the optimization problems of this thesis. The mechanics and options of the PaGMO implementation of the MOEA/D algorithm are further discussed in Section 5.2.

5.1.3. Benchmark Problems

To test the implementation and the optimization algorithm performance two benchmark problems will be used. The first problem, called Cassini-2 or Cassini2 Full Difficulty, is a problem in the ESA GTOP database mentioned in Section 4.6.1. The Cassini-2 problem was also used to verify the trajectory model results. The Cassini-2 problem is quite complex, featuring four swing-by legs in the order of Venus, Venus, Earth, Jupiter, and a capture leg around planet Saturn. As the GTOP version does not have the option to include a reach leg, the problem is adapted so that instead of a capture leg around Saturn, the benchmark implementation features a reach leg culminating in a crossing of the Kuiper Belt boundary at 30.5 AU. This adaption increases the number of problem variables from 22 to 26. The list of decision variables and their bounds are listed in Table 5.1. The information in this table provides a adequate indication of the quantity of problem variables and their range of values for a typical optimization problem. The bounds of this problem are taken from the GTOP Cassini-2 problem. For reference and as an example of an optimized variable vector, the table also lists the best putative solution for the default Cassini-2 problem as listed on the GTOP website.

Leg type	Decision Vector Entry	Variable	Lower Bound	Upper Bound	Best Putative GTOP Solution	Units
Departure	x(1)	t_0	-1000	0	-779.04675	MJD2000
Departure	x(2)	T_1	100	400	167.37895	days
Swingby	x(3)	T_2	100	500	424.02825	days
Swingby	x(4)	T_3	30	300	53.28974	days
Swingby	x(5)	T_4	400	1600	589.76695	days
Swingby	x(6)	T_5	800	2200	2200	days
Departure Earth	x(7)	η_1	0.01	0.9	0.76948	-
	x(8)	V_∞	3000	5000	3259.11446	m/s
	x(9)	θ	0	2π	3.30481	rad
	x(10)	ϕ	$-\pi/2$	$\pi/2$	0.24058	rad
Swingby Venus	x(11)	η_2	0.01	0.9	0.51329	-
	x(12)	b_{rot_1}	$-\pi$	π	-1.59374	rad
	x(13)	r_{p_1}	1.05	6	1.34878	R_{pl}
Swingby Venus	x(14)	η_3	0.01	0.9	0.02742	-
	x(15)	b_{rot_2}	$-\pi$	π	-1.95956	rad
	x(16)	r_{p_2}	1.05	6	1.05	R_{pl}
Swingby Earth	x(17)	η_4	0.01	0.9	0.26399	-
	x(18)	b_{rot_3}	$-\pi$	π	-1.55499	rad
	x(19)	r_{p_3}	1.15	6.5	1.30730	R_{pl}
Swingby Jupiter	x(20)	η_5	0.01	0.9	0.59998	-
	x(21)	b_{rot_4}	$-\pi$	π	-1.51346	rad
	x(22)	r_{p_4}	1.7	291	69.80901	R_{pl}
Reach Saturn	x(23)	η_6	0.01	5.0	-	years
	x(24)	b_{rot_5}	$-\pi$	π	-	rad
	x(25)	r_{p_5}	1.7	100	-	R_{pl}
	x(26)	ΔV_{dsm_r}	-100	100	-	m/s

Table 5.1: The decision vector variables and bounds for the Cassini-2 benchmark problem. The putative best solution registered by GTOP for the default GTOP capture leg problem is also shown [53].

The second problem is based on the planetary sequence of the envisioned NASA Trident mission. This problem is selected based on the quantity of flybys and the fact that it ends in a Neptune gravity assist. The proximity of Neptune to the Kuiper Belt is likely to cause interesting solutions, but is also a unique situation within the problem definition. A trajectory with a flyby of Neptune should therefor be evaluated in a preliminary testing phase. The Trident mission makes use of six gravity assists in the sequence of Earth, Venus, Earth, Earth, Jupiter, Neptune. With implementation of the reach leg at Neptune this results in a total of 30 variables in the decision vector, four more than the most complex problem in the GTOP database: Messenger-Full. For reference and as an example of a trajectory optimization problem in this thesis, the Trident problem variables and bounds are listed in Table 5.2. As the Trident problem is not part of GTOP, the variable bounds were initially based on the limited information of the proposed Trident trajectory discussed in Section 2.3, taken from Mitchell et al. [23]. However, this trajectory is purely indented to achieve a short time of flight to Neptune and therefor inevitably reaches the Kuiper Belt with a very high excess velocity. In order to evaluate more diverse problem solutions the maximum time of flight, for particularly the trajectory legs featuring planets Jupiter or Neptune, were increased significantly.

Leg type	Decision Vector Entry	Variable	Lower Bound	Upper Bound	Trident Proposal	Units
Departure	x(1)	t_0	9131	14610	9601	MJD2000
Departure	x(2)	T_1	100	400	196	days
Swingby	x(3)	T_2	100	500	148	days
Swingby	x(4)	T_3	30	400	319	days
Swingby	x(5)	T_4	400	1600	1096	days
Swingby	x(6)	T_5	500	2200	507	days
Swingby	x(7)	T_6	1200	5500	2191	days
Departure Earth	x(8)	η_1	0.01	0.9	-	-
	x(9)	V_∞	3000	6000	5075	m/s
	x(10)	θ	0	2π	-	rad
	x(11)	ϕ	$-\pi/2$	$\pi/2$	-	rad
Swingby Earth	x(12)	η_2	0.01	0.9	-	-
	x(13)	b_{rot_1}	$-\pi$	π	-	rad
	x(14)	r_{p_1}	1.15	6.5	-	R_{pl}
Swingby Venus	x(15)	η_3	0.01	0.9	-	-
	x(16)	b_{rot_2}	$-\pi$	π	-	rad
	x(17)	r_{p_2}	1.05	6	-	R_{pl}
Swingby Venus	x(18)	η_4	0.01	0.9	-	-
	x(19)	b_{rot_3}	$-\pi$	π	-	rad
	x(20)	r_{p_3}	1.05	6	-	R_{pl}
Swingby Earth	x(21)	η_5	0.01	0.9	-	-
	x(22)	b_{rot_4}	$-\pi$	π	-	rad
	x(23)	r_{p_4}	1.15	6.5	-	R_{pl}
Swingby Jupiter	x(24)	η_6	0.01	0.9	-	-
	x(25)	b_{rot_5}	$-\pi$	π	-	rad
	x(26)	r_{p_5}	1.7	291	2.24	R_{pl}
Reach Neptune	x(27)	η_7	0.01	5.0	-	years
	x(28)	b_{rot_6}	$-\pi$	π	-	rad
	x(29)	r_{p_6}	1.7	100	-	R_{pl}
	x(30)	ΔV_{dsm_r}	-100	100	-	m/s

Table 5.2: The decision vector variables and bounds for the Trident benchmark problem. The Trident proposal data is taken from the very limited trajectory information in Mitchell et al.[23].

5.2. Algorithm Tuning

Tuning of the algorithm parameters has a very significant effect on the quality of the optimization process results. This section describes the necessity and the goal of the algorithm tuning process in Section 5.2.1. The tuning parameters and options of the selected MOEA/D optimization algorithm are described in Section 5.2.2.

5.2.1. Effect and Goal of Algorithm Tuning

The value and effect of tuning optimization algorithms for interplanetary trajectory problems is a topic that has been extensively studied by many, including for example Musegaas in [44]. Tuning of an algorithm is done by specifying and adjusting internal parameter values of the algorithm calculation scheme. The specific parameters vary from algorithm to algorithm. The tuning parameters that exist within MOEA/D are discussed in detail in Section 5.2.2. The goal of the tuning procedure is to increase the reliability that an algorithm finds qualitatively well optimized results regardless of the initially generated population and the problem specifics.

Due to various reasons it is typically very difficult to compare different optimization techniques with each other. Studies may employ different testing problems, performance criteria, trajectory models, and ephemeris data. These differences prevent the interchangeability of the tuning parameters for different studies. This difficulty increases even further when the number of objective functions is larger than one and features a novel objective such as TKB. To tune the MOEA/D algorithm for the problems in this thesis, a new tuning process needs to be performed. This tuning process will be performed on the Cassini-2 benchmark problem. This problem is used because it is well understood, sufficiently complex, and part of the standard GTOP problems.

As stated, optimization algorithms need to be tuned in order to improve their ability to find optimal solutions. The process of tuning various single-objective PaGMO algorithms and the tuning effectiveness was described by Musegaas. The single-objective optimization algorithms in this thesis were used to find minimum Delta V trajectory solutions to planet Saturn. Musegaas describes how the tuning of optimization algorithms has a very strong effect on their performance and that the tuning parameters can be very sensitive. An example of this can be found in a paper by Olds et al. where the sensitivity of the DE algorithm is clearly shown. The study tested a large number of different settings and applied the algorithm to four different trajectory problems. The time to find a solution with 95% reliability was calculated and used as a performance indicator. Some of the results for the Cassini-2 mission trajectory case can be seen in Table 5.3. The data in this table show that the performance of the DE algorithm is highly dependent on the tuning parameters F, n_p and CR, indicating the scale factor, population size, and cross-over rate respectively. With some combination of settings the algorithm is able to find the solution within two minutes, while with others it will take several hours or it is not able to find a reliable solution at all. The data also show that the tuning parameters are highly sensitive. An increase of 0.2 in CR, for example, can make the difference in a solution within four minutes or no solution at all. Additionally, the data show that the parameters are co-dependent and can thus not be tuned efficiently one by one [61].

F	n_p = 20			n_p = 36		
	CR = 0.4	CR = 0.6	CR = 0.8	CR = 0.4	CR = 0.6	CR = 0.8
0.2	23.2	no sol.	no sol.	14.3	354.1	49.9
0.4	3.7	3.3	no sol.	13.1	5.4	1.8
0.6	19.1	2.8	1.4	195.5	9.1	1.8
0.8	160.2	3.0	1.4	no sol.	206.8	3.0
1.0	267.3	109.6	no sol.	no sol.	631.5	24.2
rand[-1,1]	4.9	2.4	1.4	9.3	2.1	1.3

Table 5.3: Run time in minutes required to reliably optimize a single-objective Cassini problem with a single DSM, using various turning parameters of the DE algorithm [61].

The importance of tuning is also reflected by the density of the dots in Figure 5.4. This image created by Musegaas with data from Price et al. in [62] shows the performance of the DE algorithm in three different problems. From the location of the swarm of dots it can be seen that the optimal region of the CR and F values differs greatly from problem to problem.

The successful tuning process described by Musegaas in [44] is applied to three single-objective algorithms. For the DE algorithm, which is the algorithm at the base of MOEA/D, the tuning process is split up into three phases. In the first phase preliminary tests are performed in which badly performing parameter settings are removed in order to limit the number and range of variable settings involved. The second tuning phase then aims to find the parameter values which perform best from the remaining options. The third and final phase is used to adjust the population size until the best performing size is found. The described process works well for multiple problem cases and provides clear parameter value regions in which good performance is returned.

The described processes give an indication of how a tuning process should be approached and that using a structured approach is necessary. The number of parameters and the sensitivity of the algorithm prohibits a successful trial-and-error approach. Therefor this tuning process is mimicked in this thesis. By first pruning badly performing settings from the variable search space, before starting a tuning process in which the best performing parameter values are to be found.

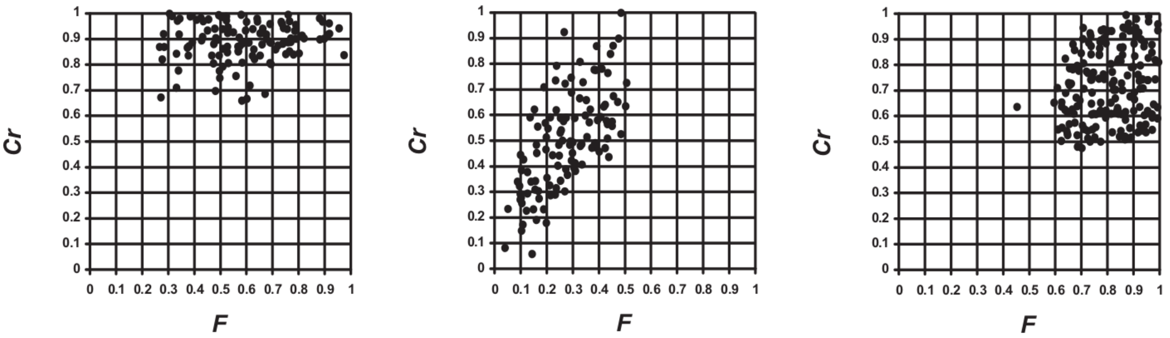

Figure 5.4: Ideal tuning parameters of DE algorithm for the 10D Rotated Whitley, Griewank, and Rosenbrock problems. The density of the dots is a measure of the algorithm performance. [62][44]

5.2.2. Tuning Parameters

To start it should be noted that several strategies exist for the DE algorithm that is used within MOEA/D. The MOEA/D version in PaGMO uses a strategy notated with *DE/rand/2/exp*. In this notation *rand* determines that the mutant vector will be added to a random individual of the population. In another popular strategy, notated with *best*, the mutant vector is instead added to the best performing individual of the population. With a random individual the algorithm has a higher chance of exploring the larger sections of the search space, while using the best performing individual generally causes the algorithm to converge on a single well-performing region. The *2* in *DE/rand/2/exp* signifies the number of difference vectors that are used to create the mutant vector. *Exp* describes the exponential cross-over scheme that is used within the MOEA/D DE algorithm. In this scheme the position at which a candidate vector is sliced is random before it continues to include more parameters until the number of parameters in the mutant vector exceeds the CR value [63].

The CR and other parameters of the PaGMO MOEA/D algorithm that are considered and tested in this thesis are listed in Table 5.4. The weight generation method that is absent from this list of parameters was kept at its default value of *grid*. The alternatives of this parameter: *low discrepancy*, and *random*, generated significantly worse results during preliminary tests on the Cassini-2 problem, and were therefor not further evaluated.

Parameter	Default value	Description
Population size	-	Number of individual solutions in a population
Decomposition method	Tchebycheff	Method by which the objectives are decomposed
Seed	Random	Seed for the internal random number generator
Generations	-	Number of times the algorithm iterates the population
Cross-over rate (CR)	1.0	Crossover parameter of the DE operator
Scale factor (F)	0.5	F parameter of the DE operator
Neighbourhood size (T)	20	Size of the neighbourhood that is considered to generate a new solution
Conservation chance (Realb)	0.9	Chance that the neighbourhood of a solution is considered rather than the whole population

Table 5.4: Short description and the default setting of the evaluated tuning parameters for the MOEA/D algorithm in PaGMO.

Population Size

The population size and the number of generations is kept constant for each problem and optimization run. This is done as these parameters are most resistant to small variations in their value. Furthermore, by setting these parameters as a constant early on, the number of variables that influence the further tuning process is reduced by two. The parameter of population size is set at a constant value of 1,000. This value is chosen to ensure a well-populated Pareto front. Increasing the population size beyond 1,000 decreases computational performance as more solutions need to be evaluated and iterated in a single run. A value of 1,000 is deemed a good compromise between a sub-optimally populated Pareto front, and an overly long computational time.

Decomposition Method

The decomposition method determines the way in which the multiple objectives in the multi-objective problem are separated and ranked. By using these methods the problem of approximating the Pareto front is converted to a number of separate optimization problems. The default method by which this is done is called the *Tchebycheff* approach. Its available alternatives are called *Weighted* and *Boundary Intersection* (BI). For an exact explanation of how these methods work and differ the reader is referred to the work of Zhang and Li [59]. Zhang and Li note that the *Weighted* method is most likely to work well with convex or concave shaped Pareto fronts, which requires a two or three objective problem. The BI method is more likely to produce favorable results for problems with more than two objectives. The focus of a four-objective tuning process should thus be on the Tchebycheff and BI decomposition methods.

Seed
The seed number is used to perform multiple and repeatable optimization runs on the same problem. Each test and run in this thesis is repeated five times using five different seed numbers for the pseudo-random number generator of PaGMO. These seed numbers are always the same: 111, 222, 333 ,444, and 555. These numbers are identical to those used in the verification tests of Section 4.6.2.

Generations
Some studies, especially those that consider single-objective problems, specify a solution convergence tolerance. In this case the optimization is performed until the relative improvement between two generations is smaller than a specified limit. The two selected generations for this scenario can be, but do not have to be, sequential. Often a certain number of generations is set between the two that are compared in order to reduce the risk of confusing a temporary plateau in solution quality with a completely converged solution. In a multi-objective problem the appeal of setting an iteration improvement tolerance is less obvious. In a problem with more than two objectives it is more difficult to objectively compare solutions and to judge whether a population has been sufficiently optimized. With this in mind a two-objective optimization test on the standard GTOP version of the Cassini-2 problem was performed in order to determine a static limit on the number of generations that should be performed. The results of this test is shown in Figure 5.5, with the two objectives shown on the X- and Y-axis. Delta V in this figure is a summation of the DV and DSMDV parameters as defined in Section 4.5. TOF on the x-axis of this figure is the time of flight between spacecraft launch and arrival at the SOI of Saturn. The figure shows that while the solution performance rapidly increases in the initial 1000 generations, further improvement takes place in the remaining 2000 iterations. The 222 seed run finds the same general solution space as the other runs between generations 1800 and 2400, and continues to improve until generation 3,000. At generation 3,000 all five runs finally individually describe an almost identical Pareto front. Based on these results a value of 3,000 generations is set for each problem optimization run.

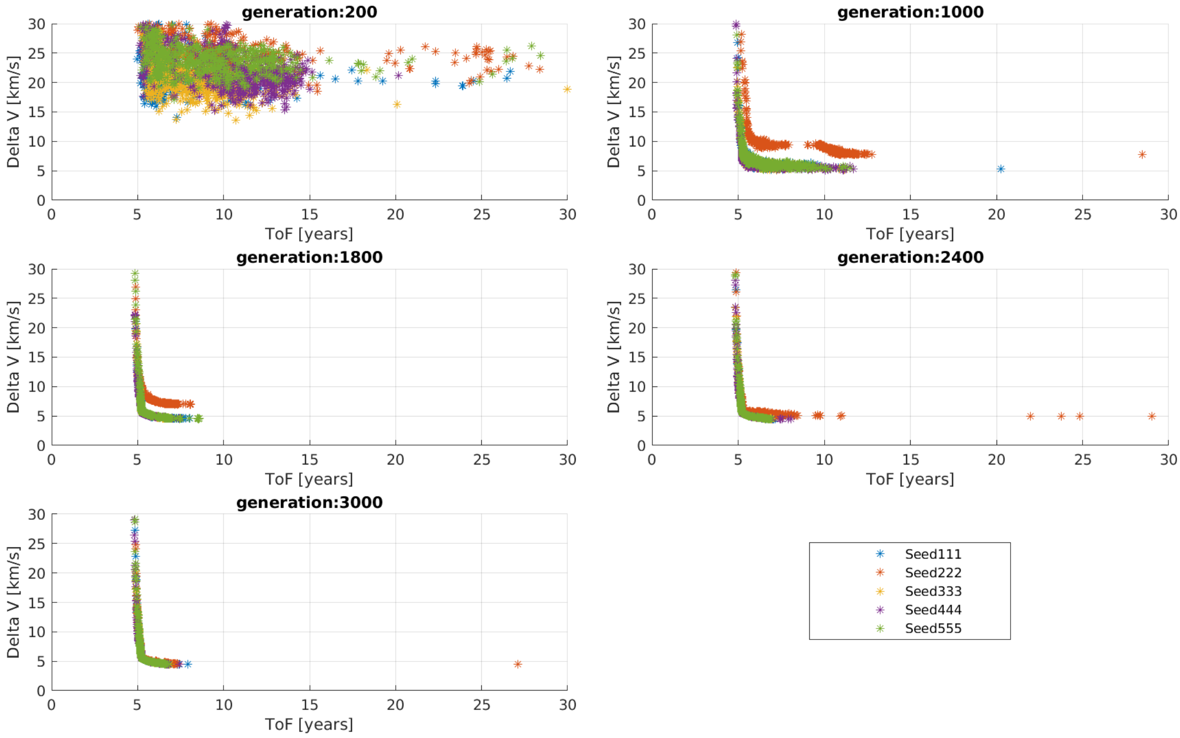

Figure 5.5: Evolution of solutions for a two-objective optimization of the default GTOP version of the Cassini-2 benchmark problem. The optimization is performed five times with default values of the MOEA/D algorithm but with five different seed numbers. The quality of the solutions keep improving between generations 2400 and 3000, most notably in the Seed 222 run.

The parameters CR, F, T, and *Realb* are the main parameters that will be tuned in the four-objective tuning phase described in Chapter 7.

CR and F

The CR and F values are the main parameters that define the behavior of the DE algorithm. As was shortly described in the description of MOEA/D in Section 5.1.2, the DE algorithm broadly revolves around generating a new mutant solution vector by combining and altering the variables of other solution vectors. This new mutant vector is then added to a third solution vector to create the trial vector. The number of variables that exist in the mutant vector is determined randomly with a probability set by the CR value. An illustration of the cross-over process is shown in Figure 5.6. The CR value is limited to the domain [0,1], corresponding to a low probability or high probability to stop the inclusion of new variables into the mutant vector. Once the initial mutant vector has been created it is combined with the weighted difference between two or more other solution vectors from the population. The weight by which this difference is multiplied is set by the scale factor F, which is also bounded to the domain [0,1]. In mathematical terms, the creation of the mutant vector in the *DE/rand/2/exp* strategy can be described as follows:

$$v_{i,G+1} = x_{r_1,G} + F \cdot (x_{r_2,G} + x_{r_3,G} - x_{r_4,G} - x_{r_5,G}) \tag{5.1}$$

with $v_{i,G+1}$ being the mutant vector, $x_{i,G}$ the target vectors, r_i random indexes, F the scaling factor, and $i \in \{1, 2, ..., D\}$ where D is the number of parameters in a target vector. Ultimately the fitness of the trial vector is compared to the fitness of the target vector, and substituted if its performance is superior [63].

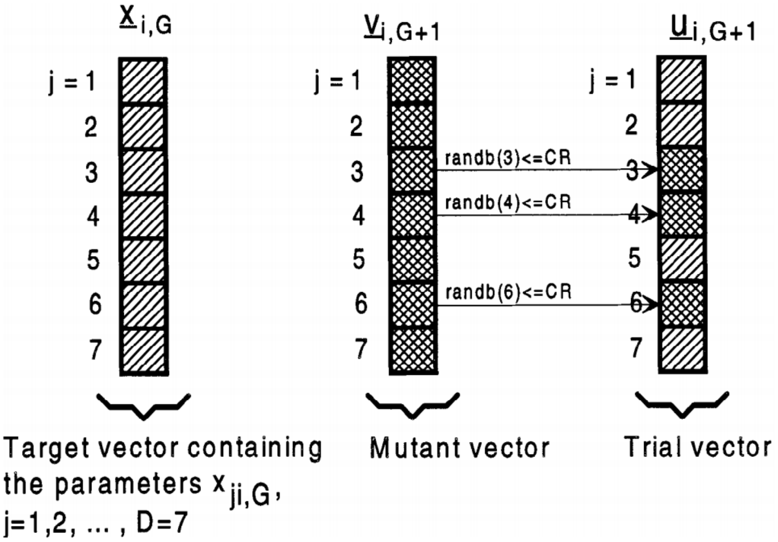

Figure 5.6: Illustration of the DE crossover process for a solution vector of size D = 7 [63].

T and Realb

T is the size of the neighbourhood of sub-solutions that are used for optimizing in MOEA/D. In short, two solutions have a chance to be combined only when they are neighbours. This is called a mating restriction. The chance that this mating restriction is adhered to is defined by the conservation chance *Realb*. The function of *Realb* is generally to maintain the diversity of the entire population. *Realb* is limited to the domain [0,1], *T* is limited to be larger than zero and smaller than the population size. The neighbourhood size parameter *T* is specifically important. If *T* is too small, the two solutions selected for genetic operation are likely very similar, reducing the chance of exploring new areas in the search space. Conversely, if *T* is too large the two solution vectors will likely be too different resulting in poorly performing offspring. A large neighbourhood size will also increase the computational cost of the algorithm significantly [59].

5.3. Problem Penalties

The following two sections describe two possible improvements that can be applied to an optimization problem in order to increase the performance of the optimization algorithm. The first technique is called *objective normalization* and is described in Section 5.3.1. The second technique is called *scaled penalization* and is described in Section 5.3.2. The subsequent section, Section 5.3.3, describes the use of objective fitness penalties to steer the algorithm towards a finding a desired result. Finally Section 5.3.4 describes the method by which a close approach of the Sun is avoided. The descriptions in these sections serve only to introduce and describe these techniques. The result of implementing these techniques is provided in Chapter 6.

5.3.1. Objective Normalization

Objective normalization is a strategy described in the paper by Zhang and Li [59]. With this strategy the fitness values of the objectives are all normalized between the same minimum and maximum value. This technique is implemented in an attempt to improve performance in problem cases of disparately scaled objectives. A simple normalization method described by Zhang and Li is to replace each objective f_i with the result of Equation 5.2. In this equation $z^* = (z_1^*, ..., z_m^*)$ is the reference point, $z^{nad} = (z_1^{nad}, ..., z_m^{nad})$ is the nadir point in the objective space.

$$\overline{f}_i = \frac{f_i - z_i^*}{z_i^{nad} - z_i^*} \tag{5.2}$$

The reference points are calculated by:

$$z_i^* = min\{f_i(x) | x \in \Omega\} \tag{5.3}$$

The nadir point describes the upper bound of the Pareto front, and is calculated with:

$$z_i^{nad} = max\{f_i(x) | x \in PS\} \tag{5.4}$$

where PS is the Pareto Set. In this way the range of objectives in the Pareto front becomes bounded within [0, 1].

Objective normalization is most viable in objectives that have disparately scaled objectives, meaning that the fitness values of the objectives are of a different order of size. Zhang and Li simulate this by multiplying the value of the second objective by ten. The difference that objective normalization makes in this case is shown in Figure 5.7. It is difficult to predict the range of values the objectives in this thesis will return as, especially in the initial generations, the variable vector values are effectively random, only limited by the defined variable bounds. Therefor it is difficult to predict the necessity of this technique in the trajectory problems of this thesis beforehand. This will be easier to reflect upon with help from the results of the initial tests as described in Chapter 6.

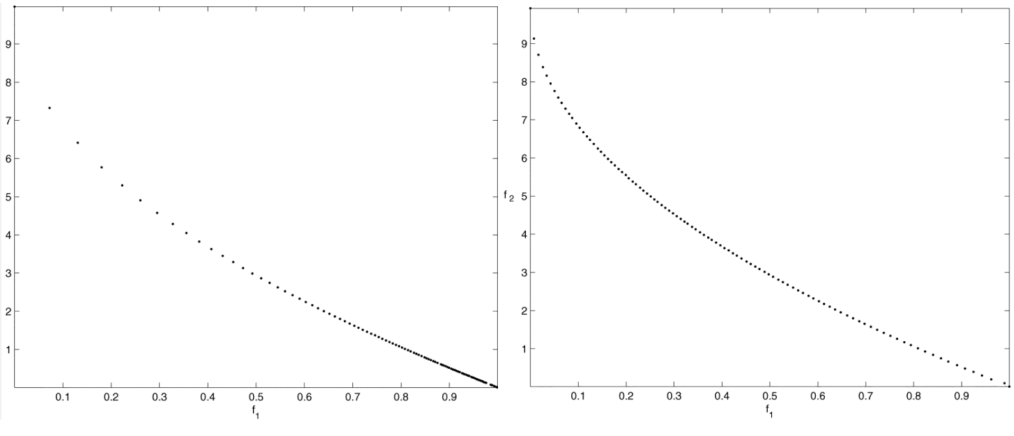

Figure 5.7: Plot of the fronts found by MOEA/D without (left) and with (right) objective normalization for a modified problem where f_2 is replaced by $10f_2$ [59].

5.3.2. Static and Scaled Penalties

The static or scaled penalty can be applied in the problem definition in order to help steer the solutions to a desired region. In this thesis a penalty can be applied to a solution when a trajectory does not reach the Kuiper Belt at all. In this scenario the final trajectory has to be elliptic with an aphelion distance that does not reach beyond 30.5 AU from the Sun. In this case it is an option to simply apply a static penalty value to one of the objectives, for example to the TTA parameter. By applying this penalty value, solutions that do not reach the Kuiper Belt are discouraged and they will ultimately be pruned from the population. In order to further guide the algorithm to desired solutions, a scaled penalty system can be applied. This is done by calculating the difference between the aphelion and the inner boundary of the Kuiper Belt and subsequently incorporating this difference value in the process of determining the magnitude of the penalty. The intention of the scaled penalty value is that it provides direct feedback into the fitness value of the objectives the closer the trajectory comes to reaching the Kuiper Belt. In a static penalty value this feedback system is far less obvious, only becoming apparent once trajectories that do reach the Kuiper Belt exist within the population.

The magnitude of the static or scaled penalty is another factor that is to be evaluated. A penalty that is too high can too aggressively prune premature but promising search space regions from the population. A penalty that is too small risks to be ineffective in discouraging unwanted results.

5.3.3. Objective Fitness Penalty

The same static or scaled penalty system can be applied to encourage certain objective fitness values themselves. For example, in order to encourage solutions with a TTA shorter than 25 years, any solution that has a TTA value of over 25 years can be applied an additional penalty. This additional penalty further discourages this solution and thereby encourages solutions with a shorter flight time. The same principle can be applied to the DSMDV parameter. For a solution to be realistic and viable, the DSMDV parameter of an evaluated trajectory has to be small. Discouraging solutions with a high DSMDV value by applying an additional penalty, either static or scaled, may consistently result in a better-quality population of solutions. However, this encouraging of low DSMDV solutions should not be too aggressive as it again has a chance of pruning underdeveloped regions early.

5.3.4. Sun Approach Penalty

The Sun approach penalty can be implemented to discourage and eliminate trajectories that approach the Sun too closely. As was discussed in Section 3.5, a minimum distance of 0.5 AU from the Sun is to be maintained over the entire course of the trajectory in order for it to be viable. Implementation of this Sun approach penalty should also be evaluated as it again runs the risk of pruning underdeveloped but perhaps interesting regions from the problem search space.

5.4. Trajectory Problem Optimization Procedure

This section presents an overview of the procedure in which the optimization problem is implemented and how the optimization algorithm is tuned. It then describes the process of interactive multi-objective optimization, the method used in this thesis project to identify the best solution in a large population of a multi-objective optimization. First, in Section 5.4.3 it is discussed how a two-objective problem is used to implement and preliminary test the implementation of PaGMO and the penalty systems. Then in Section 5.4.2 it is described how the four-objective problem is implemented and used for the tuning of the MOEA/D optimization algorithm. Finally, Section 5.4.3 describes the interactive multi-objective optimization method.

5.4.1. Two-objective Implementation Tests

Before the four-objective tuning process is started, a two-objective preliminary testing phase is performed in Chapter 6. In this phase the implementation of the trajectory model, the PaGMO libraries, the problem definition, and the possible penalty systems defined in Section 5.3 are evaluated. Testing is done on both the Cassini-2 and the Trident benchmark problems discussed in Section 5.1.3. These tests are done in a two-objective tuning process in order to make evaluation of the results easier. A population of four-objective solutions is much harder to plot, visualize and draw conclusions from, than a set of two-objective solutions. A two-objective result can be plotted in a Pareto front, easily indicating the quality of the results that are provided. Another key element to evaluate in this process is the consistency of the returned results regardless of, for example, pseudo-random number generator seeding. The two-objectives in this process are the parameter TTA, and a summation of DV and DSMDV.

During the two-objective optimization tests all four objectives are calculated and returned. However, the optimization algorithm MOEA/D only makes use of the mentioned DV plus DSMDV and TTA parameters to determine solution performance and iterate the population. Returning all four objectives enables the filtering of the solutions based on the TKB value as well, and provides otherwise void information.

The two-objective implementation tests are also used to prune certain settings from the MOEA/D tuning parameters if possible. As noted in Section 5.2.1, the first phase of the tuning process is to eliminate the worst-performing tuning settings. Eliminating one of the decomposition method options, for example, eliminates a large amount of work for the four-objective tuning phase. When eliminating one of the options it is important to keep in mind that the two-objective optimization likely has an entirely different optimally tuned algorithm than the four-objective problem. To reduce the risk of erroneously eliminating settings in this stage option elimination should thus only be performed when that option consistently produces poor results in all tests.

5.4.2. Four-objective Algorithm Tuning

In the four-objective tuning process of Chapter 7 all objective fitness parameters described in Section 4.5 are used by the MOEA/D algorithm to find an optimized Pareto set of solutions. In this tuning process the goal is to achieve a well-tuned algorithm and standardized process with which the Kuiper Belt trajectory, regardless of planetary flyby sequence, can be reliably optimized. As the model has been validated at this point, and the implementation of penalties and other options has been performed and evaluated in Chapter 6, the tuning of the MOEA/D algorithm settings can be isolated in this single section.

5.4.3. Interactive Multi-Objective Optimization

In a single-objective optimization of high-thrust trajectories, such as those performed by Musegaas and Melman, the optimal solution is a unique and optimal single solution clearly identified by its minimization of a lone objective fitness value. In a multi-objective problem identifying the best solution is typically a more complex process.

In this thesis the multi-objective optimization is done using an interactive approach as described by Miettinen et al. in [64]. This means that ultimately solving the multi-objective optimization problem reduces to helping a human decision maker, in this case the author, in identifying the Pareto optimal solution that is the most preferable option. This process necessitates the participation of a decision maker that has insight in the problem and who is able to specify preference to the objectives and to the Pareto solutions. In short the main steps of the general interactive method as described by Miettinen et al. are the following:

1. Initialize the problem.
2. Generate initial Pareto optimal starting point solutions.
3. Ask for preference information from the decision maker.
4. Generate a new set of Pareto optimal solutions.
5. Ask the decision maker to select the best solution so far.
6. Repeat from step 3 if necessary.

A downside of the interactive method is that it requires input from the decision maker during the iterative solution process. A major advantage is that it allows the decision maker to learn about the problem which improves their ability to justify why the final solution is the most preferred one [64].

With the four-objectives of DV, DSMDV, TTA, and TKB the iterative process described is implemented as shown in Figure 5.8. The initial set of Pareto optimal solutions is generated according to standardized base values of the minimum objective fitness. The DSMDV, TTA, and TKB minimum values are always the same, independent of planetary sequence: 5 km/s, 25 years, and 25 years respectively. The DV value is dependent of the planet upon which the first flyby is performed. For an inner Solar System planet the initial DV filter value is set at 5 km/s. For outer planets such as Jupiter and Saturn it is set at 10 km/s. Based on the resulting Pareto optimal solutions a new set of limits is inserted in order to generate a new set of Pareto optimal solutions. This adjustment can be either an increase or a decrease of a single or of multiple objective parameters. In most cases, however, the adjustment will be a reduction of the DV, DSMDV, and TTA values. This process is repeated until a set of filter values have been found which reduces the set of Pareto solutions to a manageable number of optimal solutions. From this final set of optimal solutions a selection of the best solution is finally made by the decision maker. This selection will be based on the remaining solutions and on the information gathered about the problem and solutions over the course of the entire interactive optimization procedure.

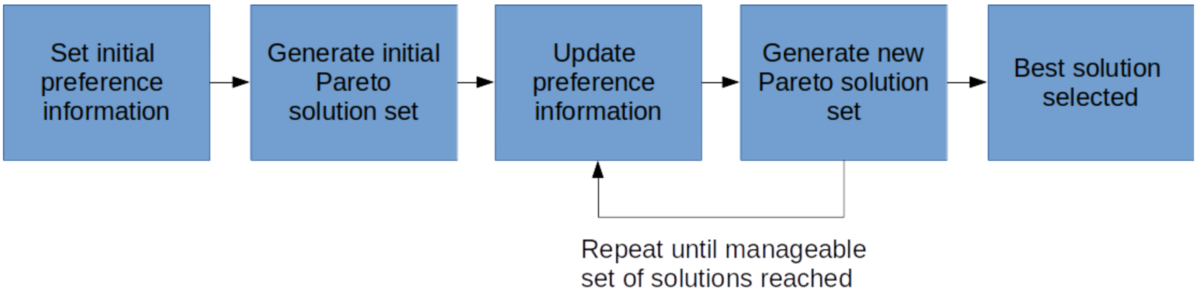

Figure 5.8: Schematic representation of the interactive multi-objective optimization method used in this thesis.

6

Two-objective Preliminary Testing

This chapter encompasses the implementation and testing of the various options and penalty systems that were described in Section 5.3, as well as an initial pruning of algorithm parameter settings. All this is done in a two-objective optimization environment described in Section 5.4.1. Section 6.1 provides a further introduction on the performed tests. Section 6.2 describes the Sun Approach Penalty used to prevent close encounters with the Sun. Then Section 6.3 describes the penalty system used to prevent trajectories that travel far out of the ecliptic plane. In Section 6.4 the use of static or scaled penalties is evaluated. The objective normalization technique is tested in Section 6.5. To test the algorithm and model before moving on to four-objective tuning, a two-objective optimization process is performed, which is documented in Section 6.6. Conclusions drawn from the preliminary testing phase are summarized in Section 6.7.

6.1. Introduction

The tests and results discussed in this chapter are a summary of the most important evaluations performed in the initial stage of the problem set-up. Over the course of the thesis project a large number of adjustments were continuously made to the problem and penalty implementations in order to achieve the most robust problem definition and solution.

Extensive preliminary optimization runs in the two-objective environment were performed with a large variety of MOEA/D algorithm settings. The results generated by all these runs were then grouped together and evaluated. The purpose of these test runs was three-fold. First, it allowed the problem to be extensively tested in order to identify and correct unforeseen issues that may arise. Second, the larger the number of solution data sets, the clearer it is where the true Pareto front of the problem is located. This in turn provides information for the interactive multi-objective optimization process. Third, by comparing the solutions generated by the various algorithm settings preliminary conclusions about the MOEA/D algorithm can be drawn. These conclusions can be used in the true algorithm tuning process in the four-objective environment.

As discussed in Section 5.1.3, the tests were performed on the Cassini-2 and the Trident benchmark problems, both of these tests are set-up to have a strong relevance to the Kuiper Belt problem of interest. The Cassini-2 problem was used to test penalty implementations as well as the objective normalization technique. The Trident problem was used as a test platform for variable bound adjustments and alternative flyby sequences, particularly the Neptune flyby. The proximity of Neptune to the Kuiper Belt was identified as a unique situation that was important to be analyzed before the true planetary sequence problems could be evaluated. All optimization runs with unique algorithm variants were performed five times, with five different seed numbers, as described in Section 5.2.2.

6.2. Sun Approach Penalty

An initial large test run was performed on the Cassini-2 problem before implementation of the Sun approach penalty. The range of MOEA/D algorithm settings used for this test are shown in Table 6.1. In total this test run contained 75 algorithm variants, aimed to investigate the influence of the decomposition method, neighbourhood size T, and conservation chance *Realb*. All trajectory solutions generated by this test were then grouped and processed. During this processing the Pareto solutions of the data set are identified by filtering out solutions that perform worse in both objectives than any other solution in the data set. The result of using this filtering system on the large data set is shown in Figure 6.1. The best solutions are reflected by the blue circular markers, the filtered solutions are indicated by the small red dots. The variants that provide a surviving solution are marked as superior.

Parameter	Values
Population size	1000
Generations	3000
CR	0.8
F	0.95
Decomposition method	Weighted/Tchebycheff/BI
T	20/40/60/80/100
Realb	0.5/0.6/0.7/0.8/0.9

Table 6.1: Range of parameters used for the initial two-objective test run on the Cassini-2 problem.

The surviving solutions are all resulting of optimization runs with the algorithm using the Tchebycheff decomposition method and a T value larger than 60. However, the approximate Pareto front does not form the concave or convex shape expected from a typical two-objective problem. Small clusters of outlier solutions are present scattered along the upper half of the approximated Pareto front. While one might initially identify these regions as sources for very well optimized solutions, however plotting the trajectory reflected by these outlier solutions immediately shows the necessity of a Sun approach penalty.

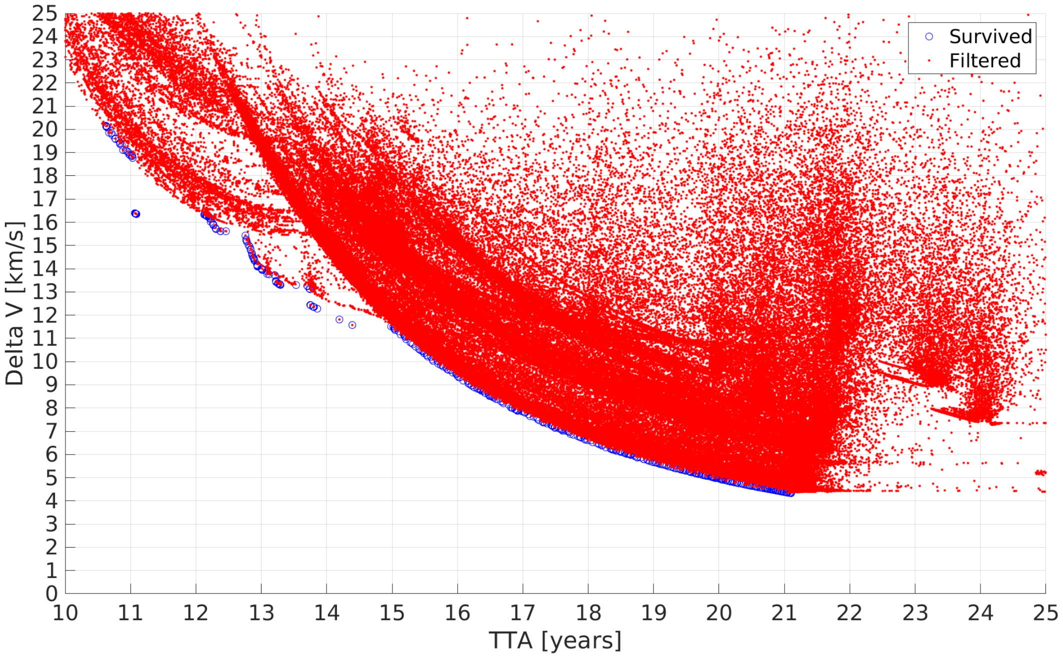

Figure 6.1: Pareto solutions of a preliminary test on the Cassini-2 problem using 75 different algorithm variants. No penalties of any kind were applied during this test.

The trajectory shown in Figure 6.2 is a reflection of the outlier solution near 11 years TTA and 16.2 km/s Delta V in Figure 6.1. Clearly this trajectory is not realistic as it crosses through the Sun after the Jupiter gravity assist. The other outlier solutions present similar trajectories, all with an extremely close Sun approach distance. To solve this problem, the Sun approach penalty is implemented. Using the orbital elements of the trajectory before the Kepler propagation, as well as the orbital elements after DSM application, the perihelion for both sections of the interplanetary leg can be calculated easily. If the orbit perihelion of either of these sections is smaller than 0.5 AU, the Sun approach penalty is applied. The value of the penalty itself was determined using a trial and error process. Ultimately a static penalty to the DSMDV parameter with a value of 10,000 m/s was found to efficiently eliminate all solutions with a close Sun flyby from the population. The positive effect of this penalty is reflected by the convex Pareto front shape in Figure 6.3, resulting from a test with only the 25 Tchebycheff algorithm variants in Table 6.1.

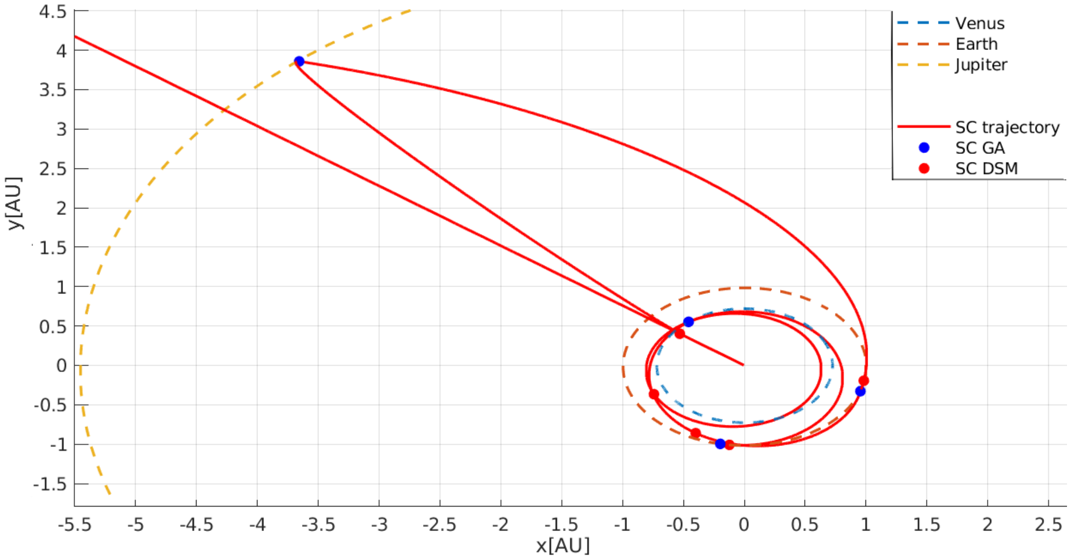

Figure 6.2: Close up of a section of a trajectory found without a Sun approach penalty implementation.

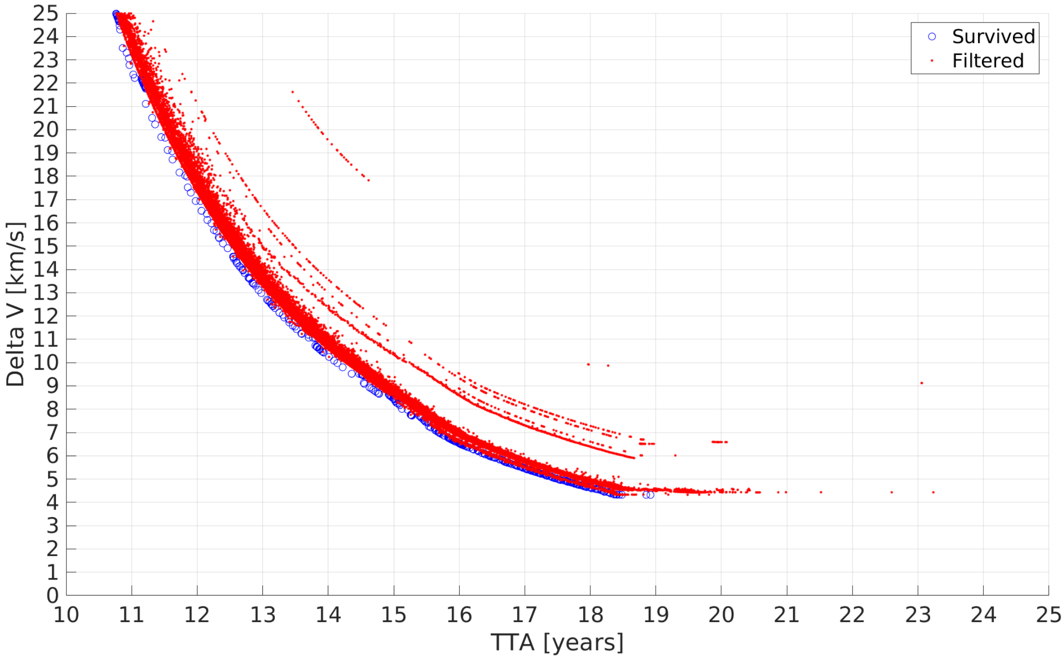

Figure 6.3: Improvement in the Pareto front shape and position as a result of the Sun approach penalty.

6.3. Inclination Penalty

During preliminary testing on the Trident problem it was found that in planetary sequences where Neptune is used as the last flyby planet, the optimization algorithm would find solutions that send the spacecraft into trajectories with significant inclinations with regards to the ecliptic plane. An example of such a trajectory is shown in Figure 6.4. The flyby of Neptune in this trajectory is performed at a b_{rot} angle such that the spacecraft sets course in a direction perpendicular to the ecliptic plane. As most Kuiper Belt objects are found within ten degrees of the ecliptic plane, as discussed in Section 2.2, this type of trajectory is not desirable.

Preventing these kinds of solutions can be done in multiple ways. One way would be to restrict the bounds of the b_{rot} variable in the reach leg, or to discourage the appropriate range of values for this variable using a penalty system. Restricting the bounds would not be a straight-forward solution, as due to the definition of the angle the allowable range of values is not continuous. Instead a more robust system similar to the Sun approach penalty is implemented. Using the orbital elements of the spacecraft after the DSM in the reach leg, the Z-coordinate of the trajectory at the inner boundary and outer boundary of the Kuiper Belt can be retrieved, as well as the Z-coordinate at the aphelion and perihelion. These values are encouraged to be kept within a value of one AU using the same implementation as the Sun approach penalty.

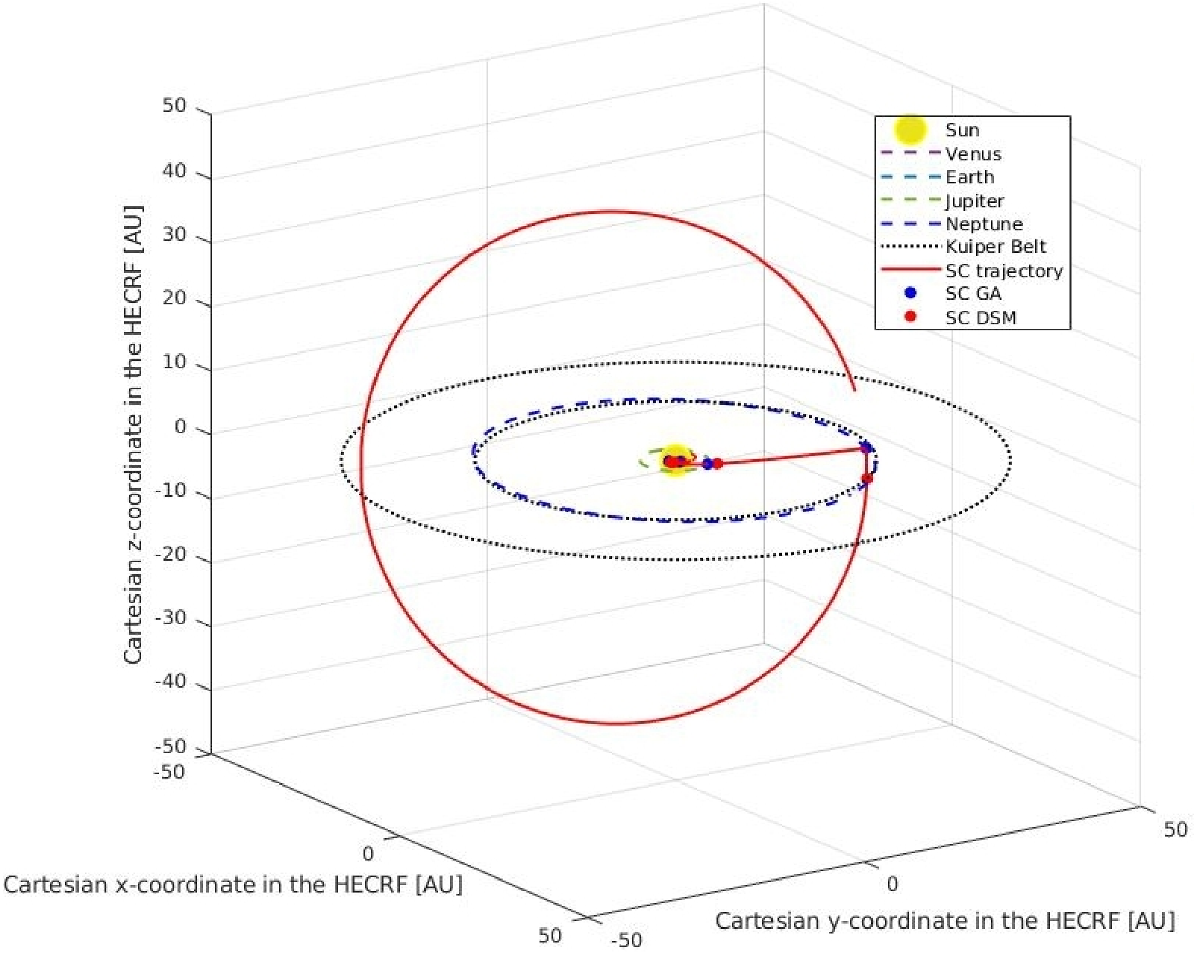

Figure 6.4: Undesirable trajectory that travels perpendicular to the ecliptic plane, as a result of a polar Neptune flyby.

6.4. Objective Fitness Penalties

The objective fitness penalties are applied to three different aspects of the problem. First, when an elliptic orbit does not reach the inner boundary of the Kuiper Belt, a TTA penalty is applied. Second, when the total TTA is over 25 years, a TTA penalty is applied. Third, when the DSMDV value surpasses 5 km/s, a DSMDV penalty is applied. Combined these penalties effectively guide the majority of optimization population to the desirable types of solutions. In order to keep things practical and the number of problem optimization variables reasonable, determining the magnitude of these penalties was relatively limited in a trial and error approach. The likelihood that small adjustments in these penalties will significantly improve the optimization efficiency or results is considered unlikely. The difference between a scaling and static penalty is much more considerable for reasons stated in Section 5.3.2.

A test to evaluate the performance difference between a scaling penalty and a static penalty system was performed in order to determine the most efficient method. This test is performed on the Cassini-2 benchmark problem with the standard MOEA/D algorithm values.

The penalty calculation schemes used in the static penalty versus scaling penalty test are shown in Table 6.2.

Scenario	Penalty parameter	Units	Static penalty	Scaling penalty
Not reaching KB	TTA	days	2500	2500 + KB_{pen}
TTA > 25 years	TTA	days	2500	1000 + 10(TTA - 25 · 365.25)
DSMDV > 5 km/s	DSMDV	m/s	7500	5000 + 10(DSMDV - 5000)

Table 6.2: Settings for the scaled and scaled penalty calculation schemes for three different scenarios.

The Kuiper Belt scaling penalty component KB_{pen} is calculated with:

$$KB_{pen} = 100 \cdot \frac{30.5AU - r_a}{AU} \tag{6.1}$$

where r_a in this case is the aphelion of the orbit after completion of the reach leg DSM, and AU is the astronomical unit in meters.

The results of the scenario with the static penalty system are shown in Figure 6.5, the results for the scaled penalty system are shown in Figure 6.6. The test was performed with five different seeds, indicated with the five different colours. In generation 50 it can be seen that in the scaled system, in four out of five seeds solutions have been found in the [0, 30] range of both variables. In the static penalty system this is true for only two out of five seeds. Solutions for all five seed numbers appear by generation 75 in the scaled penalty case. For the static penalty case this happens somewhere near generation 125. Beyond generation 125 it can be seen that the population converges to the approximate Pareto front relatively quickly in both cases, but that the static penalty system performs worse in this aspect as well. Seed 333 in the static system struggles to approach the approximate Pareto front that is found by generation 250 with all other seeds. This indicates that the static penalty system is less reliable to find the approximate Pareto front than the scaled penalty system. Furthermore, the range of relatively low Delta V solutions is much smaller in the static system case. The trailing end of the Pareto front is larger in the scaled penalty results, a much desired feature as it provides a wider range of trajectory options. This might be caused by the relatively sudden and aggressive point of penalty application for the static penalty case. In the scaled penalty system this tipping point is less severe, preventing the pruning of underdeveloped regions of the search space early on in the optimization run. Ultimately it is clear that the scaled penalty system is preferable, showing multiple advantages over static penalty application.

It should be noted that all objective fitness values described in this thesis are the true performance values unless indicated otherwise. The fitness values are not returned by the trajectory model with penalty values applied to them. The penalized fitness values are only used internally by the PaGMO optimization algorithm in order to judge the quality of solutions in the current population.

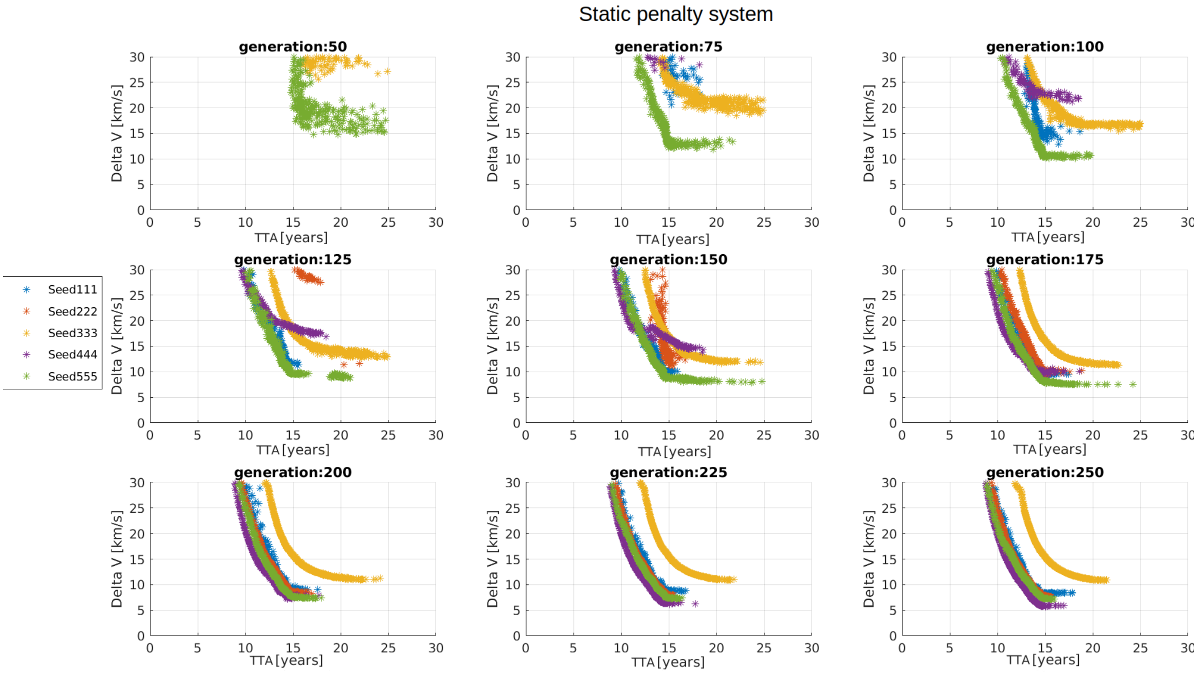

Figure 6.5: Result of the Cassini-2 benchmark problem using the static penalty system.

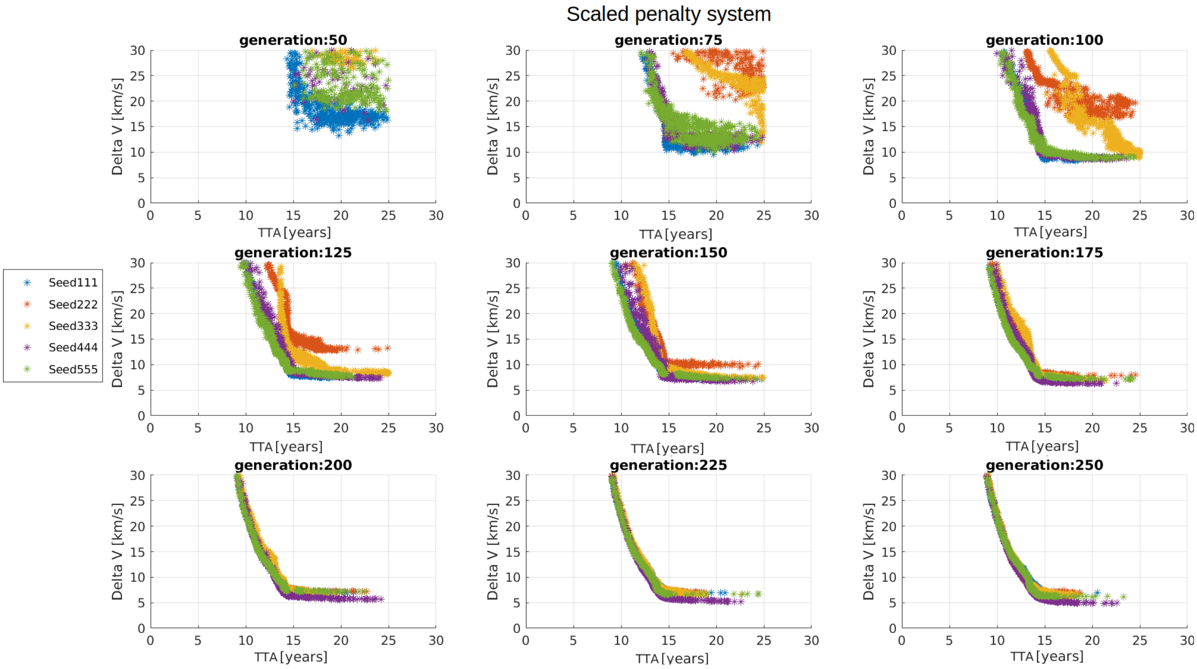

Figure 6.6: Result of the Cassini-2 benchmark problem using the scaled penalty system.

6.5. Objective Normalization

The normalization technique as described in Section 5.3.1 was attempted within the Cassini-2 benchmark problem and using two-objective optimization. First, the population fitness values of the current generation were retrieved. From this population the reference and nadir points were calculated in accordance to Equations 5.3 and 5.4. These values were then used to calculate the new fitness value for each objective using Equation 5.2. Subsequently these new fitness values replaced the fitness values of the current population. At this point the generation was evolved as usual by the MOEA/D algorithm.

The MOEA/D algorithm was tuned using the default parameters, with a population of 1,000, and made to evolve for 3,000 generations, repeated with five seed numbers. The results of this optimization run are shown in Figure 6.7. Unfortunately these results are not as expected and something in the implementation of the technique is clearly wrong. While the TTA values are reasonable, the Delta V values are extremely large, reaching values of over 400,000 km/s. The Delta V values are also concentrated around certain regions, with hardly any solutions deviating from these concentrated areas. The variation in the Delta V and TTA value between generations is extremely small, making them unnoticeable in the figure.

Attempts were made to improve the implementation of the objective normalization technique, but these efforts were ultimately abandoned due to time constraints of the project. The possible extent of improvement for interplanetary trajectory problems as a result of objective normalization thus remains unclear in this thesis. Nevertheless, as described in Section 5.3.1, the order of the difference in the objective fitness values are an important indicator for the necessity of this technique. This difference between objective fitness values can also be kept artificially small by specifying appropriate units to the returned values if possible. For example, by calculating the Delta V values in m/s and the TTA in Julian days, or by calculating the Delta V values in km/s and the TTA in years, the difference in magnitude between the fitness values of the multiple objectives can be influenced. This pragmatic technique was utilized by calculating TTA and TKB in Julian days, and DV and DSMDV in m/s. With these units the order of difference between different objective values was found to be relatively small both at the start as at the end of an optimization run.

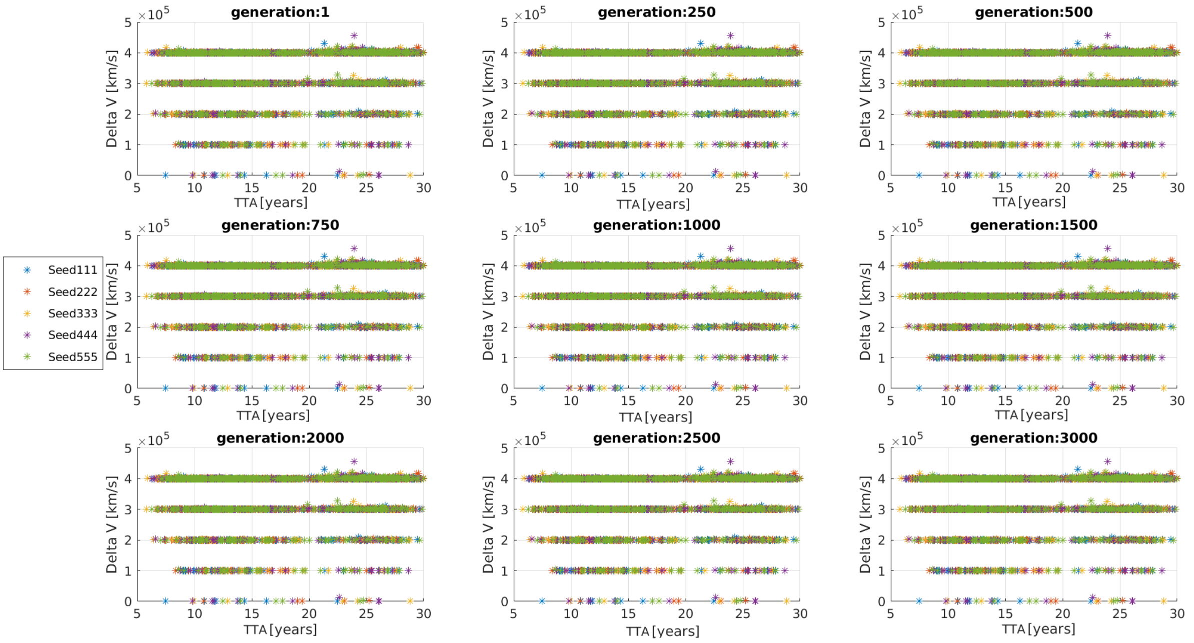
generation:1 generation:250 generation:500
generation:750 generation:1000 generation:1500
generation:2000 generation:2500 generation:3000

Figure 6.7: Results generated during the optimization of the Cassini-2 problem with application of the objective normalization technique.

6.6. Two-objective Test Trajectory

To finalize the two-objective preliminary testing phase, an algorithm tuning run was performed using 24 algorithm variations. Since the weighted decomposition method was outclassed by the Tchebycheff decomposition method in the test in Section 6.2, this test run made use of only the Tchebycheff method. The complete set of algorithm setting variants is summarized in Table 6.3.

Parameter	Values
Population size	1000
Generations	3000
CR	0.7/0.8/0.9/1.0
F	0.3/0.4/0.5/0.6/0.7/0.8
Decomposition method	Tchebycheff
T	20
Realb	0.9

Table 6.3: Range of parameters used for the final two-objective test run on the Cassini-2 problem.

The grouped result of these 24 optimization runs is shown in Figure 6.8. The solutions were filtered in an iterative process, as describe for by the interactive multi-objective optimization method, to find the best set of solutions. The best solutions are indicated by the blue circles in the figure. These solutions adhere to the following set of limits:

- DV < 5 km/s
- TTA < 18.5 years
- TKB > 10 years
- DSMDV < 0.7 km/s

Using these filters, 238 solutions concentrated in a very small region remain from the initial 120,000. Clearly however, the front portrayed in Figure 6.8 is quite broad, meaning that variants do not converge to a single approximate line. Between the variants no clear best tuned algorithm was found. The 238 remaining solutions were the product of two different algorithm settings, with no obvious correlation. Slightly broadening the filter limits quickly increases the number of variants that show up in the list of surviving solutions.

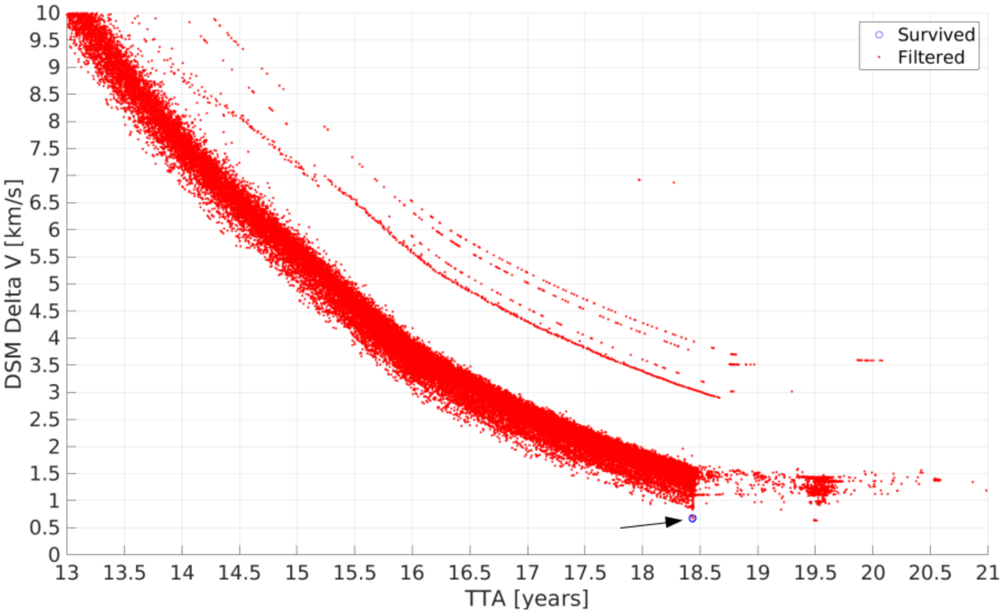

Figure 6.8: Pareto set of the preliminary two-objective optimization results for the Cassini-2 problem.

From the remaining 238, the solution with the lowest DSMDV parameter is plotted and shown in Figure 6.9. Note that because this trajectory is based on the Cassini-2 problem, the dates of this trajectory are of course in the past. Regardless, the trajectory is as expected, featuring a low DV, DSMDV, and TTA value, but a sub-optimal TKB parameter. As the TKB parameter was not a part of the optimization process at all during the two-objective optimization, it is no surprise that the final resulting trajectory is a hyperbolic solution. The hyperbolic trajectory is the most likely orbit form to achieve a low TTA value. A goal of the four-objective optimization solutions is to achieve efficient elliptical orbits intersect the Kuiper Belt as well.

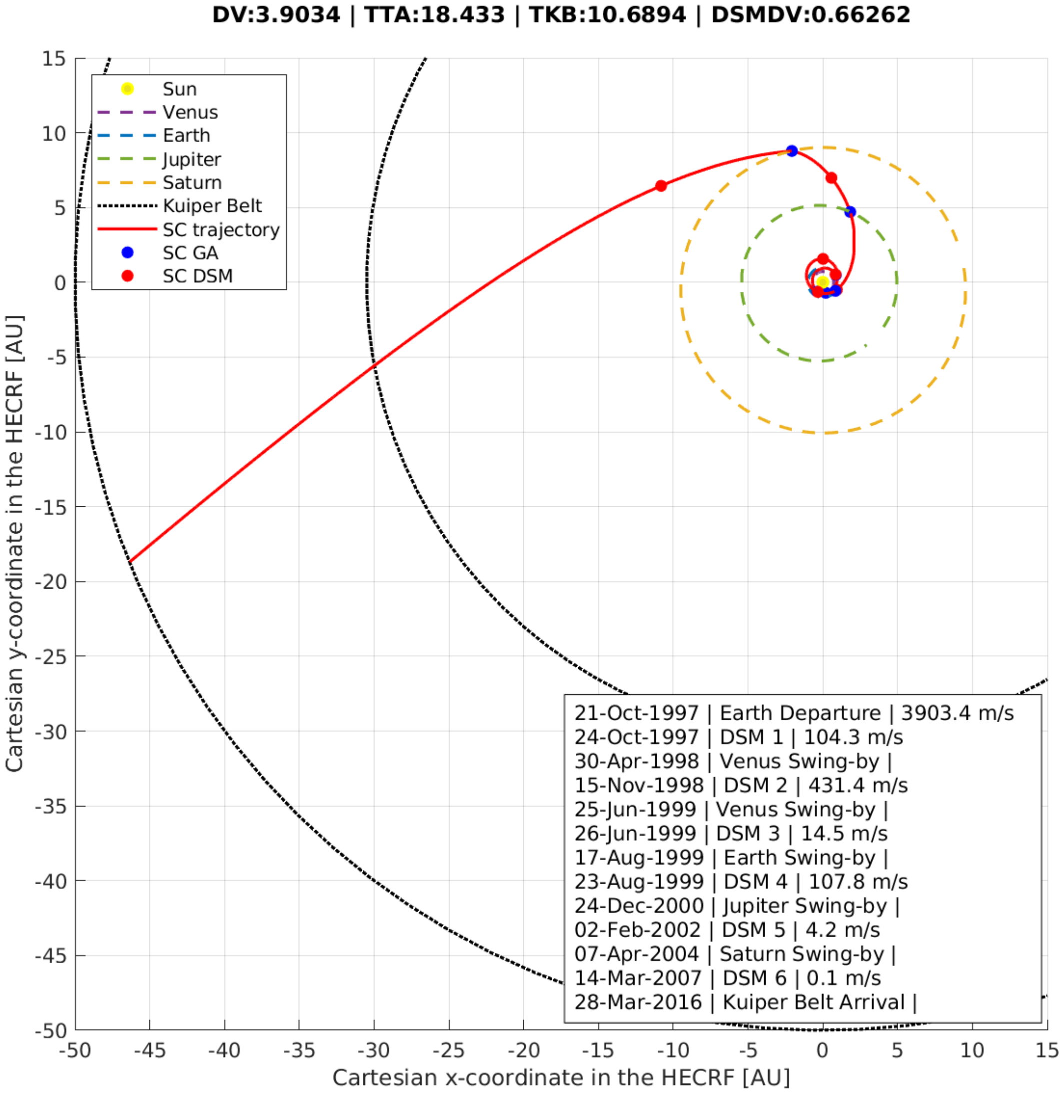

Figure 6.9: Trajectory to the Kuiper Belt found as a result of two-objective optimization in the Cassini-2 problem.

In regards to tuning the MOEA/D algorithm not many conclusions can be drawn at this stage. No cohesive or common algorithm settings were found during the two-objective optimization tests. Only the use of the weighted decomposition method has been eliminated from the range of tuning settings, as it continuously achieved worse results than the Tchebycheff method. The BI algorithm also performed badly in preliminary tests, but as the BI algorithm is likely much better at problems with more than two objectives it will not be eliminated as an option at this point. Further tuning of the MOEA/D algorithm will be performed in the four-objective optimization environment described in Chapter 7.

6.7. Conclusions

For convenience a summary of the conclusions drawn from the two-objective preliminary tests is listed here. These conclusions will be used in the four-objective optimizer tuning phase where possible.

- The population shall be kept at 1000 as this successfully creates the desired wide array of solutions that create a well populated and broad spectrum of options.
- The algorithm will run for a maximum of 3000 generations based on the tests that indicate results of the two-objective optimization still adjusting considerably up to this point.
- The use of the weighted decomposition method will be excluded due to its consistently inferior performance in comparison to Tchebycheff method.
- Approaching the Sun by a distance less than 0.5 AU implements a DSMDV penalty to discourage the algorithm from iterating upon unrealistic solutions.
- An inclination penalty system is implemented within the trajectory section that passes through the Kuiper Belt, in order to discourage trajectories that significantly deviate perpendicularly to the ecliptic plane.
- The penalty for not reaching the Kuiper Belt will be scaled with the distance by which the inner boundary is missed. This penalty is applied to the TTA parameter.
- A scaled DSMDV penalty is applied when the DSMDV objective value exceeds 5,000 m/s, in order to discourage solutions with unrealistically high DSM capability requirements.
- A scaled TTA penalty is applied when the TTA objective value exceeds 25 years, in order to discourage solutions with an undesirably long time-of-flight to the Kuiper Belt.
- Due to literature specifying that the BI decomposition method is preferable in a multi-objective problem, it will be included in the four-objective testing phase.
- It is concluded that the implementation of a objective normalization system might be beneficial, but is nonetheless abandoned in this thesis due to project time constraints and implementation issues.

7

Four-objective Optimizer Tuning

This chapter describes the process to achieve a reliable method of optimizing four-objective interplanetary trajectories. This method will be used to optimize the various trajectory problems for a long-duration flight in the Kuiper Belt that are described in Chapter 8. In the tuning process the Cassini-2 and Trident benchmark problems will be used instead. As mentioned earlier, both of these problems share a number of commonalities with the Kuiper Belt trajectory problems which are to be optimized. The initial stage of the four-objective tuning process is to optimize the Cassini-2 problem using a large number of algorithm variants, as documented in Section 7.1. Then in Section 7.2 it is explained how the solutions are further optimized by constraining the variable bounds. The conclusions of this chapter, including an summary of the final optimization method, are provided in Section 7.3.

7.1. Algorithm Variants

Initially the Cassini-2 problem is again used in the four-objective benchmark case. The model adjustments and the problem implementations summarized in the conclusion of Chapter 6 are used. In the four-objective optimization all objective fitness values described in Section 4.5 are used by the MOEA/D algorithm to evaluate the quality of solutions in the population. To find the best settings for the MOEA/D algorithm for this problem and these objectives, a large optimization test is performed using 288 algorithm variations. These variations are shown in Table 7.1. The decomposition method is limited to Tchebycheff and BI, meaning that 144 variants will be performed with use of each of these two techniques. The *CR* and *F* variation is centered around the default values of these parameters, with a step-size of 0.1. The neighbourhood size *T* is increased from the default value of 20 to a minimum value of 60 based on the results of the test performed in Section 6.2. The conservation chance *realb* is varied from the default value of 0.9 down to 0.6 using a step-size of 0.1. As usual each algorithm variant is performed with the standard five different seed numbers in order to also evaluate the reliability of a certain optimizer setting.

Parameter	Lower bound	Upper bound	Step size
Population size	1000	-	-
Generations	3000	-	-
Weight generation method	Grid	-	-
Decomposition method	Tchebycheff	BI	-
Cross-over rate *CR*	0.8	1.0	0.1
Scaling factor *F*	0.4	0.7	0.1
Neighbourhood size *T*	60	100	20
Conservation chance *realb*	0.6	0.9	0.1

Table 7.1: Variants included in the four-objective benchmark case, resulting in a total of 288 algorithm variants to be tested.

After each iterating for 3,000 generations these 288 variants return 1,440,000 optimized trajectory solutions in total. In order to conclude which algorithm variant is most reliable in producing optimized solutions these solutions are first processed by simply filtering out inadequate solutions. This initial filter consists of the following limits:

- DV < 5 km/s
- TTA < 25 years
- TKB > 25 years
- DSMDV < 5 km/s

The solutions that pass this filter are then processed through a Pareto filter, removing any solution that performs worse in all four objectives than any other solution in the entire population. After both these filters 158,327 solutions remain and no algorithm variant has been completely eliminated yet as each variant has at minimum one surviving solution remaining.

At this point the reliability of each algorithm variant is brought into the selection process. This is done by using the fact that each algorithm variant run was repeated with five seed numbers and by counting the number of different seed numbers each algorithm variant has in the remaining solution set. A variant which finds good solutions with all five initial seed numbers is clearly a more reliable algorithm than a variant that only manages to find good solutions with a single seed number. Using this idea on the remaining 158,327 solutions and filtering out all variants that are unable to find sufficient solutions with all five seed numbers, finally a large portion of the algorithm variants are removed from the pool. After this process 26 algorithm variants remain, nine of these utilizing the Tchebycheff decomposition method, the other seventeen using the BI method.

The intention is to find a much more select number of algorithm variants; using 26 variants with five seed numbers on each trajectory problem would not be feasible as the computation time would be significant. Instead the number of surviving algorithms is further reduced by decreasing the DSMDV objective filter value. Setting the DSMDV filter value to 3 km/s reduces the number of variants to 13, all of which use the BI problem decomposition method. Finally reducing the DSMDV filter to 1 km/s causes five algorithm variants to remain. These five variants are listed in Table 7.2.

Four out of these algorithm settings use of a CR value of 1.0 and a F value of either 0.5 or 0.6. Further a T value of 60 and a $Realb$ value of 0.6 is most common. There are deviations from these settings, including a relatively high T value of 100 and an F value of 0.7. Instead of further tuning the algorithms with knowledge of these results, or simply selecting one of these remaining five, it is decided that using all five of the shown algorithms for the future optimization problems. Running these five algorithms with five seed numbers for 3,000 generations and a population of 1,000 takes significant computational time but does have the best chance of finding high quality results. To further improve the results a second step in the optimization process of a problem is performed. This step is discussed in Section 7.2.

Variant Nr	Name	Decomposition method	T	Realb	CR	F
181	MOEAD1	BI	100	0.6	1.0	0.6
217	MOEAD2	BI	80	0.7	1.0	0.5
265	MOEAD3	BI	60	0.7	1.0	0.5
278	MOEAD4	BI	60	0.6	1.0	0.6
281	MOEAD5	BI	60	0.6	0.9	0.7

Table 7.2: The settings of the five best performing versions of MOEA/D determined in the four objective problem tuning process.

7.2. Focusing Variable Bounds

The five best performing algorithm variants found in Section 7.1 are now applied to the Trident benchmark problem. The results are plotted using two objectives: TTA on the x-axis and DSMDV on the y-axis. The DV and TKB objectives are not immediately reflected in this figure, instead they are used as a filter parameter. The minimum TKB value is set at 25 years. The maximum DV value is set at 5 km/s. Using the interactive multi-objective optimization method the maximum DSMDV value is ultimately set at 1.5 km/s. The result of this is shown in Figure 7.1. In this plot every algorithm is shown with its own colour, enabling a better visualization of each algorithm's behavior. The downward triangles indicate solutions that adhere to the set minimum objective limits. The dots indicate solutions that have failed in one or more of these objectives. Algorithms 4 and 5 were able two find two regions in which good solutions are present. However, it is unclear whether the true optimum in these regions have been found. The other three algorithms returned did not find these optimum regions, indicating that using all five algorithm runs for each problem is necessary to find good results.

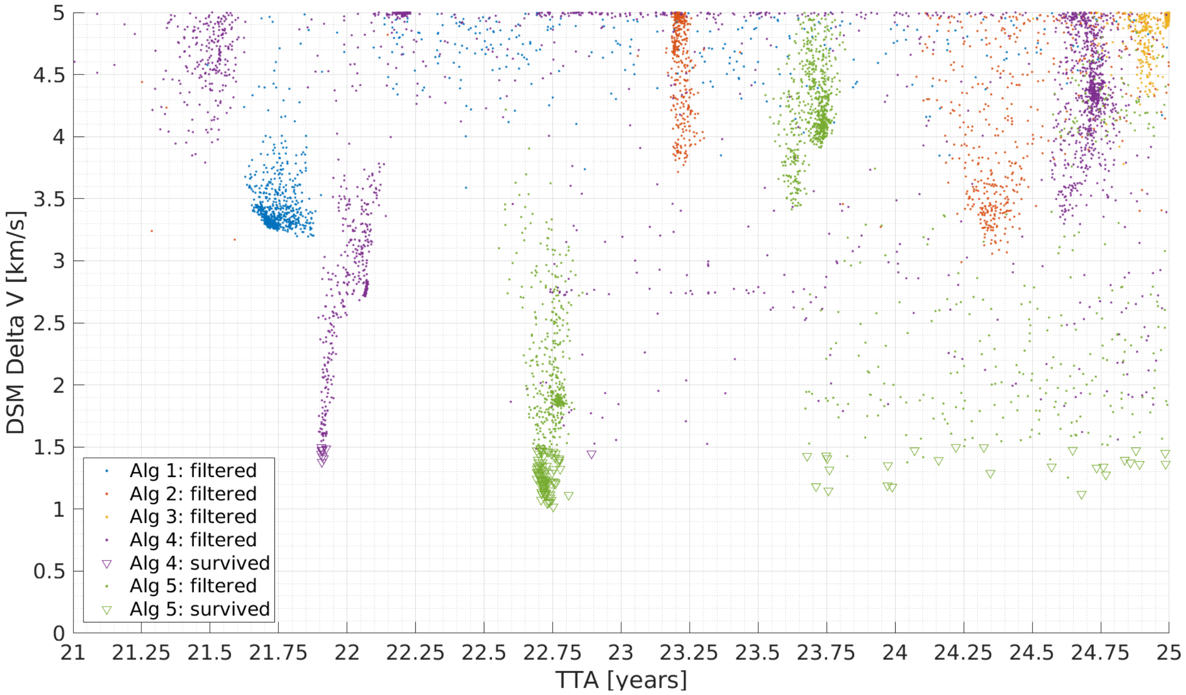

Figure 7.1: Trident benchmark problem global optimization result using the five best performing algorithm settings. The population was subsequently filtered by placing limits on all four objective fitness values in order to locate two promising regions in the search space.

To further investigate the quality of the solutions found by algorithm 4 and 5, the decision vectors that reflect these search space regions are investigated. As an example, a section of the population data for the best results in Figure 7.1 is shown in Table 7.3. Using this population data two new optimization runs are performed. One with variable bounds based on the variant 4 solutions, and one based on the variant 5 solutions. When these new bounds are selected, the launch date, transfer leg times, and launch velocity are prioritized, as these are considered the most significant trajectory variables.

Variant	Departure [MJD2000]			Leg 1 [days]			Leg 2 [days]		
	Min	Max	Mean	Min	Max	Mean	Min	Max	Mean
4	14528	14535	14533	365.08	365.32	365.22	221.82	228.70	224.62
5	12442	12452	12447	184.16	186.18	184.85	106.35	118.03	111.53

Table 7.3: Variable vector data of the departure date and the first two interplanetary legs for the best solutions produces by algorithm variants 4 and 5 for the Trident benchmark problem.

The result for the case where the bounds were narrowed based on the best solutions of variant 4 are shown here in Figure 7.2. Clearly the quality of the solutions has improved significantly in terms of DSMDV. Again using the interactive multi-objective optimization method the best solutions have been deduced from this solution set. The solutions in this figure are filtered with the same DV and TKB values as before but with a maximum TTA of 23.25 years and a maximum DSMDV of 0.75 km/s.

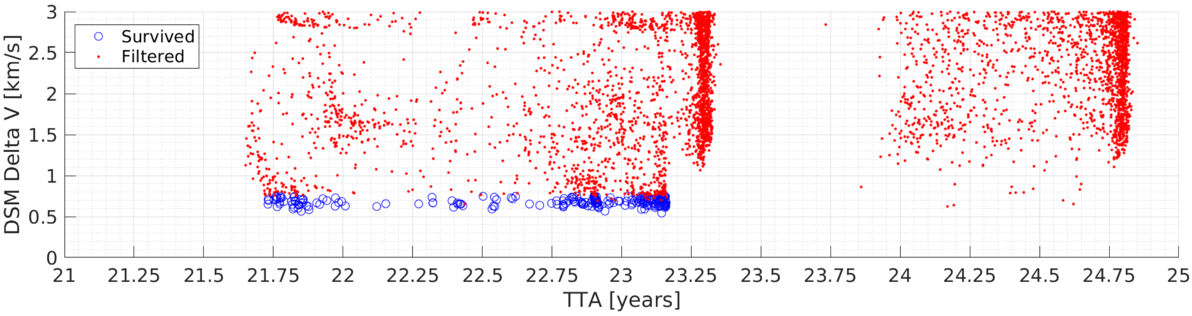

Figure 7.2: Result of optimizing the Trident benchmark problem using five algorithm variants and using bounds narrowed around the best results of variant 4 in the global search.

The 20 best solutions from this optimization run are summarized in Table 7.4. These solutions were selected by taking the five best solutions in terms of each of the four objectives individually. It is then up to the decision maker to ultimately select the most optimal solution. As the TKB and TTA values in the population are all relatively close together, the solutions that perform best in these categories are not likely to be selected. Furthermore, the DV launch value of all solutions are below 4.5 km/s, corresponding to a low C_3 of approximately 20 km^2/s^2. The DSMDV value is then considered the most important objective to select the single-best solution on in this case. Prime choices would be option 19 or 20, but first the result of focusing the bounds on algorithm variant 5 solutions should be considered.

Set	ID Number	DV [km/s]	TTA [years]	TKB [years]	DSMDV [km/s]
Best DV	1	3.66	23.12	96.24	0.72
	2	3.65	23.14	96.37	0.74
	3	3.65	23.08	95.55	0.74
	4	3.65	23.14	95.84	0.74
	5	3.63	23.16	96.37	0.75
Best TTA	6	3.82	21.76	93.35	0.71
	7	4.11	21.75	93.37	0.71
	8	3.92	21.73	93.38	0.70
	9	3.89	21.73	93.41	0.71
	10	4.00	21.73	93.36	0.65
Best TKB	11	4.34	23.10	96.47	0.63
	12	4.49	23.16	96.55	0.69
	13	4.50	23.15	96.58	0.70
	14	4.50	23.15	96.58	0.69
	15	4.49	23.15	96.58	0.66
Best DSMDV	16	3.96	23.07	94.97	0.59
	17	4.26	21.88	93.54	0.58
	18	4.25	22.94	95.75	0.57
	19	4.20	21.85	93.48	0.56
	20	4.03	23.14	95.46	0.54

Table 7.4: Twenty best results of the Trident benchmark problem using five algorithm variants and using bounds narrowed around the best results of variant 4 in the global search.

The result for narrowing the bounds around variant 5 of the global search is shown in Figure 7.3. The range of solutions in terms of TTA is much narrower in this case. All five of the optimization algorithm variants have found solutions that are present in the indicated blue region. These solutions in the blue region are filtered using a maximum DV and DSMDV of 5 and 0.6 km/s respectively. The maximum TTA and minimum TKB were set at 22 and 25 years. Using these filters 54 solutions remain.

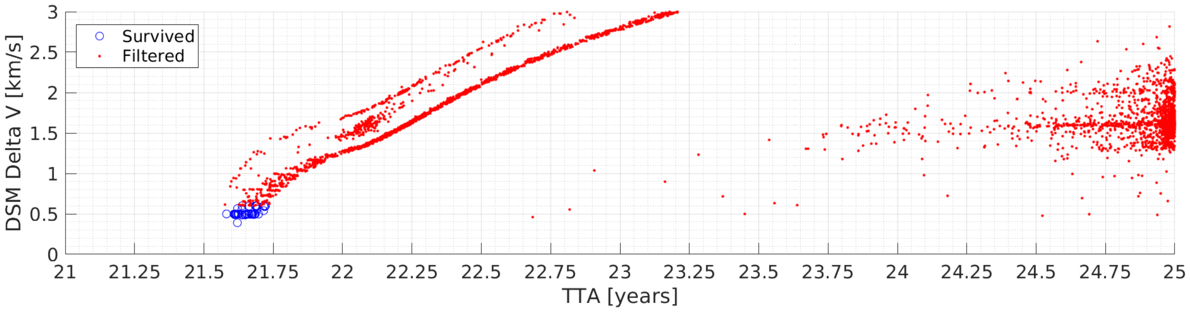

Figure 7.3: Result of optimizing the Trident benchmark problem using five algorithm variants and using bounds narrowed around the best results of variant 5 in the global search.

Again, the twenty best solutions from this set of 54 solutions are summarized in Table 7.5 by again selecting the five best solutions in each category. While the DV parameter is consistently larger in these solutions, the DSMDV value is consistently lower. In a trade-off between these two parameters the DSMDV value is always likely to be the better option. The TTA of these solutions is always shorter than 22 years and the TKB surpasses 100 years easily. It is clear that these solutions are better. Ultimately it can be decided that the best solution for this problem is thus number 20 shown in Table 7.5, as the ten extra years of Kuiper Belt exploration are almost negligible in a time-frame of 120 years of flying through the Kuiper Belt. This trajectory is shown and discussed in Section 8.1.3.

Set	ID Number	DV [km/s]	TTA [years]	TKB [years]	DSMDV [km/s]
Best DV	1	4.43	21.65	130.52	0.50
	2	4.43	21.63	130.32	0.50
	3	4.42	21.62	129.90	0.50
	4	4.42	21.62	129.89	0.50
	5	4.42	21.62	119.50	0.39
Best TTA	6	4.44	21.61	131.37	0.50
	7	4.48	21.61	129.47	0.49
	8	4.49	21.61	130.56	0.50
	9	4.46	21.58	128.67	0.50
	10	4.46	21.58	128.67	0.50
Best TKB	11	4.43	21.69	136.44	0.60
	12	4.48	21.72	136.49	0.60
	13	4.48	21.72	136.74	0.59
	14	4.48	21.72	136.88	0.60
	15	4.43	21.72	137.30	0.60
Best DSMDV	16	4.46	21.65	130.55	0.49
	17	4.48	21.61	129.47	0.49
	18	4.43	21.64	130.74	0.49
	19	4.48	21.65	130.71	0.49
	20	4.42	21.62	119.50	0.39

Table 7.5: Twenty best results of the Trident benchmark problem using five algorithm variants and using bounds narrowed around the best results of variant 5 in the global search.

7.3. Optimization Method Conclusion

This section summarizes the findings of this chapter and thereby establishes the procedure of problem optimization to generate the trajectory results in Chapter 8. A schematic representation of the optimization procedure is shown in Figure 7.4

The used algorithm settings are shown in Table 7.6. For optimization of each trajectory problem these five algorithms are used consecutively with five different initial population seeds. The results are then pooled together. Pareto and objective fitness filters are applied to all four objectives using the interactive multi-objective optimization method until a manageable set of solutions remains. This concludes the global problem optimization phase, at which point a more localized optimization phase is started.

The decision variables of the set of global solutions are processed in order to establish narrow bounds based on the initial set of best solutions. This typically results in two or more new problem definitions with localized variable bounds. These problems are again optimized using the same five algorithm variants and five different initial population seeds. The results of each localized optimization problem is then again evaluated using the interactive multi-objective optimization method.

Ultimately a data set of the 20 best solutions for each local problem is generated. This set of 20 solutions is small enough in order to finally make an informed decision to select the most optimal trajectory solution for the respective optimization problem.

Name	Decomposition method	T	Realb	CR	F
MOEAD1	BI	100	0.6	1.0	0.6
MOEAD2	BI	80	0.7	1.0	0.5
MOEAD3	BI	60	0.7	1.0	0.5
MOEAD4	BI	60	0.6	1.0	0.6
MOEAD5	BI	60	0.6	0.9	0.7

Table 7.6: The settings of the five best performing versions of MOEA/D determined in the four objective problem tuning process.

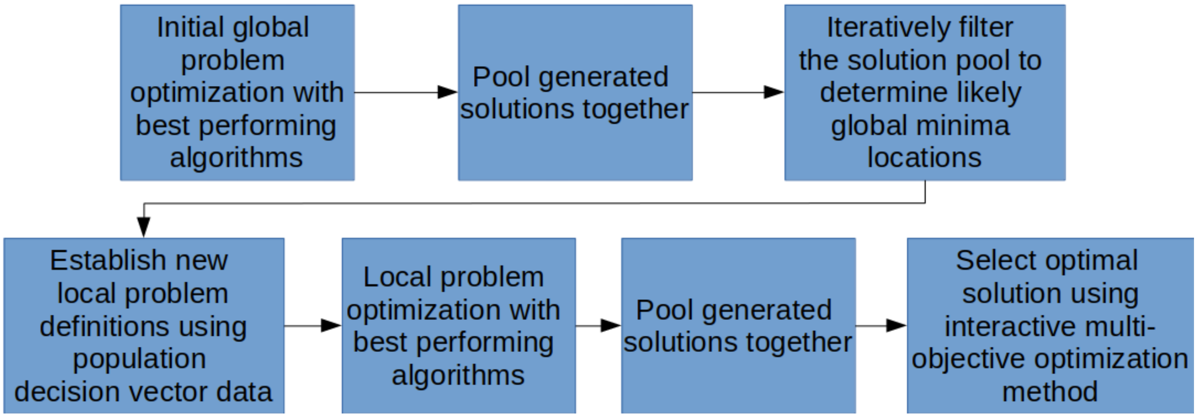

Figure 7.4: Schematic overview of the problem optimization procedure used to generate the results in this thesis.

8

Results

This chapter presents and discusses the found trajectory solutions that enable long-duration flight through the Kuiper Belt. The selection and evaluation of the initial planetary sequences are discussed in Section 8.1. Based on these results five additional sequences which end in a Jupiter-Neptune flyby were analyzed. These additional sequences are discussed in Section 8.2. A short study on the launch windows of the five best performing flyby sequences is shown in Section 8.3. Finally, in Section 8.4, the trajectory parameters of the best performing trajectories are translated into allowable spacecraft mass estimations.

8.1. Initial Planetary Sequences

The optimization of the trajectories is done based on the four objectives which are repeated here for convenience:

- **DV:** The launch energy required to initiate the trajectory, supplied completely by the launch vehicle. Equal to the hyperbolic excess velocity V_∞, and to the root of the launch energy parameter C_3.
- **DSMDV:** The ΔV required to perform the Deep Space Maneuvers of a trajectory.
- **TTA:** The time of flight between spacecraft launch and spacecraft entry of the Kuiper Belt.
- **TKB:** The time between entry of the Kuiper Belt and exit of the Kuiper Belt by the spacecraft.

The initial set of planetary flyby sequences is established based on the trajectory optimization results for a mission to Neptune by Melman [36], the KBO flyby trajectory optimization results in the study by Zangari et al. [2], the Argo mission proposal by Hansen et al. [22], and the Trident mission study by Mitchell et al. [23]. Combined these studies result in two sets of ten sequences, one set with relatively low C_3 requirements, and one set with higher C_3 requirements. The 20 initial trajectories and their sources are shown in Table 8.1. The optimization of these trajectories is done according to the procedure described in Section 7.3.

The sequences that have Earth or Venus as their first flyby planet are optimized with an upper boundary on the V_∞ variable of 6 km/s, which is in correspondence with a maximum launch energy of 36 km^2/s^2. This launch energy is not sufficient for trajectories that aim to launch directly towards Jupiter or Saturn for their first flyby maneuver. In those scenarios the maximum C_3 value is increased to 150 km^2/s^2, corresponding with a V_∞ of 12.5 km/s. This distinction is made in order to narrow the variable bounds and thereby increase the efficiency of the optimization algorithm. As discussed in Section 3.1, for solutions where the launch energy rises above 100 km^2/s^2, an additional upper stage such as the STAR48 solid rocket motor which was used for the launch of the New Horizons and the Parker Solar probe, would most likely be required. Note that trajectories with such a high required launch energy are very limited in their maximum deployable payload mass.

Nr	Melman [36]	Zangari [2]	Argo [65] and Trident [23]	Initial Set Low C_3	Initial Set High C_3
1	EJ	J	SN	EJ	J
2	EJS	JS	JSN	EJS	JS
3	EJSN	JU	EVEEJN	EJSN	JU
4	VEMS	JN		EVEEJN	JN
5	VEJS	JSU		VEMS	JSU
6	VVEJS	SU		VEJS	JSN
7	VVEE	SUN		VVEJS	JUN
8	VVEEJ	SN		VVEE	SU
9	VVEMJ			VVEEJ	SUN
10				VVEMJ	SN

Table 8.1: The two initial sets of planetary sequences that are evaluated and their sources.

8.1.1. Optimization results

For each sequence the 20 best results based on DV, DSMDV, TTA, and TKB were compiled first. From these 20 solutions a selection was made manually based primarily on the DSMDV value. The DSMDV value is considered the most important indicator on whether the proposed solution is feasible. As mentioned earlier, the fitness values DV and TTA are already limited by upper bounds in the search space and by a penalty system in the optimization algorithm. The DV and TTA values were considered when the DSMDV difference between solutions was negligible or when there was a large discrepancy between the DV or TTA values of a solution range. The final selection was made manually in order to judge each trajectory solution critically and to prevent the risk of pruning an optimal or otherwise interesting solution. The solutions of the VEMS, EJSN, JSN, JUN, and SUN sequence were removed from the results as these routes did not provide a realistic solution. Between the years 2025 and 2040 there exists no adequate alignment between Jupiter, Uranus and Neptune, or between Saturn, Uranus and Neptune. The solutions for these routes required excessive DSMDV capabilities of over 5 km/s in order to patch the planetary flybys together. The VEMS solution was removed because it required a larger DSMDV than launch DV which is inefficient and undesirable. These outliers have been removed from the results in order to produce a clearer and more concise figure. The selected optimal results of the remaining 15 sequences are summarized in Figure 8.1. The sequences are ordered in ascending launch DV value which is the first indicator of the required launch vehicle capabilities and of the maximum allowable mass for the specified trajectory. The left axis specifies the DV requirement for launch and DSMs in km/s scale. The right axis indicates the TTA and TKB value in years. The more exact objective fitness values for each trajectory are shown in the data table beneath the graph.

In the figure a clear distinction is made between the fitness of the four objectives, however, the optimal route is dependent on the exact requirements and goals of the mission. In any case it is clearly possible to fly a trajectory which deploys a spacecraft in the Kuiper Belt for an exceptional amount of time. The required C_3 value ranges from 15.1 to 128.2 km^2/s^2, which means this type of mission can be done with either a high-velocity New Horizons type launch or with a lower launch energy, multiple gravity assist, Trident type mission. The time to arrival ranges from 15 years for the very fast Jupiter Neptune trajectory, to 25 years for the VEJS trajectory. The graph also clearly shows that the use of DSMs is minimal for several of the routes. The J, JS, and JU routes require less than 50 m/s of onboard propellant for pure DSMs, which is about a quarter of the capability of a spacecraft such as New Horizons. The flight time inside the Kuiper Belt is consistently extremely long, ranging from 89 to 203 years, with the longest TKB times being achieved with trajectories that perform a Neptune flyby. In the following sections the VVEJS, EVEEJN, and JN sequence trajectories will be discussed in more detail.

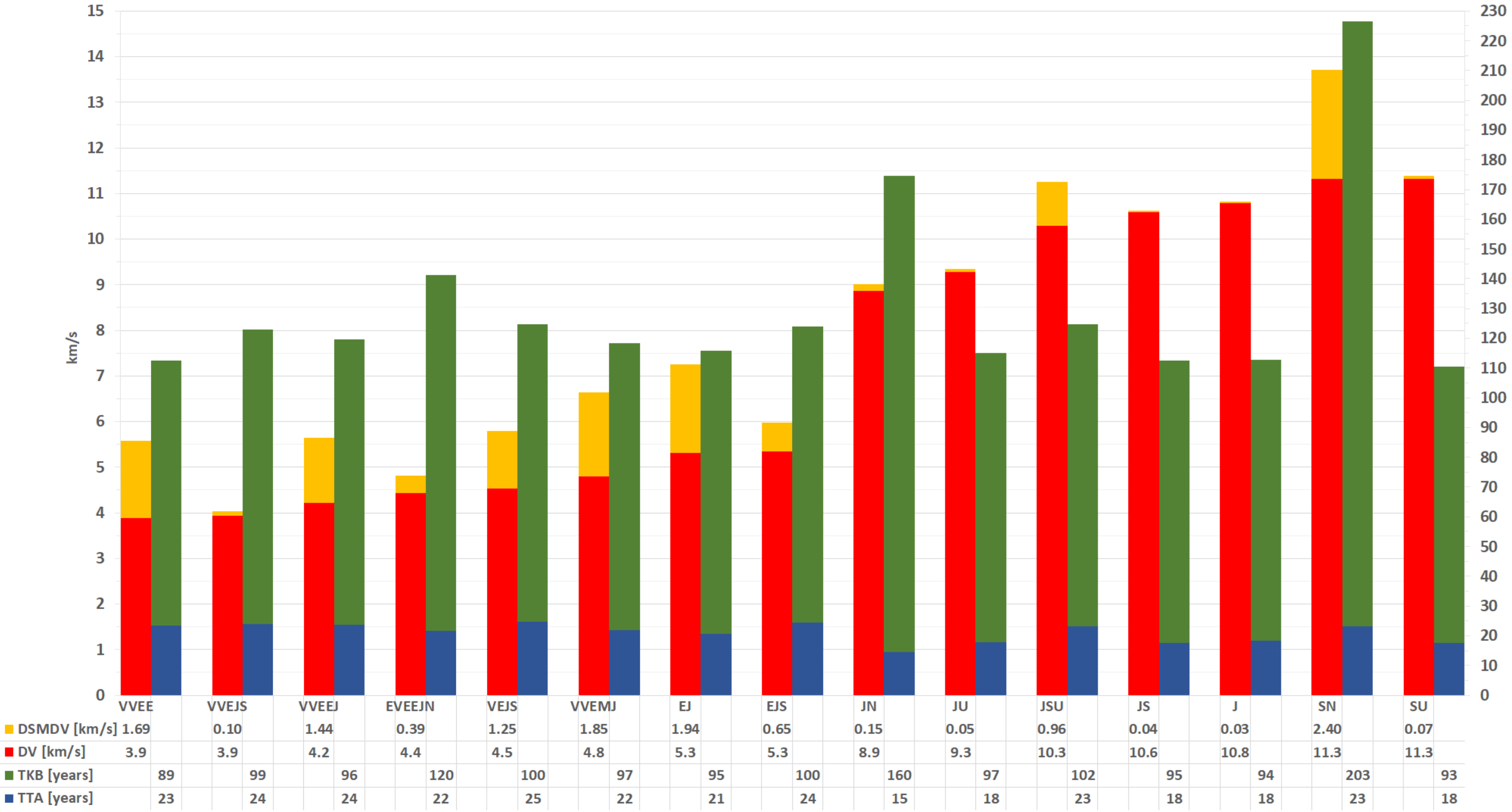

Figure 8.1: Results of the 4-objective optimization for the initial planetary sequences.

8.1.2. VVEJS trajectory

The VVEE route, which only performs swing-bys of inner Solar System planets, is able to reach the Kuiper Belt in less than 24 years and then remain there for almost 90 years. In order to do this the spacecraft does need to perform significant DSM burns. Better options exist for a low C_3 launch scenario, with the best performing routes being VVEJS and EVEEJN. The VVEJS route is shown in Figure 8.2.

Launching in February 2033, this trajectory makes use of an exceptionally efficient sequence of Venus and Earth flybys in order to build up sufficient velocity to slingshot towards Jupiter and finally Saturn. The Kuiper Belt is reached in February of 2057, almost exactly 24 years after launch. The time to arrival of this trajectory is thus near the upper boundary of the 25 year maximum that was set. In return for this long travel time it features a very low required C_3 of 15.5 km^2/s^2, a very small DSMDV requirement of 102 m/s, and almost a 100 years of flight time through the Kuiper Belt. The combination of low C_3 and small DSMDV requirement provides the opportunity to launch a heavier spacecraft with a large instrument suite, or the option of utilizing a smaller and likely cheaper launch vehicle. The closest approach distance to Jupiter in this trajectory is 3.9 Jupiter radii. The launch window for this trajectory with minimal variation spans from the 25th to the 27th of February 2033. As will be shown in Section 8.3, slightly increasing the C_3 budget from 15.5 to 19 km^2/s^2 increases the duration of this launch window to the 24th of March the same year. At that point however, it might be more attractive to consider the EVEEJN route, which is shown and discussed in the next section.

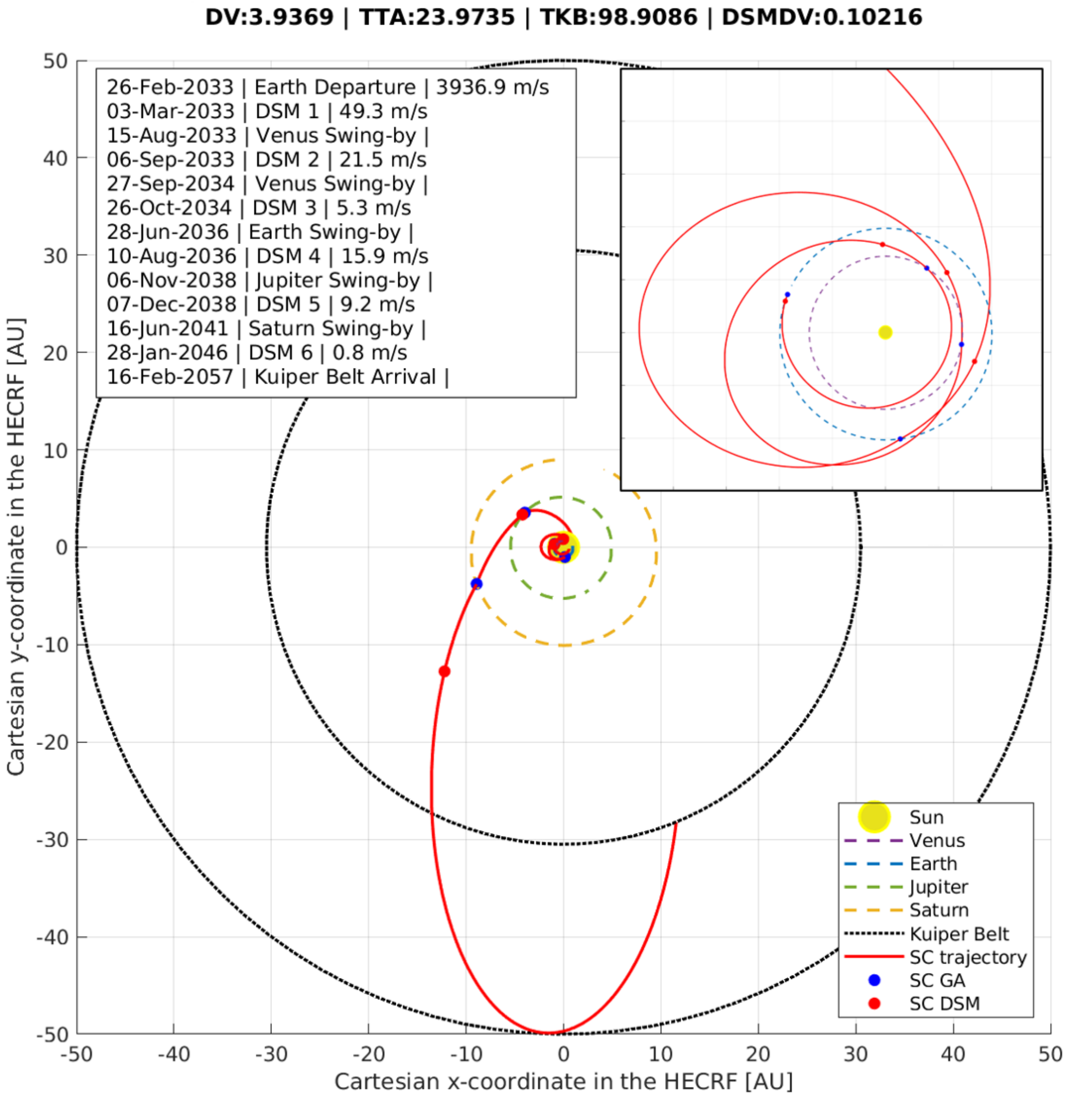

Figure 8.2: Plot showing the selected optimized VVEJS flyby sequence trajectory.

8.1.3. EVEEJN trajectory

The EVEEJN route, shown in Figure 8.3, requires a slightly higher C_3 parameter of 19.6 km^2/s^2, and a higher 390 m/s of DSM capability than the VVEJS route, but reaches the Kuiper Belt in 21.5 years instead of 24. It also remains in the Kuiper Belt longer than the VVEJS route, having a Kuiper Belt flight duration of over 119 years. Similar to the VVEJS route discussed earlier, this route uses the inner planets to build up velocity in order to set up a Jupiter gravity assist. Instead of targeting Saturn with this Jupiter flyby this trajectory sets course towards Neptune. The Neptune flyby is then used to massively alter the orbit of the spacecraft, reducing both the aphelion and the eccentricity of the final orbit. By using Neptune instead of Saturn to remain in the Kuiper Belt, the EVEEJN route achieves a shorter time of flight even though it utilizes an extra inner Solar System planet flyby to set up the Jupiter assist. Using this method this trajectory is able to launch in May 2035, two years later than the VVEJS trajectory, yet reach the Kuiper Belt sooner, in January 2057. The sensitivity study in Section 8.3 finds solutions for this trajectory between May 30th and June 8th of 2035, indicating that the launch window for this sequence is quite narrow. With minimal adjustments solutions from this initial optimization run range from the 17th to the 25th of May. Because this sequence is the only trajectory that makes use of six gravity assists and six DSMs it is also the most complex of the evaluated solutions.

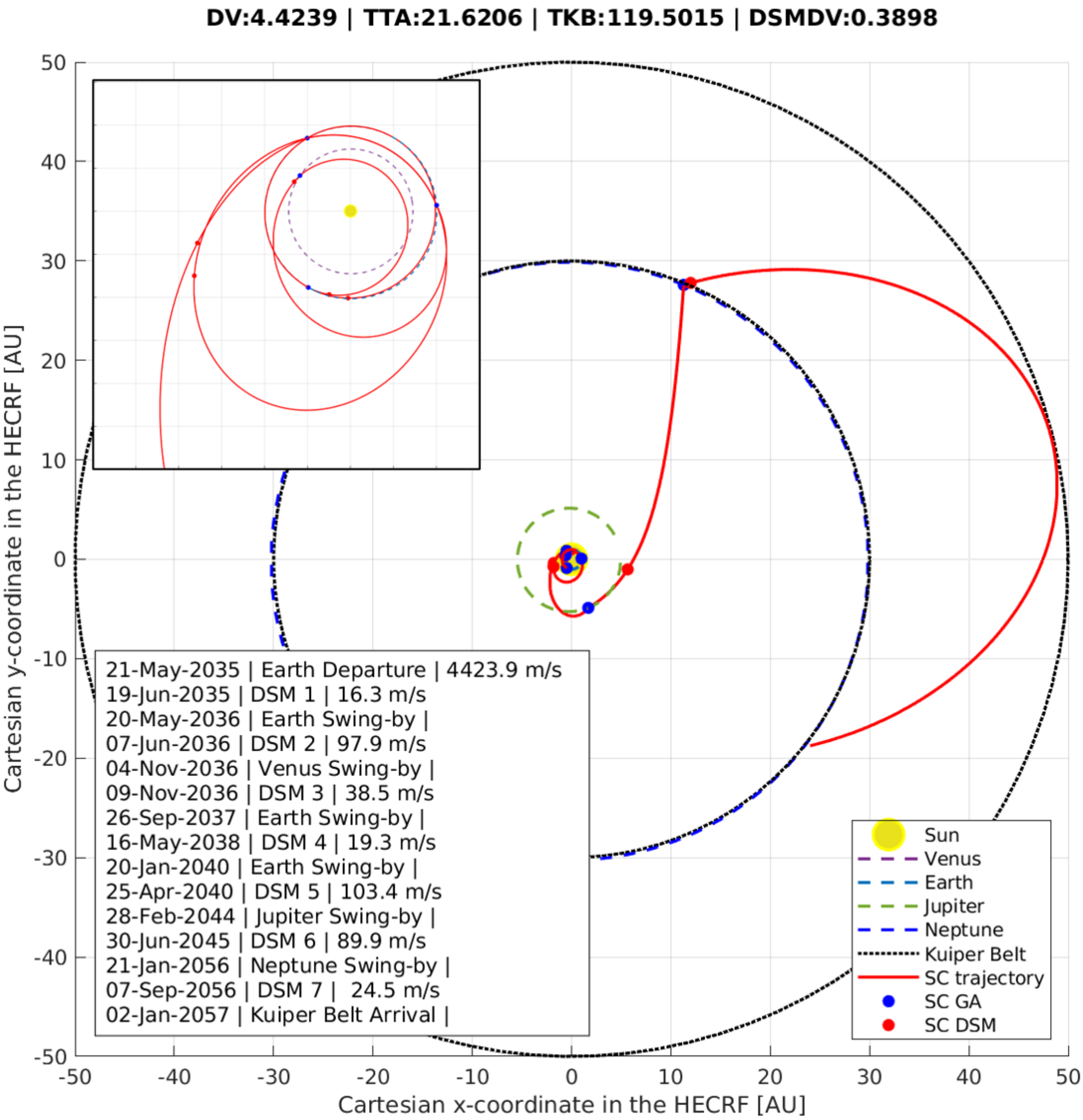

Figure 8.3: Plot showing the selected optimized EVEEJN flyby sequence trajectory.

8.1.4. JN trajectory

The shortest TTA trajectory is the JN sequence. Using a high velocity launch, requiring a C_3 of 78.5 km^2/s^2, sets up a direct flyby of Jupiter. Where the previously discussed VVEJS and EVEEJN routes spent over six years to set up the Jupiter flyby, this sequence reaches Jupiter two years after launch. The Neptune flyby is used in a similar way as in the EVEEJN route, reducing the aphelion and eccentricity of the final orbit. In this case the eccentricity is reduced to just 0.39, creating an orbit with a perihelion of 22 AU. Performing a burn of 355 m/s at aphelion would raise that perihelion to 30 AU, and a burn of 920 m/s would circularize the orbit to 50 AU. The initial phase of this trajectory is quite similar to the New Horizons trajectory, utilizing both a high C_3 launch and a Jupiter assist to reach the Kuiper Belt in a relatively short time. New Horizons however, was launched at a much higher velocity than is proposed in this solution, as it reached Jupiter just five months after launch. The JS and JU trajectories are quite similar to the JN trajectory shown here, except they use Saturn or Uranus respectively to reduce heliocentric velocity and set up the final orbit aphelion to remain inside the Kuiper Belt. As explained in Section 8.1.3, the planet Neptune is more efficient for this purpose, cutting down on the time to arrival and increasing TKB. Due to the higher C_3 value, the allowable spacecraft mass for this trajectory would be either more restricted or more expensive to launch than for the earlier discussed VVEJS and EVEEJN routes.

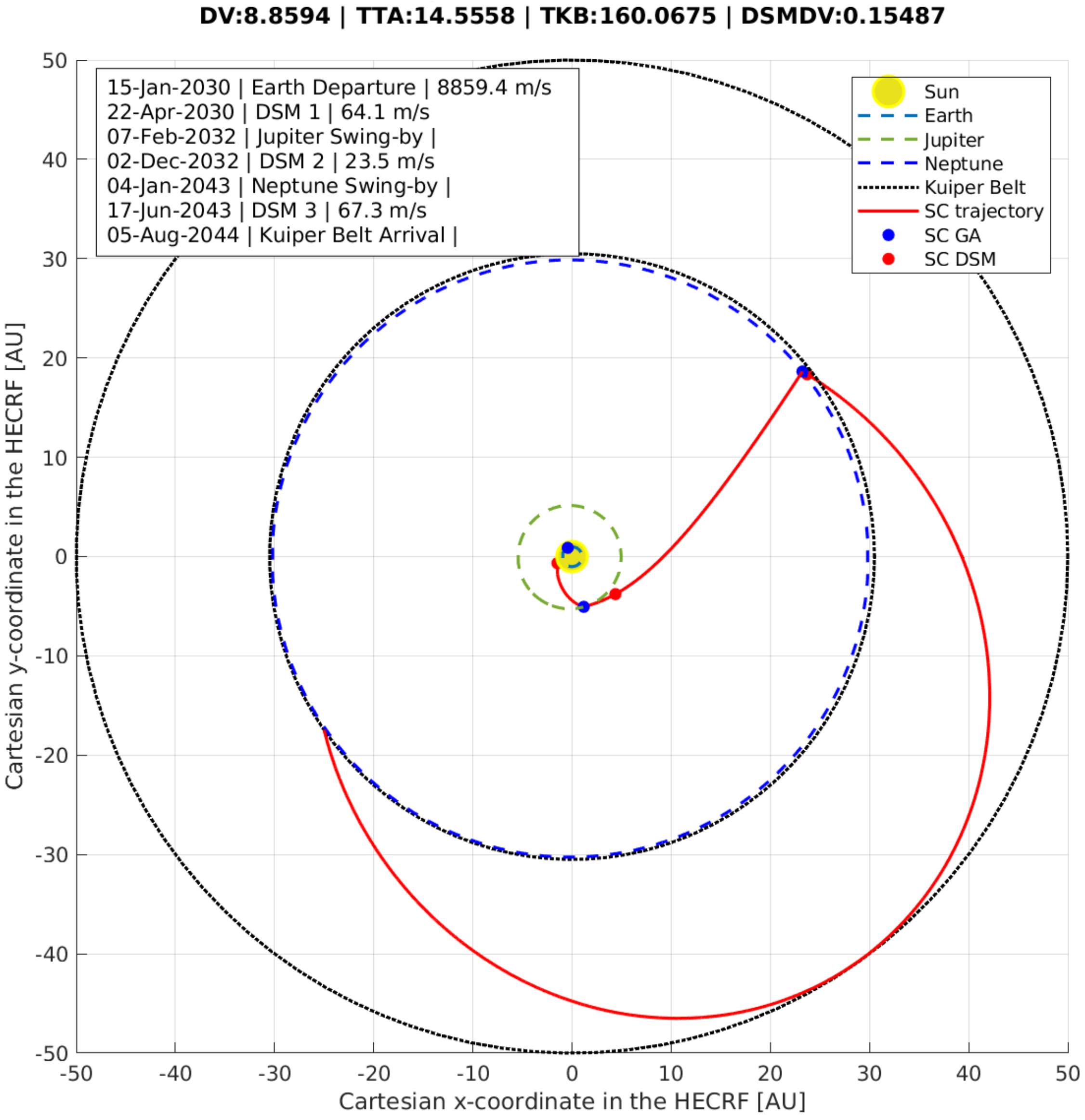

Figure 8.4: Plot showing the selected optimized JN flyby sequence trajectory.

8.1.5. Conclusions

The heliocentric velocity of the three selected trajectories is plotted against the flight time in Figure 8.5. The data shown in this plot support the conclusions drawn in the previous sections. The VVEJS and EVEEJN trajectories use the inner planets to increase their velocity in order to perform the Jupiter flyby. The JN trajectory performs the Jupiter flyby directly, but requires a higher initial heliocentric velocity to achieve this. The plot also annotates each trajectories last planetary flyby. It is clear to see how the Saturn flyby reduces the velocity less significantly as the spacecraft has over 20 AU to traverse before the Kuiper Belt is reached. The routes that use Neptune to reduce velocity are significantly faster as they travel this same distance at a higher velocity, only reducing their velocity at Neptune, which is positioned at the inner edge of the Kuiper Belt.

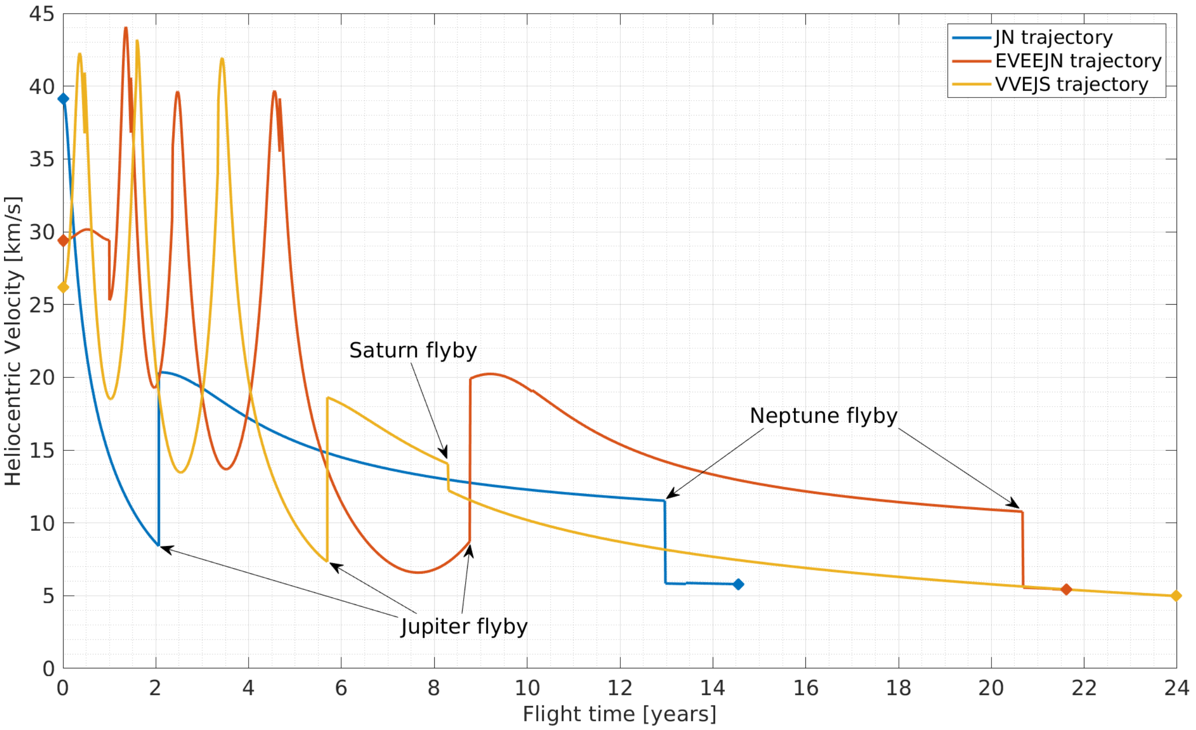

Figure 8.5: Heliocentric velocity over flight time until moment of Kuiper Belt entry for the JN, EVEEJN, and VVEJS trajectories. Note the reduction of velocity during the final planet flybys in order to achieve an orbit aphelion placed inside the Kuiper Belt.

Based on these three trajectories and the results of the other sequences shown in Section 8.1, it is concluded that a long-duration Kuiper Belt trajectory is certainly possible. The initial sequence results show viable trajectories with a relatively low C_3 launch parameter and a longer time to arrival of up to 25 years, as well as high velocity launches that are able to reach the target zone in 15 to 18 years. The optimal route for this mission type thus mostly depends on the desired mass of the spacecraft and on the intended launch date. These two factors will be further explored in Sections 8.3 and 8.4. The most viable low C_3 routes which were identified are EJS, EVEEJN, and VVEJS. For the high C_3 launch scenarios the best identified trajectories are J, JS, JU, and JN, These trajectories all make use of a Jupiter flyby, indicating that this planet is an important aspect of reaching the Kuiper Belt efficiently. For a mission aiming to achieve an extremely long Kuiper Belt flight time, a trajectory which employs a Neptune gravity assist is especially favorable.

The different trajectory solutions have also shown the possibility to fly both prograde and retrograde trajectories through the Kuiper Belt. The EVEEJN and JN trajectories, shown in Figures 8.3 and 8.4, are achieve a retrograde orbit as a result of the Neptune gravity assist. This means that the spacecraft would be flying against the orbital direction of the KBOs. The VVEJS trajectory shown in Figure 8.2 travels in prograde direction and will therefor fly in the same direction as the KBOs. It can be argued that a retrograde orbit is the preferable option as the spacecraft will likely encounter a larger number of bodies over the course of its mission when their orbital directions are opposite.

Furthermore, it is observed that the final DSM of the optimized trajectories is relatively small. In the discussed trajectories this maneuver is performed only in order to place the aphelion of the final orbit exactly on the defined outer edge of the Kuiper Belt at 50 AU. This way the TKB value can be maximized at the expense of a relatively small increase in DSMDV. However, in the shown JN trajectory data it can be clearly seen that performing this maneuver is not necessarily desirable. Of the total 155 m/s DSMDV requirement, almost half is applied after the Neptune flyby in order to maximize the TKB value. Eliminating this DSM from the JN trajectory would reduce the DSMDV requirement by 43.4% to just 87.57 m/s. For the EVEEJN trajectory eliminating the final DSM would cause a reduction of 6.3% in the DSMDV requirement. In the VVEJS trajectory the final DSM is implemented as intended. Its magnitude is almost negligible, comparable in size to a minor course correction maneuver, while maximizing the TKB value.

8.2. Additional Jupiter-Neptune Sequences

The results of the initial sequences in Section 8.1 show that the Jupiter to Neptune flyby sequence is a promising gateway to achieve a fast and efficient trajectory towards the Kuiper Belt. The Jupiter flyby allows a reduction of the required launch energy and time to arrival, while the Neptune flyby enables the potential for long-duration Kuiper Belt flight time as well as an opportunity to more easily achieve a retrograde final orbit direction.

The use of Jupiter over Saturn to reach Neptune is based on two main advantages that using Jupiter has. First, the mass and therefor gravitational attraction of Jupiter is larger, allowing larger bending angles, more efficient maneuvers, and shorter travel times. Second, the synodic period between Jupiter and Neptune is considerably shorter. The synodic period between two planets can be calculated using Equation 8.1. In this equation P_{syn} is the synodic period between the two planets, P_{sid1} is the sidereal period of planet 1, and P_{sid2} is the sidereal period of planet 2. The sidereal period of Jupiter is 11.87 years, and that of planet Neptune is 164.8 years. Using this equation indicates that the Jupiter-Neptune sequence appears every 12.8 years. The same calculation can be done for Saturn which has a sidereal period of 29.5 years. Inserting this value in Equation 8.1 returns that the Saturn-Neptune sequence appears every 36 years. The use of a Jupiter assist to reach Neptune is thus possible almost three times as often as a Saturn gravity assist [66].

$$P_{syn} = \frac{1}{|\frac{1}{Psid1} - \frac{1}{Psid2}|} \tag{8.1}$$

In addition, Jupiter can be more easily reached by a direct high-velocity launch from Earth, or by first performing a sequence of inner planet gravity assists. The Trident, or EVEEJN, route is an example of this second scenario. To further investigate the possibility of using Jupiter and Neptune as a gateway to the Kuiper Belt, a selection of additional sequences is evaluated. In these additional sequences inner Solar System planet flybys are used, ranging from one to three flybys, aiming to find efficient trajectories similar in quality to the EVEEJN result. The number of flybys is limited to three in order to find a high-quality trajectory with a reduced time to arrival and with a reduced quantity of flyby maneuvers. The selection of the additional flyby sequences is based on the results of Melman [36] and on the results shown in Section 8.1. Due to the limited duration of the thesis project the total number of additional sequences was limited to five.

Data of the best EVEEJN and JN sequence trajectories found in Section 8.1 are used to prune the search space of the additional sequences. To do this the approach explained in Section 7.3 is used. Within the original search space between the years 2025 and 2040 there exist two periods in which the Jupiter-Neptune alignment exists. The direct JN sequence found earlier utilizes the first opportunity to make use of this alignment by launching in January of 2030 and performing its Jupiter flyby in June 2032. The EVEEJN trajectory makes use of the second alignment period. This happens because the time of flight between launch and the flyby of Jupiter in this longer trajectory is close to nine years. Even if the launch of this trajectory took place on the very lower bound of the original search space, January 1st 2025, the Jupiter flyby would happen in 2034, at which point the alignment between Jupiter and Neptune has become sub-optimal. The most efficient EVEEJN trajectory that was found thus launches in May of 2035, in order to perform its Jupiter flyby in February 2044. The time between the selected JN and EVEEJN trajectory Jupiter flybys is eleven years and eight months, a reflection of orbital period of Jupiter and of the synodic period between the two planets discussed earlier in this section.

Based on the initial trajectory results the search space of the additional sequences can be limited and guided so that the intended Jupiter flyby happens when Jupiter and Neptune are aligned. This means that the Jupiter flyby has to happen in 2032 or 2044, with an arbitrary tolerance of plus-minus one year. With a launch in early 2025 this would mean that the time of flight to Jupiter has an upper boundary of approximately eight years, or about 3,000 days. For all additional sequences this initial opportunity in 2032 is considered first. If the resulting trajectories of a specific sequence are sub-optimal, a second run is done in which the Jupiter assist in 2044 is targeted. Whether a initial run is sub-optimal can be judged by analyzing the leg flight time between each flyby. If one or more of these are consistently near the upper boundary limit it is a clear indication that a longer allowed TTA is required.

Because all the additional sequences use an inner Solar System planet as their first flyby target, the maximum launch energy for these additional routes was again restricted to a maximum of 36 km^2/s^2. This limit is slightly higher than the 28 km^2/s^2 that was required for the EJS route, which was the highest C3 requirement of the initial set of sequences that started with an inner planet flyby. Keeping the upper boundary at the higher value ensures consistency and is also intended to prevent the pruning of optimal trajectories. The additional sequences and their results are shown in Table 8.2. For convenience the results of the JN, EVEEJN, and VVEJS sequences, discussed in Section 8.1, are listed in this table as well.

Sequence	C_3 [km^2/s^2]	DSMDV [km/s]	TTA [yrs]	TKB [yrs]	Launch Year	Jupiter Flyby Year
VVEJS	15.5	0.10	24.0	98.91	Feb 2033	Nov 2038
EVEEJN	19.6	0.39	21.6	119.5	May 2035	Feb 2044
JN	78.5	0.15	14.6	160.1	Jan 2030	Feb 2032
EEJN	26.4	0.49	18.9	161.7	Dec 2025	Nov 2032
EJN	36.0	0.86	18.6	147.7	Oct 2025	Jan 2032
EVEJN	31.8	1.50	19.8	162.1	Jan 2025	Dec 2032
VEJN	14.0	1.53	19.2	159.2	Feb 2025	Jul 2031
EVJN	35.7	2.01	17.8	163.6	Jan 2027	Jan 2033

Table 8.2: Results of the three original best performing planetary sequences and of the five additional Jupiter-Neptune sequences.

The EJN and EEJN sequences are viable alternatives to the EVEEJN route. Requiring less flybys and suitable for launch in late 2025, these solutions are less complex and can be launched in this decade. The remaining additional sequences require a DSMDV of over 1,000 m/s, which is certainly possible with their associated low C_3 parameter requirement, but will require a significant amount of spacecraft mass to be reserved for propellant instead of payload. Nevertheless they may be suitable as a back-up consideration for when a trajectory with an earlier launch window is missed.

8.3. Launch Windows

The launch windows of five of the best performing sequences are visualized in Figures 8.6 and 8.7. These launch windows are the result of allowing either a deviation of 1,000 m/s in the launch DV, or a deviation of 100 m/s in the DSMDV requirement. These deviations are relative to the original trajectory results shown in Figure 8.1 and Table 8.2. With these figures the launch sensitivity of a certain trajectory can be estimated. It is clear from the figures that increasing the maximum allowable C_3 provides many more options in comparison to allowing an increased DSMDV. This phenomenon is an expected and also preferable result. An increased budget on the launch vehicle is much easier and cheaper to realize than placing an extra reserve on the onboard propellant. Unfortunately, results of the EJN route are extremely concentrated inside a launch window of seven days. Efforts were made to diversify the trajectory results in subsequent optimization runs, but results remained concentrated on these dates. Of the remaining analyzed routes the EVEEJN route has the most narrow launch window, spanning just ten days. Generally it is shown that trajectories that make use of fewer flybys have broader launch windows.

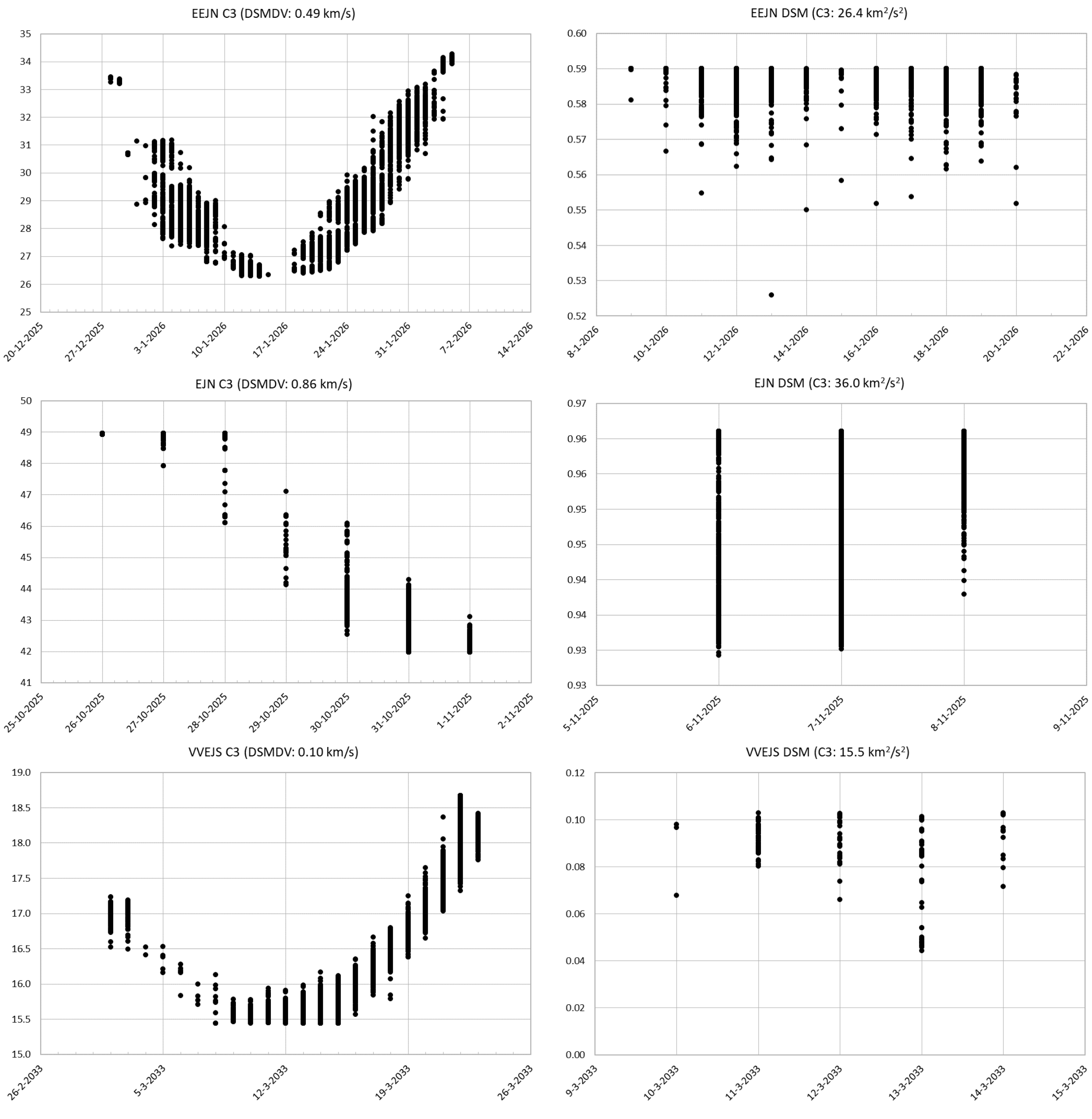

Figure 8.6: Rudimentary launch sensitivity study results for the EEJN, EJN, and VVEJS sequences. The left column of figures shows the results for variation in required C_3 energy in km^2/s^2 and a fixed maximum DSMDV value. The right column shows the variation in required DSMDV in km/s in combination with a fixed maximum DV value.

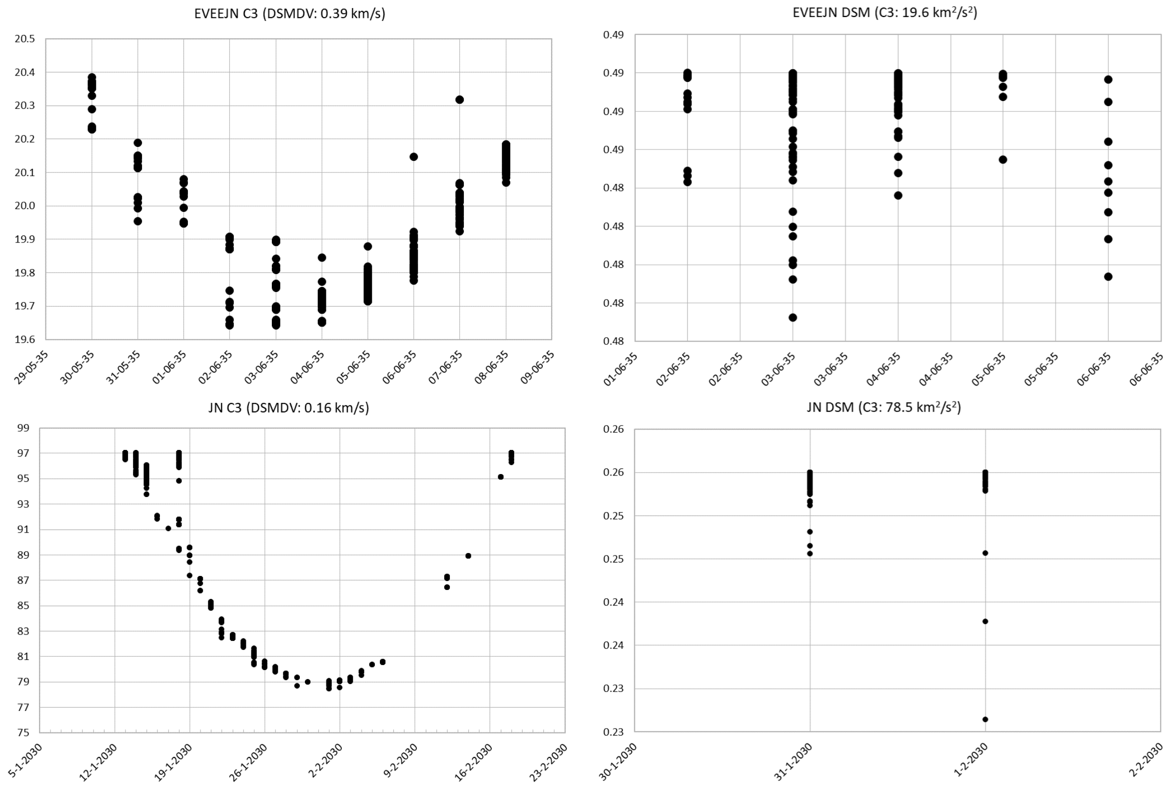

Figure 8.7: Rudimentary launch sensitivity study results for the EVEEJN, JN sequences. The left column of figures shows the results for variation in required C_3 energy in km^2/s^2 and a fixed maximum DSMDV value. The right column shows the variation in required DSMDV in km/s in combination with a fixed maximum DV value.

8.4. Technical Consequences

This section provides an indication of the spacecraft mass that can be deployed inside the Kuiper Belt by using the best performing trajectories identified in Sections 8.1 and 8.2. Five trajectories for different planetary sequences are selected based on their low DSMDV requirement. These sequences are: EJN, EEJN, EVEEJN, VVEJS, and JN.

Launch vehicle performance data used for the mass estimations are taken from information provided by the NASA Launch Services Program (LSP) [34]. The LSP provides general information regarding performance metrics for a wide range of launch vehicles. The five trajectories are evaluated with two different launch vehicles. For the launches that require a C_3 of less than 36 km^2/s^2 the Atlas V 401 and the Falcon Heavy (FH) with recoverable boosters are used. The Atlas V 401 is a smaller but reliable launcher that is the envisioned launch vehicle for the NASA Trident mission. For the JN trajectory only the Falcon Heavy (FH) with expendable boosters is used, as the Atlas V 401 and the FH with recoverable boosters are not powerful enough to accommodate this trajectory. While the Falcon Heavy is relatively new, and has not had the opportunity to establish a significant track record at time of writing, it is selected for evaluation rather than the Delta IV Heavy. Both the Delta IV and the Atlas V launch vehicle families are planned to be phased out in the upcoming years, with the Delta IV rockets already no longer being in production. To replace these vehicles the Vulcan rocket is currently under development by United Launch Alliance (ULA). However, the availability and extent of performance data on this next generation of launch vehicles is limited. The C_3 performance curves for the expendable Falcon Heavy and the Atlas V 401 are shown in Figure 3.1. The data in these graphs is used to establish the allowable spacecraft and propellant mass, or wet mass (m_{wet}), for each trajectory.

As the wet mass includes the mass of the propellant required to perform DSMs, the spacecraft dry mass (m_{dry}) is calculated by using the formulation of the Tsiolkovsky rocket equation as shown in Equation 8.2. In this equation g_0 is the standard gravity of 9.80665 m/s^2, and ΔV is the change of velocity provided by DSMs (DSMDV). As discussed in Section 3.6 an I_{sp} of 250 s is assumed.

$$m_{dry} = m_{wet} e^{\frac{-\Delta V}{I_{sp} g_0}} \tag{8.2}$$

The result of using the NASA LSP data and Equation 8.2 to calculate the allowable spacecraft wet and dry mass for each trajectory is shown in Table 8.3. Using the less powerful Atlas V 401 launch vehicle, a spacecraft with a dry mass of between 806 and 1,621 kg can be placed inside the Kuiper Belt for close to, or well over, 100 years. Using the more powerful FH with recoverable boosters, the possible spacecraft dry mass increases to between 1,524 and 3,322 kg for the same trajectories. Finally, for the faster and higher required C_3 JN trajectory, the allowable spacecraft dry mass is determined to be 2183 kg when the FH with expendable boosters is utilized.

Sequence	C_3 [km^2/s^2]	DSMDV [km/s]	TTA [yrs]	TKB [yrs]	Launcher	m_{wet} [kg]	m_{dry} [kg]
EJN	36.0	0.86	18.6	147.7	Atlas V 401 FH (rec)	1,145 2,165	806 1,524
EEJN	26.4	0.49	18.9	161.7	Atlas V 401 FH (rec)	1,565 3,125	1,282 2,559
EVEEJN	19.6	0.39	21.6	119.5	Atlas V 401 FH (rec)	1,900 3,895	1,621 3,322
VVEJS	15.5	0.10	24.0	98.91	Atlas V 401 FH (rec)	2,115 4,400	1,407 2,926
JN	78.5	0.15	14.6	160.1	FH (exp)	2,325	2,183

Table 8.3: Deployable spacecraft mass estimation for the selected five trajectory options. Launch vehicle performance data from NASA LSP [34]. FH (rec) signifies the Falcon Heavy with recovered boosters, (exp) signifies that the boosters are expended.

The minimum allowable spacecraft dry mass to declare the envisioned Kuiper Belt mission trajectories feasible was set at 450 kg in Section 3.6. The calculated m_{dry} of all five sequences well surpass that minimum value and are thus affirmed as feasible trajectories for a long-term Kuiper Belt exploration mission. Comparing the results with the dry mass of launched NASA spacecraft such as New Horizons (401 kg [30]), Voyager 2 (715 kg [39]), Galileo (1,298 kg [67]), and Cassini (2,125 kg [40]) provide further context and insight in the potential of such spacecraft masses. The deployable dry mass exceeds the New Horizons probe mass by at least 400 kg which enables a heavier spacecraft to be launched that is better equipped for the challenges of long-duration Kuiper Belt exploration. Instruments for long-distance observation of KBOs, larger systems for power generation and communication, or a more sizable onboard propellant budget for intermediate maneuvers are examples of the possibilities this increased spacecraft mass creates.

9

Conclusions

Previous efforts to propose trajectories with the intention of exploring the Kuiper Belt have been limited to identifying trajectories to visit selected objects. Zangari et al. [2], for example, reports preliminary spacecraft trajectories for 45 KBOs suitable for launch between 2025 and 2040. Others, such as Oleson et al. [4], focus on estimating the technological capabilities required to place a spacecraft in orbit of a KBO. However, these options either fly through the Kuiper Belt at Solar System escape velocity, or are not technologically feasible in the near future. In this thesis the possibility to achieve a trajectory which places a spacecraft inside the Kuiper Belt for an extended period of time has been investigated. This was done by performing an interactive multi-objective optimization approach with four distinct solution fitness criteria on a set of 20 planetary sequences previously proposed for reaching targets in the Kuiper Belt.

Using this method multiple routes were identified that are well suited to support long-duration flight through the Kuiper Belt. The most promising planetary flyby sequences were found to be VVEJS, EVEEJN, and JN. Excess launch energy (C_3) required for these trajectories ranges from 16 km^2/s^2, for sequences utilizing multiple inner planet flybys, to 75.5 km^2/s^2, for solutions utilizing a direct Jupiter-Neptune route. These solutions require between 100 and 400 m/s of ΔV capability for DSMs, and have a flight time to the inner boundary of the Kuiper Belt that ranges from 14.6 to 24 years. All these trajectories feature a flight time through the Kuiper Belt of well over or close to a hundred years. With these results an alternative is presented to the high-velocity flyby and orbiter missions proposals targeting specific KBOs. In addition it was found that trajectories that conclude their planetary flyby sequence with a Jupiter-Neptune leg are found to be especially well-suited for long duration Kuiper Belt flight. It is shown that in these cases planet Jupiter is used to reach Neptune faster, at which point Neptune is used to reduce the spacecraft's heliocentric velocity and extend the Kuiper Belt flight time. These results also indicate that opportunities for these type of trajectories are present every Jupiter-Neptune synodic period of 12.8 years.

This is the first study to the author's knowledge to identify trajectories that could position a spacecraft within the Kuiper Belt almost indefinitely. These results introduce an interesting new approach to consider for further exploration of the Kuiper Belt in order to better understand the formation period of the Solar System. However, the scope of this thesis was limited to determining the existence of trajectories to support this type of mission. The existence or technical feasibility of instruments to gather scientific data with use of these trajectories was not investigated. Future work should therefor evaluate these and other aspects in order to determine the true scientific value of the proposed trajectories .

10

Recommendations

Over the course of the project some aspects have been left untreated and some simplifications have been made. Furthermore, potentially interesting ideas have been left undeveloped due to project time constraints. These aspects and ideas are listed in this chapter. The recommendations are divided in three main topics. The first two topics are regarding the trajectory model and the optimization process respectively. The third section lists proposals or starting points for future research.

Trajectory model

- The powered gravity assist was not utilized in the trajectory model in order to reduce the complexity of the optimization problem. The solutions found in this thesis could perhaps be improved by implementing the powered gravity assist. Musegaas noted an average 7.8% improvement in final payload mass with utilization of the powered-gravity assist model compared to the unpowered variant [44].
- The Msc thesis of Melman[36] describes the use of aero-gravity assists in order to further improve trajectory solutions. An aero-gravity assist around planet Neptune could improve the maximum achievable bending angle parameter, which in turn could potentially increase the approach velocity while still resulting in a long Kuiper Belt flight time. This would positively affect the time of arrival parameter. It should be noted that aero-gravity assists have not been used in practice yet and that the use of one would necessitate a spacecraft design that tolerates the significant aerodynamic drag.

Optimization

- Optimization with multiple islands and an archipelago model was not utilized in this thesis. Using this method may improve or simplify the optimization method, as the multiple algorithm variants can be ran concurrently on separate islands.
- After preliminary testing of the NSGA-II and MOEA/D algorithms was completed, two additional multi-objective optimization algorithms were released in PaGMO version 2.12. These are the Non-dominated Sorting Particle Swarm Optimization (NSPSO) and the Multi-objective Hypervolume-based Ant Colony Optimizer (MHACO). These algorithms may be interesting to investigate.
- Combining the objective DV and DSMDV into a single objective reflected by the final payload mass reduces the optimization problem complexity. In this case it would likely be beneficial to keep the maximum value limits on the on the departure velocity and onboard propellant intact.

Follow-up research

- This thesis focused on identifying conventional high-thrust trajectories to the Kuiper Belt. A low-thrust trajectory study that includes gravity-assists should be performed in order to enable a comparison of results and determine the most attractive propulsion method for this type of mission.
- The minimum approach distance to Neptune was limited to 1.7 Neptune radii in the problem definition. A closer flyby distance than this could improve the trajectory solutions further. Further study of the effect of reducing the Neptune approach distance could be interesting.
- One of the major topics to further investigate in order to determine the true value of these long-term Kuiper Belt trajectories is the technological feasibility of observing KBOs from within the Kuiper Belt but without performing close flybys.
- Large databases of the orbital parameters of the TNOs that have been observed so far are provided by, among others, the minor planet center (*minorplanetcenter.net*) [68]. This data can be used to analyze the distance between the spacecraft and the nearest KBOs as it flies a long-duration Kuiper Belt trajectory. Alternatively, this data could also be included in the optimization problem directly in order to identify trajectories that approach as many KBOs as possible with a certain minimum distance.

Bibliography

[1] Ryan Mcgranaghan, B. Sagan, G. Dove, A. Tullos, James Lyne, and J. Emery. A survey of mission opportunities to trans-neptunian objects. *Journal of the British Interplanetary Society*, 142:296–303, September 2011.

[2] Amanda M. Zangari, Tiffany J. Finley, S. Alan Stern, and Mark B. Tapley. Return to the Kuiper Belt: Launch Opportunities from 2025 to 2040. *Journal of spacecraft and rockets*, pages 919–930, October 2018.

[3] Joel Poncy, Jordi Fontdecaba Baig, Fred Feresin, and Vincent Martinot. A preliminary assessment of an orbiter in the Haumean system: How quickly can a planetary orbiter reach such a distant target? *Acta Astronautica*, 68(5-6):622–628, March 2011. ISSN 00945765. doi: 10.1016/j.actaastro.2010.04.011.

[4] Steven R Oleson, Melissa L Mcguire, John Dankanich, Anthony Colozza, Paul Schmitz, Omair Khan, Jon Drexler, and James Fittje. Kuiper belt object orbiter using advanced radioisotope power sources and electric propulsion. Technical report, 2011.

[5] Julio A. Fernández. Chapter 1 - Introduction: The Trans-Neptunian belt—Past, present, and future. In Dina Prialnik, M. Antonietta Barucci, and Leslie A. Young, editors, *The Trans-Neptunian Solar System*, pages 1–22. Elsevier, January 2020. ISBN 978-0-12-816490-7. doi: 10.1016/B978-0-12-816490-7.00001-1.

[6] Ethan Siegel. This is everything that's wrong with our definition of 'planet'. https://www.forbes.com/sites/startswithabang/2019/07/09/this-is-everything-thats-wrong-with-our-definition-of-planet/ [Accessed on September 18, 2019], July 2019.

[7] Maria Antonietta Barucci. Kuiper Belt. In Muriel Gargaud, Ricardo Amils, José Cernicharo Quintanilla, Henderson James (Jim) Cleaves, William M. Irvine, Daniele L. Pinti, and Michel Viso, editors, *Encyclopedia of Astrobiology*, pages 892–902. Springer Berlin Heidelberg, Berlin, Heidelberg, 2011. ISBN 978-3-642-11274-4. doi: 10.1007/978-3-642-11274-4_854.

[8] NASA JPL. JPL Solar System Dynamics. https://ssd.jpl.nasa.gov/ [Accessed on May 16, 2020].

[9] NASA. NASA New Horizons Webpage. http://www.nasa.gov/mission_pages/newhorizons/ [Accessed on June 21, 2020], March 2015.

[10] Craig B. Agnor and Douglas P. Hamilton. Neptune's capture of its moon Triton in a binary–planet gravitational encounter. *Nature*, 441(7090):192–194, May 2006. ISSN 1476-4687. doi: 10.1038/nature04792.

[11] NASA/JPL/USGS. Pia00317: Global color mosaic of triton. https://photojournal.jpl.nasa.gov/catalog/PIA00317 [Accessed on June 28, 2020], June 1998.

[12] Alessandro Morbidelli and David Nesvorný. Chapter 2 - Kuiper belt: Formation and evolution. In Dina Prialnik, M. Antonietta Barucci, and Leslie A. Young, editors, *The Trans-Neptunian Solar System*, pages 25–59. Elsevier, January 2020. ISBN 978-0-12-816490-7. doi: 10.1016/B978-0-12-816490-7.00002-3.

[13] S. Alan Stern, John R. Spencer, Anne Verbiscer, Heather E. Elliott, and Simon P. Porter. Chapter 17 - Plans for and initial results from the exploration of the Kuiper belt by New Horizons. In Dina Prialnik, M. Antonietta Barucci, and Leslie A. Young, editors, *The Trans-Neptunian Solar System*, pages 379–394. Elsevier, January 2020. ISBN 978-0-12-816490-7. doi: 10.1016/B978-0-12-816490-7.00017-5.

[14] John R. Spencer, William M. Grundy, Francis Nimmo, and Leslie A. Young. Chapter 12 - The Pluto system after New Horizons. In Dina Prialnik, M. Antonietta Barucci, and Leslie A. Young, editors, *The Trans-Neptunian Solar System*, pages 271–288. Elsevier, January 2020. ISBN 978-0-12-816490-7. doi: 10.1016/B978-0-12-816490-7.00012-6.

[15] NASA and JHUAPL. New horizons: The path to pluto and beyond. http://pluto.jhuapl.edu/Mission/The-Path-to-Pluto-and-Beyond.php [Accessed on January 8, 2020].

[16] Tricia Talbert. NASA: New horizons spacecraft returns its sharpest views of ultima thule. https://www.nasa.gov/feature/new-horizons-spacecraft-returns-its-sharpest-views-of-ultima-thule [Accessed on April 22, 2020], 2019.

[17] Yanping Guo and Robert W Farquhar. New horizons mission. Technical Report January, 2006.

[18] NASA, SWRI, and JHUAPL. New horizons launch press kit, 2006.

[19] Alan Stern, Rick Binzel, Hal Levison, Rosaly Lopes, Bob Millis, and Jeff Moore. New Horizons 2. Technical report.

[20] New Horizons II Review Panel. Final Report of the New Horizons 2 Review Panel. Technical report, NASA, March 2005.

[21] Candice Hansen, Hammel Heidi, Don Banfield, Amanda Hendrix, Krishan Khurana, Damon Landau, Alfred McEwen, Linda Spilker, Tom Spilker, John Stansberry, Ed Stone, and Nathan Strange. Argo: Voyage through the outer solar system. Technical report, Outer Planets Assessment Group, 2008.

[22] C J Hansen, A S Aljabri, D Banfield, and E B Bierhaus. Triton science with argo-a voyage through the outer solar system, 2009.

[23] K L Mitchell, L M Prockter, W E Frazier, W D Smythe, B M Sutin, D A Bearden, and Trident Team. Implementation of trident: A discovery-class mission to triton. page 2, 2019. doi: 10.1089/ast.2018.1955.

[24] L M Prockter, K L Mitchell, J A Howett, W D Smythe, B M Sutin, D A Bearden, W E Frazier, and Trident Team. Exploring triton with trident: A discovery-class mission. In *50th Lunar and Planetary Science Conference*, March 2019. doi: 10.1089/ast.2018.1955.

[25] Louise M Prockter, Karl L Mitchell, David A Bearden, and William D Smythe. Triton: Exploring a Candidate Ocean World. In *European Planetary Science Congress 2018*, page 2, 2018.

[26] Laurens van der Heyden. Feasibility study of a spacecraft trajectory to observe the Kuiper Belt. Technical report, Delft University of Technology, 2019.

[27] Gautamraj Baskaran, Anurag Bonthalapati, Justin Lewis, Kyle Malone, Harsh Ved, and James Lyne. A survey of mission opportunities to trans-neptunian objects - part IV. In *AIAA/AAS Astrodynamics Specialist Conference 2014*, August 2014. ISBN 978-1-62410-308-7. doi: 10.2514/6.2014-4353.

[28] Ashley Gleaves, Randall Allen, Adam Tupis, John Quigley, Adam Moon, Eric Roe, David Spencer, Nicholas Youst, and James Lyne. A survey of mission opportunities to trans-neptunian objects - part II, orbital capture. In *Astrodynamics Specialist Conference*, August 2012. ISBN 978-1-62410-182-3. doi: 10.2514/6.2012-5066.

[29] Geffrey Ottman and Chris Hersman. The pluto-new horizons RTG and power system early mission performance. In *4th International Energy Conversion Engineering Conference and Exhibit (IECEC)*. doi: 10.2514/6.2006-4029.

[30] David Y. Kusnierkiewicz, Chris B. Hersman, Yanping Guo, Sanae Kubota, and Joyce McDevitt. A description of the Pluto-bound New Horizons spacecraft. *Acta Astronautica*, 57(2-8):135–144, 2005. ISSN 00945765. doi: 10.1016/j.actaastro.2005.03.030.

[31] Michael W Leeds, Ralph N Eberhardt, and Robert L Berry. Development of the cassini spacecraft propulsion subsystem. Technical report, JPL, NASA, 1996.

[32] Curt A Henry. An introduction to the design of the cassini spacecraft. Technical report, 2003.

[33] Yanping Guo and Robert W Farquhar. New horizons mission design. Technical report.

[34] NASA. Launch vehicle performance website. https://elvperf.ksc.nasa.gov [Accessed on May 31, 2020], 2020.

[35] United Launch Alliance. Atlas launch system mission planner's guide, 2008.

[36] Jeroen Melman. *Trajectory Optimization for a Mission to Neptune and Triton*. Master thesis, Delft University of Technology, 2007.

[37] H A Weaver, W C Gibson, M B Tapley, L A Young, and S A Stern. Overview of the new horizons science payload.

[38] NASA. Overview | cassini nasa solar system exploration. https://solarsystem.nasa.gov/missions/cassini/ [Accessed on April 22, 2020].

[39] NASA. Voyager backgrounder. Technical report, October 1980.

[40] Curt Henry. An introduction to the design of the cassini spacecraft. *Space Science Reviews*, 104: 129–153, July 2002. doi: 10.1023/A:1023696808894.

[41] The Johns Hopkins University Applied Physics Laboratory. New horizons : Spacecraft. http://pluto.jhuapl.edu/Mission/Spacecraft.php, 2020.

[42] NASA. Kepler: NASA's First Mission capable of Finding Earth-Size Planets. Kpler Press Kit, February 2009.

[43] K.F. Wakker. *Fundamentals of Astrodynamics*. TU Delft Library, 2015. ISBN 978-94-6186-419-2.

[44] Paul Musegaas. *Optimization of Space Trajectories Including Multiple Gravity Assists and Deep Space Maneuvers*. Master thesis, Delft University of Technology, 2012.

[45] S. Molenaar. *Optimization of Interplanetary Trajectories with Deep Space Maneuvers - Model Development and Application to a Uranus Orbiter Mission*. PhD thesis, TU Delft, 2009.

[46] The Johns Hopkins University Applied Physics Laboratory. Messenger Mission Design: Launch and Cruise. https://messenger.jhuapl.edu/About/Mission-Design.html [Accessed on April 6, 2020].

[47] Davide Conte and David B. Spencer. Targeting the martian moons via direct insertion into mars-orbit. In James D. Turner, Geoff G. Wawrzyniak, William Todd Cerven, and Manoranjan Majji, editors, *Astrodynamics 2015*, Advances in the Astronautical Sciences, pages 2389–2406, United States, January 2016. Univelt Inc. ISBN 9780877036296. AAS/AIAA Astrodynamics Specialist Conference, ASC 2015 ; Conference date: 09-08-2015 Through 13-08-2015.

[48] E R Lancaster and R C Blanchard. A unified form of lambert's theorem. Technical Report NASA-TM-X-63355, NASA Goddard Space Flight Center, Greenbelt, MD, United States, September 1968.

[49] R. H. Gooding. A procedure for the solution of Lambert's orbital boundary-value problem. *Celestial Mechanics and Dynamical Astronomy*, 48(2):145–165, June 1990. ISSN 1572-9478. doi: 10.1007/BF00049511.

[50] Dario Izzo. Revisiting Lambert's problem. *Celestial Mechanics and Dynamical Astronomy*, 121 (1):1–15, January 2015. ISSN 1572-9478. doi: 10.1007/s10569-014-9587-y.

[51] T. Vinko and D. Izzo. Global optimisation heuristics and test problems for preliminary spacecraft trajectory design. Technical Report GOHTPPSTD, 2008.

[52] E M Standish. Keplerian Elements for Approximate Positions of the Major Planets, 2012.

[53] European Space Agency. Global Trajectory Optimisation Problems Database. esa.int/gsp/ACT/projects/gtop/ [Accessed on June 16, 2020].

[54] T. Vinko, D. Izzo, and C. Bombardelli. Benchmarking different global optimisation techniques for preliminary spacetrajectory design. September 2007.

[55] Francesco Biscani and Dario Izzo. Esa/2: Pagmo 2.15.0, April 2020.

[56] Dario Izzo, Marek Ruciński, and Francesco Biscani. The Generalized Island Model. In Francisco Fernández de Vega, José Ignacio Hidalgo Pérez, and Juan Lanchares, editors, *Parallel Architectures and Bioinspired Algorithms*, pages 151–169. Springer Berlin Heidelberg, Berlin, Heidelberg, 2012. ISBN 978-3-642-28789-3. doi: 10.1007/978-3-642-28789-3_7.

[57] Pagmo development team. Pagmo documentation. esa.github.io/pagmo2 [Accessed on April 4, 2020].

[58] H. Li and Q. Zhang. Multiobjective optimization problems with complicated pareto sets, MOEA/D and NSGA-II. *IEEE Transactions on Evolutionary Computation*, 13(2):284–302, April 2009. ISSN 1941-0026. doi: 10.1109/TEVC.2008.925798.

[59] Q. Zhang and H. Li. MOEA/D: A multiobjective evolutionary algorithm based on decomposition. *IEEE Transactions on Evolutionary Computation*, 11(6):712–731, 2007.

[60] K. Deb, A. Pratap, S. Agarwal, and T. Meyarivan. A fast and elitist multiobjective genetic algorithm: NSGA-II. *IEEE Transactions on Evolutionary Computation*, 6(2):182–197, April 2002. ISSN 1089778X. doi: 10.1109/4235.996017.

[61] Aaron D Olds, Craig A Kluever, and Michael L Cupples. Interplanetary mission design using differential evolution. *Journal of Spacecraft and Rockets*, 44(5):1060–1070, September 2007. doi: 10.2514/1.27242.

[62] Kenneth Price, Rainer M Storn, and Jouni A Lampinen. *Differential Evolution: A Practical Approach to Global Optimization*. Springer Science & Business Media, 2006.

[63] Rainer Storn and Kenneth Price. Differential evolution - a simple and efficient heuristic for global optimization over continuous spaces. *Journal of Global Optimization*, 11:341–359, January 1997. doi: 10.1023/A:1008202821328.

[64] Kaisa Miettinen, Francisco Ruiz, and Andrzej Wierzbicki. Introduction to multiobjective optimization: Interactive approaches. volume 5252 of *Introduction to Multiobjective Optimization: Interactive Approaches*, pages 27–57, January 2008. doi: 10.1007/978-3-540-88908-3_2.

[65] C J Hansen, H B Hammel, and L J Spilker. Argo: Exploring the neptune system and beyond. In *EPSC Abstracts*, volume 4, pages 2009–796. European Planetary Science Congress, 2009.

[66] Dr. David R. Williams. Planetary Fact Sheet. https://nssdc.gsfc.nasa.gov/planetary/factsheet/ [Accessed on June 7, 2020].

[67] NASA JPL. Galileo Jupiter Arrival Press Kit, December 1995.

[68] IAU Minor Planet Center. https://minorplanetcenter.net/ [Accessed on June 7, 2020].